

6-14-2016

Distributed Coordination and Control of Renewable Energy Sources in Microgrids

Javad Khazaei Khazaei

University of South Florida, javadkhazaei@mail.usf.edu

Follow this and additional works at: <http://scholarcommons.usf.edu/etd>

 Part of the [Electrical and Computer Engineering Commons](#)

Scholar Commons Citation

Khazaei, Javad Khazaei, "Distributed Coordination and Control of Renewable Energy Sources in Microgrids" (2016). *Graduate Theses and Dissertations*.

<http://scholarcommons.usf.edu/etd/6274>

This Thesis is brought to you for free and open access by the Graduate School at Scholar Commons. It has been accepted for inclusion in Graduate Theses and Dissertations by an authorized administrator of Scholar Commons. For more information, please contact scholarcommons@usf.edu.

Distributed Coordination and Control of Renewable Energy Sources in Microgrids

by

Javad Khazaei

A dissertation submitted in partial fulfillment
of the requirements for the degree of
Doctor of Philosophy
Department of Electrical Engineering
College of Engineering
University of South Florida

Major Professor: Zhixin Miao, Ph.D.
Lingling Fan, Ph.D.
Rajesh Kavasseri, Ph.D.
Chung Seop Jeong, Ph.D.
Yu Sun, Ph.D.

Date of Approval:
June 8, 2016

Keywords: Distributed Control, Distributed Energy Resource, Consensus Theory, Impedance Modeling, Battery Energy Storage, Power Synchronization, Photovoltaic

Copyright © 2016, Javad Khazaei

DEDICATION

To my father and my mother.

ACKNOWLEDGMENTS

Firstly, I would like to appreciate my advisor Dr. Zhixin Miao who supported me for the past three years. I would especially appreciate an excellent opportunity that he gave me to not only do research on hot topics and publish high quality papers, but also to teach graduate and undergraduate level courses that improved my teaching experience significantly.

I would also like to appreciate Dr. Lingling Fan who has a wide range of research interests and sharp insights, she always was available to help and always was motivating me to do better, which truly helped me.

Secondly, I appreciate all my committee members: Dr. Rajesh Kavasseri, Dr. Chung Seop Jeong and Dr. Yu Sun for their advice and helpful comments.

I would like to thank Dr. Lakshan Piyasinghe, the former Ph.D. student in our group who was always a good friend and an excellent team member for my research. I believe team-work is the key part of successful research and he was the main team member in my research. I want to appreciate my classmates from the smart grid power system lab, including: Mohammed Alhaider, Yin Li, Hossein Ghassempour, Ahmad Tazay, Yan Ma, Minyue Ma, Yangkun Xu, Yi Zhou, and Dr. Ling Xu for the time I spent with them during the past three years.

Finally, I want to thank my father, Manouchehr Khazaei, my mother, Mahrokh Abdollahzadeh, my love, Faegheh Moazeni, my sisters, Atefeh and Solmaz for all the support and care they provided for me during my Ph.D. studies.

TABLE OF CONTENTS

LIST OF TABLES	v
LIST OF FIGURES	vii
ABSTRACT	xi
CHAPTER 1 OVERVIEW	1
1.1 General Introduction	1
1.2 Current State of Knowledge	4
1.2.1 PV	5
1.2.2 Offshore Wind Farm	6
1.2.3 Energy Storage Systems	7
1.2.4 Interactions and Unbalance Due to DERs	9
1.2.4.1 Interactions between Converters and Grid	9
1.2.4.2 Effect of Unbalance in Microgrids	11
1.3 Research Significance	12
1.4 General Problem Statement	15
1.5 Research Objectives	15
1.5.1 Sub-Objectives	16
1.6 Chapter Breakdown	17
CHAPTER 2 MODELING AND CONTROL IN MICROGRIDS	19
2.1 Introduction	19
2.2 Methodology	20
2.2.1 Voltage Source Converters (VSC)	20
2.2.2 Control in DERs	20
2.2.3 Lower Level Control/Primary Control	21
2.2.4 Upper Level Control-Centralized Approach	22
2.2.4.1 Centralized Secondary Control-Frequency Control	22
2.2.4.2 Centralized Secondary Control-Voltage Control	23
2.2.5 Upper Level Control-Decentralized Approach	24
2.2.6 Distributed Consensus Control Theory	24
2.2.6.1 Basics of Graph Theory	24
2.2.6.2 Consensus Based Secondary Control Design	26
2.2.7 Microgrid Modeling Techniques	28
2.2.7.1 Impedance Analysis	28
2.2.7.2 Dynamic Phasor Analysis	29

2.3	Discussions	30
CHAPTER 3 MPPT CONTROL FOR SINGLE PHASE PV		31
3.1	Introduction	31
3.2	Methodology	33
3.2.1	System Configuration	33
3.2.2	PV Control	34
3.2.3	Discrete Time Single Phase PLL	34
3.2.4	Discrete Proportional Resonant (PR) Controller	36
3.2.5	MPPT for PV Systems	38
3.2.6	Traditional IC Method	38
3.2.7	Modified IC-PI MPPT	41
3.3	Results	42
3.3.1	Case Studies	42
3.3.2	RT-LAB Performance	45
3.4	Discussions	46
CHAPTER 4 MINIMIZATION OF LOSSES IN MULTI-TERMINAL HVDC SYSTEM		48
4.1	Introduction	48
4.2	Methodology	51
4.2.1	Operation and Control of a MTDC System	51
4.2.2	Rectifier Control	51
4.2.3	Inverter Control	52
4.2.4	Circuit Analysis and Optimal Setting of Droop Gains	52
4.2.5	Rectifier Side Analysis	54
4.2.6	Inverter Side Analysis	55
4.2.7	Analysis of an Abnormal System	57
4.3	Results	58
4.3.1	Case Studies	58
4.3.2	One of the Inverter Side Terminals Is Tripped	59
4.3.3	Change of Active Power Generated by Wind Farms	61
4.4	Discussions	64
CHAPTER 5 DISTRIBUTED CONTROL FOR ENERGY STORAGE SYSTEM		65
5.1	Introduction	65
5.2	Methodology	68
5.2.1	Distributed Control Design Philosophy	68
5.2.2	System Model and Communication Graph	69
5.2.3	Design of the Inputs	70
5.2.4	Stability Analysis	72
5.2.5	Numerical Example	73
5.2.6	Test System Circuit Configuration	74
5.2.7	Detailed Battery Models	75
5.2.8	Battery Converter Controls	78
5.3	Results	81
5.3.1	RT-Lab Simulation Results	81

5.3.2	Discharging Event	81
5.3.3	Charging Event	81
5.4	Discussions	82
CHAPTER 6	IMPEDANCE MODELING AND MIMO ANALYSIS	84
6.1	Introduction	84
6.2	Methodology	86
6.2.1	Power Synchronization Control	86
6.2.2	Transfer Function from Angle to Power	88
6.2.3	Alternating Voltage Control Loop	90
6.2.4	Impedance Model of VSC with PSC Control	91
6.2.5	Impedance of Vector Control	92
6.2.6	Outer Loop Effects	93
6.2.7	The PLL Effect	95
6.2.8	Parameter Selection	96
6.3	Results	99
6.3.1	MIMO Stability Analysis and Validation	99
6.3.2	Impedance of the Converter for Different Control	100
6.3.3	Stability under Different SCR Scenarios	101
6.3.4	The Effect of Filter	105
6.3.5	The Effect of PSC Loop Gain	106
6.4	Discussions	107
CHAPTER 7	DYNAMIC PHASOR MODELING FOR UNBALANCED MICROGRIDS	109
7.1	Introduction	109
7.2	Methodology	111
7.2.1	DP Approach	111
7.2.2	Microgrid Configuration	113
7.2.3	The DP Model of a Single-Phase PV	113
7.2.4	DP Model of a PR Controller	115
7.2.5	Induction Machine Model in Dynamic Phasors	116
7.2.6	Integrated Microgrid Model in Dynamic Phasor	118
7.3	Results	119
7.3.1	Case Studies	119
7.3.1.1	Case Study 1	120
7.3.1.2	Case Study 2	121
7.3.1.3	Case Study 3	123
7.4	Discussions	125
CHAPTER 8	CONCLUSIONS	127
8.1	Results	127
8.2	Future Work	129
8.2.1	Lower Level Control	129
8.2.2	Upper Level Control	129
8.2.3	Parallel Programming in Power System and Smart Grids	130

REFERENCES	131
APPENDICES	141
Appendix A List of Parameters	142
Appendix B Reuse Permissions of Published Papers for Chapters 3, 4, and 7	146
ABOUT THE AUTHOR	End Page

LIST OF TABLES

Table 4.1	Droop gains at the base case	58
Table 4.2	Droop gains, voltages and currents for case 1 in line trip event	59
Table 4.3	Droop gains, voltages and currents for case 2 in line trip event	61
Table 4.4	Droop gains, voltages and currents for case 1 in active power change	63
Table 4.5	Droop gains, voltages and currents at steady-state for case 2 in active power change	64
Table 5.1	Parameters of controllers	80
Table 7.1	Eigenvalues of the system without PV	122
Table 7.2	Eigenvalues of the system with PV	122
Table A.1	Parameters of single phase PV for Sunpower panel	142
Table A.2	Parameters of the wind farm side rectifiers	142
Table A.3	Parameters of the grid side inverters	142
Table A.4	Parameters of the system	143
Table A.5	Parameters of transformers	143
Table A.6	Parameters of battery control	143
Table A.7	Parameters of individual batteries	143
Table A.8	System parameters for VSC-HVDC model	144
Table A.9	Parameters of individual VSC	144
Table A.10	Parameters of power synchronization	144
Table A.11	Parameters of vector controllers	144
Table A.12	Parameters of the induction machine	144
Table A.13	Parameters of the PV	145

LIST OF FIGURES

Figure 2.1	Basic diagram of a three phase voltage source converter connected to grid.	20
Figure 2.2	Microgrid structure in islanded mode and grid connected.	21
Figure 2.3	Lower level control of DERs.	22
Figure 2.4	Upper level control of microgrids in centralized approach.	23
Figure 2.5	Distributed control of microgrids; upper level decentralized approach.	25
Figure 2.6	Small signal model of a converter connected to grid.	28
Figure 3.1	Topology of a single-phase PV grid integration system.	33
Figure 3.2	Block diagram of PV control system.	35
Figure 3.3	Discrete-time model of a single-phase PLL for the PV system.	35
Figure 3.4	Control diagram of PR controller.	36
Figure 3.5	Bode plot for PR controller for different K_r , while $K_p = 1$ and $\omega = 377\text{rad/s}$.	37
Figure 3.6	Structure of PR controller.	38
Figure 3.7	The MPPT structure for a single-phase PV in RT-Lab.	40
Figure 3.8	Error signal description based on I-V characteristic of PV.	40
Figure 3.9	Improved IC MPPT for PV systems.	42
Figure 3.10	V-I and P-V curves for different irradiance values of Sunpower PV panel.	42
Figure 3.11	Irradiance step change and the MPPT input error.	43
Figure 3.12	The AC current magnitude reference.	44
Figure 3.13	PV output power and DC current for traditional MPPT.	44
Figure 3.14	PV output power and DC current for the proposed MPPT.	45
Figure 3.15	PV voltage in operating point change case.	45

Figure 3.16	Simulation results from Opmonitor block in RT-LAB.	46
Figure 4.1	A 6-terminal MTDC schematic.	49
Figure 4.2	Control of wind-side converters.	52
Figure 4.3	Control of grid-side converters.	52
Figure 4.4	Simplified equivalent DC model for MTDC.	53
Figure 4.5	Voltages at grid side and wind farm side terminals for case 1 in line trip event.	60
Figure 4.6	Currents at grid side and wind farm side terminals for case 1 in line trip event.	60
Figure 4.7	Droop gain change of grid side terminals for case 2 in line trip event.	61
Figure 4.8	Voltages at grid side and wind farm side terminals for case 2 in line trip event.	62
Figure 4.9	Currents at grid side and wind farm side terminals under optimized operation.	62
Figure 4.10	Voltages at grid side and wind farm side terminals for fixed droop gains in active power change.	63
Figure 4.11	Voltages at grid side and wind farm side terminals for adaptive droop gains in active power change.	64
Figure 5.1	Communication graph of the proposed system.	69
Figure 5.2	Block diagram of the simplified battery models including consensus based SOC management control.	74
Figure 5.3	Simulation results of the analysis model; $Q = \text{diag}([800, 10]), R = 200, K_1 = -20, K_2 = 2.23860, c = 0.01$.	75
Figure 5.4	Simulation results of the analysis model; $Q = \text{diag}([300, 10]), R = 5000, K_1 = -2.4495, K_2 = 0.4487, c = 0.01$.	76
Figure 5.5	Comparison of two designs when power limits are enforced.	77
Figure 5.6	Microgrid system composed of battery energy storage systems and loads.	78
Figure 5.7	Detailed electrical battery model.	78
Figure 5.8	Battery converter control blocks.	79
Figure 5.9	Discharging case; consensus control has been enabled at 300 seconds and consensus achieves at 2300 seconds and power levels achieve consensus at 2600 seconds, each 32 kW.	82

Figure 5.10	Load increase occurs at 2458.5 seconds, frequency is brought back to 60 Hz by secondary frequency control, battery power levels are different at 2458.5 seconds due to various gains for secondary frequency control: $K_{if1} = 0.01, K_{if2} = 0.02, K_{if3} = 0.04$.	82
Figure 5.11	Reactive power and voltage for three batteries; the reference reactive power is set to 0 and voltage reference is set to 400 V.	83
Figure 5.12	A charging event shows power and SOC consensus are achieved after around 2500 seconds.	83
Figure 6.1	Back-to-back VSC-HVDC connected to a weak AC grid with two different controls at the rectifier side.	86
Figure 6.2	Simplified model of the system with PSC; $R = 0 \Omega, L = 0.04 H, R_g = 0.1 \Omega, L_{g1} = 0.25 H$ for $SCR = 1, L_{g1} = 0.088 H$ for $SCR = 2$ and $L_{g1} = 0.048 H$ for $SCR = 3$.	87
Figure 6.3	Simplified block diagram for inner loop control	97
Figure 6.4	Simplified block diagram for outer loop control	98
Figure 6.5	Impedance model of a converter connected to grid.	99
Figure 6.6	Comparison between real parts of converter impedances, $Z_{conv}(s)$ for different controllers of rectifier side converter.	101
Figure 6.7	Comparison of eigen loci of $Z_g(s)Y_{conv}(s)$ for different SCR values and controllers of the rectifier side converter; power transfer level is 100 MW; (a) PSC; (b) vector control with PI power loop; (c) vector control without PI power loop.	102
Figure 6.8	Comparison of singular value plots of $I + Z_g(s)Y_{conv}(s)$ for the different SCR values and controllers of the rectifier side converter; power transfer level is 100 MW; high pass filter is included for the PSC.	102
Figure 6.9	Simulation results for step change in real power when vector control is applied and SCR is 3.	103
Figure 6.10	Simulation results for step change in real power when vector control is applied and SCR is 1.	103
Figure 6.11	Simulation results for step change in real power when PSC is applied and SCR is 3.	104
Figure 6.12	Simulation results for step change in real power when PSC is applied and SCR is 1.	104

Figure 6.13	Simulation results for different active power levels for three different control approaches; (a): Vector control without outer power loops, (b) Vector control with outer power loops, (c) power synchronization control, a three-phase balanced fault is applied at $t = 5$ s at the inverter AC side and cleared after one cycle, SCR for this case is set to 2.	105
Figure 6.14	Effect of filter on root locus curves of the system when SCR is 1.	105
Figure 6.15	Real-time simulation results for the effect of filter when SCR is 1 shown in different scales; (a): effect of filter during the operation, (b): zoom in version of the first subplot.	106
Figure 6.16	Root loci of PSC for SCR equal to 1, with the high pass filter.	106
Figure 6.17	Real-time simulation results for different PSC gain loops when the $SCR=1$; (a): PSC loop gain is 390, (b): PSC loop gain is 200, (c) PSC loop gain is 50.	107
Figure 6.18	Effect of filter and high gain PSC.	107
Figure 7.1	The study system; unbalanced microgrid.	113
Figure 7.2	A basic configuration of PV system.	114
Figure 7.3	Simplified PV model with different combinations; (a) LCL filter, (b) L filter	114
Figure 7.4	Basic control of a single-phase PV.	115
Figure 7.5	Conversion from abc to pnz and back to abc for an induction machine.	118
Figure 7.6	(a) Model of microgrid with PV in phase a , (b) model of microgrid in phase b and c	118
Figure 7.7	Simulation results of torque and rotor speed due to a step change in mechanical torque (from 28 N.M to 23 N.M).	120
Figure 7.8	Simulation results of the IM stator current, stator voltage and PV current due to a step change in mechanical torque (from 28 N.M to 23 N.M).	121
Figure 7.9	Simulation results for the effect of irradiance change.	123
Figure 7.10	The dominant modes (120 Hz, and the voltage stability mode) by increasing the line length.	124
Figure 7.11	Stator voltage when the grid line length increases from 3 km to 30 km; simulation results are produced by Matlab/SimPowerSystems.	124
Figure 7.12	RMS stator voltage when the grid line length increases from 3 km to 30 km.	125
Figure 7.13	Simpowersystems simulation results for the effect of grid line length increase; (a) torque (b) rotating speed (c) instantaneous current from PV.	125

ABSTRACT

Microgrid is an emerging technology in the field of electrical engineering which employs the concept of Distributed Energy Resources (DERs) in order to generate electricity in a small sized power system. The main objectives of this dissertation are to: 1- design a new control for lower level control of DERs in microgrids, 2- implement distributed upper level control for DERs in microgrids and 3- apply analytical approaches in order to analyze DERs in microgrids. The control in each DER can be divided into two main categories: lower and upper level. Lower level control is the main objective of control in each DER. For example, the lower level control in Photovoltaic (PV) is in charge of transferring the maximum power from sun into the main grid. Unlike the lower level control, the upper level control is an additional control loop on top of the lower level controls. For example, Voltage/Frequency (VF) controllers are installed on top of Active/Reactive (PQ) power controller in energy storage devices as upper level control. In this dissertation, for the lower level control improvements, two widely used DERs are selected (PV, and offshore wind farm) and new control algorithms are developed in order to improve the performance of lower level controllers in these DERs. For the PV lower level improvement, a new control methodology is proposed in order to minimize the maximum power tracking error in PV lower level controller. Second contribution in lower level control is for the offshore wind farm applications based on Multi-Terminal High Voltage Direct Current (MTDC) transmission; a new control is designed in order to minimize the losses in transmission lines through lower level control of High Voltage Direct Current (HVDC) converters.

For the upper level control, this dissertation considers the energy storage as another mostly used type of DER in microgrids. The lower level control for energy storage is in charge of controlling the PQ of the energy storage. The main contribution in the upper level control is to implement the distributed control algorithm based on consensus theory for battery energy storages in order to maximize the efficiency, energy management as well as synchronizing the performance of parallel

energy storage devices in microgrids. In this case, the consensus based distributed control algorithm with limited information exchange between neighboring energy storage units is proposed and implemented to validate the claim.

The third contribution of this research is to apply advanced analysis techniques to evaluate the performance of the DERs in microgrids. Two approaches are introduced for microgrid modeling in this research. Firstly, an impedance modeling technique is used to model the offshore wind farm connected to the main AC grid through HVDC transmission line. Multiple Input Multiple Output (MIMO) Nyquist analysis and singular value analysis are used to assess the interactions between HVDC converter and grid. Secondly, an unbalanced microgrid is considered and Dynamic Phasor (DP) analysis is applied in order to find the stability limitations under different scenarios.

This dissertation has led to seven journal papers (five published, one journal in revision process and one journal submitted recently) and four conference papers.

CHAPTER 1

OVERVIEW

This chapter briefly introduces the advances toward microgrid and DER technology and classifies the objectives and significance of this research in microgrid and DER technology.

1.1 General Introduction

Based on economic, technological and environmental changes during the past years and concerns about global warming issues, centralized generation units such as power plants based on synchronous generators are getting less attention compared to distributed generation. Microgrid is a systematic approach that considers the generation and associated loads as a subsystem. The microgrid idea incorporates the Distributed Energy Resources (DERs) and loads in both grid connected and islanded mode conditions [1, 2, 3]. Microgrid idea also brings isolation in case of disturbances where distributed generation and corresponding loads can be separated from the main Alternative Current (AC) system (islanded operation). This ability provides a higher local reliability compared to the power systems based on massive synchronous generators.

DERs are covering a wide range of applications such as: gas turbines, microturbines, Photovoltaic (PV), fuel cells, wind farms and energy storage units. Most DERs require an inverter to interface with the distribution AC system. A basic microgrid structure is composed of a group of radial feeders, critical/non-critical loads, and DER units. The entire system may be connected to the main AC grid (grid connect mode) or it may work as stand alone (autonomous/islanded mode). Therefore, the operation of a microgrid can be classified into two main approaches:

- 1- Islanded operation [4, 5].
- 2- Grid connected operation [6].

Islanded mode is when the microgrid is not connected to the main grid and it is operating independently to support its local loads or share energy between the neighbors. In this case, the islanded microgrid should not only retain the voltage and frequency, but also be able to control the supply and demand. On the other hand, the grid connected mode is when the microgrid is supported by the grid and there is no need for regulating the voltage or frequency, but the supply and demand can be controlled.

Whether a microgrid is operating at the grid connected or the islanded mode, renewable energy sources are integrated to generate electricity. Integrated renewable energy sources performing as a microgrid have locally solved the energy problems and brought more efficiency and flexibility to power systems. This would not be achieved without the significant improvement of power electronic devices implemented for renewable energy sources. Future power systems will mainly be composed of a number of interconnected microgrids where each microgrid is in charge of supplying its own demand as well as sharing the energy with the neighbouring microgrids in case of extra generation.

Hence, the future microgrid technology will become more distributed where the generation and consumption should be planned as a whole unit of multiple distributed microgrids, or simply distributed agents [7]. With the recent improvements towards smart buildings and smart grids, one should anticipate that small distributed renewable generation units are going to be integrated soon. However, one of the most significant concerns related to the renewable energy sources in the microgrids is their limited operating time due to the uncertain behavior [8]. For example, Photovoltaic (PV) modules can only generate electricity in presence of sun irradiance, or wind farms can only operate in places where sufficient amount of wind exists. Therefore, due to the uncertain behavior of renewable energy resources in microgrid, battery energy storage systems are commonly implemented as the energy buffers [9].

Microgrid control can be divided into two main levels:

- 1- Centralized control [10, 11].
- 2- Decentralized control [12, 13]

In the centralized control, the microgrid central controller receives the data from each DER and issues the commands such as power references to the generation units or control signals to the loads. One of the main drawbacks regarding the centralized controller is that the central controller should communicate with each distributed renewable energy source, where fast communication system is highly expensive. Moreover, in case of a failure in the central controller, the entire system fails and will not operate optimally. Decentralized controllers are the best solutions for the centralized controller drawbacks. The decentralized control locally controls the DER units and guarantees the stability in a global scale by only communicating between neighboring distributed generations. Therefore, we used decentralized approach in this dissertation which provides more advantages compared to centralized approaches.

Another point of view for microgrid control is to separate the controllers into two levels; 1- lower level control and 2- upper level control. The lower level control of microgrids includes a short-time scale control for resonance stability analysis and various individual control design for DERs. However, the upper level control is mainly used for the long-time scale where the power balance, or frequency deviations will be involved. Moreover, optimization schemes or coordinations will be implemented and tested in upper-level research [14]. Depending on the type of DER, lower level control may differ. For example, the lower level control in PV is mainly in charge of transferring the maximum generated power by sun irradiance to the grid through an inverter. Another example would be the energy storage, where the lower level control is in charge of controlling the generated active and reactive powers through charging and discharging cycles of battery Direct Current (DC) voltage. The upper level control, however, will be supplemented on top of the lower level control to add more functionalities to the entire system, in case there is a global objective. For example, when the microgrid is operating in an islanded mode, the global objective for the upper level control would be controlling the voltage and frequency in the entire microgrid. In the next part, current progress in microgrid area will be discussed in detail.

1.2 Current State of Knowledge

This part of dissertation reviews the existing literature in microgrid systems and provides a background for motivation of research and problem statement. Generally, a microgrid can be viewed in three different levels:

1- Microgrid Model

This level considers the microgrid as a whole, where the ultimate goal is providing an overall stability. There are several factors impacting the stability in this level including interactions between power electronic converters and the grid, the effect of harmonics and unbalance, power quality issues in the entire system, stability limits, and etc.

2- Microgrid Lower Level Control

Microgrid is composed of many DERs. Each DER has a power electronic converter with a general control function. For example, PV converter transfers the maximum generated power into the system, or energy storage converter controls the active and reactive power in case it is necessary. Lower level control is dedicated to the general control functionality of each DER.

3- Microgrid Upper Level Control

Upper level control is the supplementary controller on top of the lower level control or primary control with a global objective. For example, when the microgrid is in the stand alone condition (islanded operation), the upper level control controls the voltage and frequency in the entire microgrid. Upper level control can be centralized or decentralized, too.

This dissertation will cover topics in the three levels stated above. For the microgrid model, two problems are considered: interaction between converters and grid, and unbalanced microgrids. For the lower level control, two main DERs broadly used in microgrid applications are selected: PV and wind farm. For the upper level control, an energy storage is selected as the DER to be investigated and decentralized control approach is proposed. Below is a brief introduction of the current state of knowledge in the three targeted levels of microgrids.

1.2.1 PV

PV is widely used because of its low operational and maintenance cost, and due to the public attention to green energy sources. Based on previous studies, PV system will become the most widely spread renewable energy source in 2040 [15, 16]. The main objective of the PV system is to absorb the energy from the sun and convert it to the electricity via a DC-to-AC power electronic converter. Such process is conducted by an inverter control named Maximum Power Point Tracking (MPPT) algorithm. MPPT tracks the maximum power even in load change or under changing weather conditions. There are several approaches to achieve the maximum power in PV systems, including Incremental Conductance (IC), Perturb and Observe (PO), and Hill Climbing (HC). Previous studies have mainly focused on improving the performance of MPPT algorithms applied in PV systems. For example, adaptive hill climbing MPPT technique is proposed in [17], or a comparison between PO and HC method is conducted in [18]. While PO and HC offer more simplicity, there are several issues regarding these two approaches. For example, PO method provides error around the maximum power point and cannot lock the controller in the maximum power [19]. In comparison to PO and HC, IC algorithm is more complicated and in some cases is slow, yet it can track the maximum power precisely without any error providing more efficiency. Therefore, any solution to improve the IC MPPT performance and its simplicity is highly in demand. To that end, there are a few papers investigating the improvements toward the IC MPPT approach. Variable step size method is proposed in [20] in order to increase the speed of IC MPPT convergence, however, the complexity is even more than previous approaches. In [21], a novel approach is introduced as an alternative to the IC method using the slope of power-voltage ($P - V$) curve in a PV system. However, there is a voltage deviation ($\frac{dV}{dt}$) term in the denominator of the error signal which provides infinity output if it is zero. To solve this problem, a dead-band controller is suggested in [19] to replace the zero voltage deviation by a very small number, but still it does not solve the problem. Therefore, more research is yet to be done in this topic to enhance the operation of IC MPPT algorithm.

1.2.2 Offshore Wind Farm

In the large scale application of wind farms, offshore wind energy is the keystone. Nowadays, the application and the grid connection of large offshore wind farms are receiving more attention. As the wind farm capacity is higher, the application of offshore wind farm is more feasible. This is due to better wind profiles and large space demands in offshore. There are two options to transfer the generated power from offshore to the onshore station; 1- High Voltage Alternative Current (HVAC), and 2- High Voltage Direct Current (HVDC). Compared to the HVAC transmission system, HVDC provides several advantages when the offshore capacity is large [22]:

- AC cable generates considerable reactive power which significantly reduces the active current capacity of the cable, but HVDC does not have this problem.
- Resonances may occur in HVAC transmission due to high capacitance of the cable, but not in HVDC.
- In HVDC connections, wind turbine and AC grids are synchronously coupled, which means any fault in either grid or wind farm side will propagate in the entire system, while in HVDC, the wind farm and the grid are isolated by DC transmission.
- In HVDC system, there is no charging current in DC cable and there is no limit on DC cable length.
- HVDC has two converters; one in the wind farm side and one in the grid side. Therefore, the full controllability of the active and reactive power is provided by HVDC, but not for HVAC.

These main advantages of HVDC transmission toward HVAC have convinced the electrical utilities to consider the HVDC as the best solution for large offshore wind farm generations.

Multi-Terminal HVDC (MTDC) is a new concept of HVDC system which can be applied in large offshore wind farms, where the interconnection between multiple large offshore wind farm stations are necessary. Moreover, it will increase the reliability and utilize the transmission lines optimally. Generally, MTDC is composed of multiple wind farm stations which are intersecting in offshore through a common interconnection point. A main DC cable is then used in order to transfer the

generated power by multiple offshore stations to multiple onshore stations. At onshore stations, the main cable will be interconnected to many onshore DC cables same as the offshore station. Several studies have demonstrated the practical applications and barriers of MTDC systems for large offshore wind farms [22, 23, 24, 25, 26]. For example, [24] investigates the operation of three different types of MTDC configurations, or [25] proposes a new control approach for DC voltage control in MTDC systems.

One of the main advantages of the MTDC is the application of droop control in order to share the generated power between multiple onshore stations based on the capacity of the generation. However, there is a vital issue in MTDC system as the main DC cable carries a large DC current, thus generates a huge amount of transmission losses. Several studies focused on the minimization of losses in MTDC systems. For example, in [27], losses in DC transmission lines are minimized by regulating all the grid side DC voltages and selecting the droop gains proportional to the corresponding cable resistances.

The proposed method for loss minimization in [28] suggests that the set point of DC side at each inverter station should be regulated by an optimization algorithm. The proposed “optimum voltage control” minimizes the losses, however, it fails in proper power sharing among onshore stations. Therefore, it is still required to improve the operation of MTDC systems in large offshore wind farm applications by reducing the transmission line losses and without modifying the main objective of power sharing through droop control.

1.2.3 Energy Storage Systems

In case of power disturbances, synchronous generators cannot rapidly respond to the fault and make the system stable, as they are generally having very slow dynamics. In this situation, a high speed control of active/reactive or voltage/frequency is needed. Power electronic devices can provide high speed active/reactive power control. One interesting alternative is the application of energy storage in order to maintain the system reliability and power quality with fast controllers. The main characteristic of energy storage is to respond to the sudden load changes, supply the load in case of faults, and provide fast active and reactive power support to the loads.

However, the application of energy storage for active/reactive control or load support is not limited to the distribution and transmission level. Recent studies have shown that the energy storage application in microgrids can provide several advantages compared to the operation of microgrids with no energy storage devices. One of the most significant concerns related to the distributed renewable energy sources in microgrids is their uncertain behavior due to the limited supply of renewable source. For example, in different weather conditions, PV modules cannot generate the nominal power [29, 30], or wind farms cannot operate optimally in case the wind speed is not enough [31]. In these scenarios, energy storage can be utilized to balance the energy as an energy buffer [32, 33, 34]. A few papers have demonstrated the application of energy storage devices in microgrids. For example, [33] studies the smoothing performance of PV and wind generation in presence of battery energy storage systems as a hybrid microgrid. Another paper [35] reviews the challenges of integrating the energy storage in distribution power systems, and describes different control methodologies implemented for energy storage systems.

Most of the applications stated above are considering the performance of energy storage system in improving the lower level controllability of the entire system. It should also be mentioned that the energy storage can be used for upper level control improvements as well. The application of upper level control in energy storage is a new topic. There are two different approaches in designing the upper level controller for energy storage devices: 1- centralized controllers, and 2- decentralized controllers. As discussed earlier in the beginning of the chapter, centralized controllers have a high risk of single point of failure and need for extra communication links between the controller and DERs. As a result, application of the centralized controllers in upper level control is very limited. In contrast to the centralized controllers, decentralized controllers provide multiple benefits, and are of interest in microgrid applications [36, 37, 38, 39]. There are a few papers investigating the effect of decentralized upper level control in energy storage with multiple objectives [40]. For example, [40] designs a microgrid composed of energy storage and microsources. The lower level control is in charge of controlling the voltage and frequency, however, the upper level control tries to set the power level of the energy storage devices to zero, meaning the energy storage finally will not be charged or discharged. Distributed control has also been applied in energy storage devices

to achieve synchronization for energy and power levels [41]. Such a complicated approach, in case of complex microgrids with many components will be too difficult to deal with. Moreover, the communication is not limited, as all the states of the system will be synchronized by the designed approach. Another problem related to their design is that it only works for one operating mode (islanded microgrid) and in case of grid connected microgrid, the proposed controller should be changed completely. Therefore, there is a significant demand to improve the distributed control in energy storage devices in microgrid application. The proposed control should not only consider the simple design approach, but also limit the information exchange between energy storage devices, and operate in both operating modes of a microgrid (islanded and grid connected).

1.2.4 Interactions and Unbalance Due to DERs

As discussed earlier, power electronic devices or converters provide fast controllability in power systems especially in microgrids. However, grid connected inverters provide some barriers too. For example, single phase PV systems are extensively used in home applications. One should consider an unbalance effect due to the single phase PV penetration into the power grids. Moreover, grid connected converters may interact with the grid if the grid impedance is high. As a result, there should be some analysis approaches in order to evaluate the operation of grid connected systems, find the limitations and stability issues in microgrids, and provide a solution to make the system stable.

1.2.4.1 Interactions between Converters and Grid

Most of DERs are connected to the main system through an inverter. This is called grid connection of inverters. A grid connected inverter normally operates as a current source to inject current to the main grid. Extensive research has been conducted in recent years to study the interactions between grid connected converters and the main grid. These studies have focused on grid stability in the presence of DERs, or harmonic problems due to inverters. Recent studies have found that the grid impedance may deteriorate the inverter control performance resulting instability issues [42]. Such instability problems can be mentioned as: harmonic resonances, a destabilization of

the converter current controller, or a synchronization of the converter to the grid. There are several approaches to analyze the inverter grid interactions, among which, time domain and frequency domain techniques are more common. However, they need the detailed inverter control models and even coupling between multiple inverters should be taken into account, which complicates the analysis. On the other hand, impedance analysis has recently been proposed and proved to be the best approach to analyze the converter grid interactions. In this case, as the grid stability is the main objective, internal behavior of the inverter including the control can be neglected. An impedance based approach provides a suitable analysis tool, since it avoids complete modeling of inverters. In addition, it works with different grid impedances or in case of coupled inverters without any modification in analysis. The impedance analysis for grid connected inverters is well studied in the literature [43, 42, 44, 45]. For example, [43] investigates the impedance analysis for Voltage Source Converter (VSC) in the grid connected mode, or [42] studies the stability criterion for grid connected inverter with impedance analysis. The application of impedance analysis for microgrid is a new topic. For example, [45] studies the impedance analysis of Doubly Fed Induction Generator (DFIG) in wind farm applications. One application of impedance analysis is when the AC grid is weak, or if the transmission line connecting the converter to the grid is long. In this case, interactions will happen between the converter control and the grid. One of the most common control approaches in converters is dq control or vector control. Studies have shown that in case of grid connected vector control converter, interactions may occur if the grid is weak, or if the converter is connected to the grid through a very long transmission line. Also, [46] has reported that the vector controlled converter fails to respond to the active power commands of more than 0.4 p.u if the AC grid is weak. Analytical studies indicate the limiting factors for the vector control can be current control interactions with grid [44, 47], and or Phase-Locked-Loop (PLL) dynamics [44, 47, 48]. A few papers have studied the improvements of interactions between weak AC grids and inverters. For example, in [48], gain scheduling approach is applied to design the outer loop power/voltage, which results in the power transfer increase. Furthermore, in [46], a new control approach named Power Synchronization Control (PSC) is introduced to enhance the operation of the inverters when linked to a weak AC system. However, more studies are needed to analyze the

performance of PSC in weak AC conditions in order to generalize the comment that the PSC is an alternative for vector control in weak AC connections.

1.2.4.2 Effect of Unbalance in Microgrids

For the past few decades, PV has been one of the mostly applied renewable sources of energy in the world. The total capacity of installed PV was 300 MW in the year 2000. However, the installed capacity has been greatly increased to 21 GW in the year 2010 which is a great improvement [49]. This improvement in the application has convinced the utility planners and microgrid operators to apply PV as the most reliable source of energy in microgrids. Normally, PV is applied in microgrids to support the loads, shave the load peaks, respond to the demand, and coordinate the control of microgrids [50, 51, 52]. Compared to the wind energy, which is only available in limited locations, sun is available almost everywhere, bringing more attention to the PV.

There are different types of PV systems such as: single-phase and three-phase with different characteristics and controllers. While three phase PV systems are mostly used for higher capacities including microgrid applications and distribution level power systems, single phase PVs are mostly used for home and small sized industrial applications. Single phase PV has a good tradeoff between the generated electricity and the design complexity, reduced price, improved penetration, and high reliability. However, one should consider the effect of unbalance when it comes to the large amount of single phase PV panels applied into the power grid. The application of a large amount of single phase PV penetration into the grid will cause many problems including harmonic issues, power quality problems, reliability issues, voltage rise, or inaccurate energy/demand metering [53, 54].

Power quality and harmonic problems can be addressed by designing filters or compensators. However, the effect of unbalance should be addressed precisely. The impact of unbalance caused by harmonic currents injected by single-phase PV into microgrids are not comprehensively investigated in the literature. Moreover, it should be noted that the proper selection of controller parameters is very important in attenuating the instabilities or resonances in unbalanced microgrids. Dynamic analysis of unbalanced microgrid can be assessed. One common approach in dynamic analysis is the state space modeling and eigenvalue analysis. However, as most of the inverters are modeled in

the dq reference frame, in unbalanced conditions, dq models have an oscillating term on top of the steady state value which makes the analysis difficult. Therefore, there should be another approach to provide steady state values even in unbalanced conditions. Through various methods of dynamic analysis, Dynamic Phasor (DP) analysis offers abundant merits compared to traditional methods [55, 56, 57]. DP will change slightly when there is a sudden change in instantaneous quantities. Consequently, fast simulations with larger time step will be provided. One major advantage of DP compared to the other approaches is that it provides steady values even in unbalanced condition.

The existing literature still needs a comprehensive unbalanced microgrid model for small-signal analysis and nonlinear time-domain simulation when the microgrid is unbalanced.

1.3 Research Significance

1- PV:

This study suggests that single phase PV operations can be improved if a new design methodology can improve the performance of MPPT controllers. As discussed at the beginning of the chapter, IC MPPT algorithm provides abundant merits compared to PO and HC MPPT algorithms. However, practical implementation of IC MPPT was limited due to the complicated design procedure. Moreover, a voltage deviation term ($\frac{dV}{dt}$) in the denominator of the error signal makes the output of the controller to be infinity if $\frac{dV}{dt} = 0$. This dissertation will introduce a novel algorithm to remove the $\frac{dV}{dt}$ from the denominator of the error signal without changing the final results. Furthermore, the design procedure in this study will be simplified which enables the practical application of IC MPPT algorithms in single phase PV penetration.

2- Multi-Terminal HVDC for Offshore Wind Farm:

MTDC provides many benefits for offshore wind farm applications. However, there are some practical problems because of high amount of losses in the main DC transmission lines. This dissertation aims to improve the application of MTDC for offshore wind farms by proposing a simple method to minimize the losses in MTDC system. Although previous research tried to minimize losses in the MTDC system, all the aspects of MTDC operation was not taken

into account. This study will consider the operation of the entire system and design an adaptive controller to modify the controller parameters for HVDC converters with guaranteed minimum loss condition. The main advantage compared to the previous designs is that the designed approach does not change the basic controllers in MTDC. Moreover, it guarantees the minimum loss condition by tuning the gains adaptively. It means even if the operating mode of the system changes, the controller automatically tunes the gains for the new condition and guarantees the minimum loss condition.

3- Energy Storage System:

Decentralized controllers are recently proposed as alternatives to centralized controllers to enhance the efficiency, reliability and power quality in DERs. The application of decentralized or distributed controllers for energy storage devices were limited to the voltage/frequency control. Moreover, the literature lacks a simple design of distributed controllers for energy storage devices in microgrids with limited information exchange between batteries. Such design should work for both the grid connected and the islanded operating mode. To that end, this dissertation develops a novel distributed control for energy storage devices with a simplified dynamic model of energy storage and limited information exchange between energy storage devices. In addition, the designed approach will work for the both operating modes without modifying the controller. The design procedure uses the advanced control theory named consensus theory which has been widely used in control and robotics for synchronization of multiple agents. A 14-bus microgrid model is developed in real-time simulators including all the details to validate the superior performance of the designed controller for energy storage systems.

4- Interaction between Converter and Weak AC Grid:

One of the main issues regarding the connection of converters to the grid is the interaction problem between the converter and the weak AC grid. Previous literature showed that the conventional control of grid connected converters based on vector control results in interactions between the grid and the converter. An alternative has been proposed for the

conventional control and named as Power Synchronization Control (PSC), which uses the synchronous generator idea to synchronize the converter with the grid even in weak AC conditions. The practical implementation of PSC is still under investigation, as it has not been extensively tested for stability, or resonance problems. Moreover, the decoupled controllers in grid connected converters are no longer considered as a Single Input Single Output (SISO) system and hence they are Multiple Input Multiple Output (MIMO). Therefore, MIMO analysis technique should be conducted to justify the operation of the newly introduced PSC in weak AC grids. This dissertation will conduct an impedance analysis for both types of grid connected converter controls (vector control and PSC). The analysis uses the MIMO Nyquist stability criterion and singular value plots to compare these two types of controllers in multiple conditions. To validate the analysis results, this dissertation uses the real-time simulation platform with RT-LAB.

5- Unbalanced Microgrid:

It was mentioned earlier that single phase PV penetration is getting more attention for home and industrial applications. With the massive amount of single phase PV systems installed in microgrids, a large amount of unbalanced current will be injected into the system. There has not been enough evidence for investigating the effect of unbalance in microgrids, and literature lacks a comprehensive model capable of considering all the dynamics and nonlinear behavior of single phase PV in microgrids. Therefore, this dissertation implements DP as the most suitable analysis approach for reflecting instabilities and unbalanced situations to analyze an unbalanced microgrid composed of three phase balanced elements and a single phase PV. The DP analysis will be conducted for every component of the microgrid and the entire model will be incorporated to shape a single dynamic model. Various analysis approaches such as root-locus or eigenvalue analysis will be carried out to find the stability limits of unbalanced microgrids. Moreover, non-linear time domain simulations of the same microgrid model including all the details will be carried out to validate the analysis results.

1.4 General Problem Statement

General idea of this dissertation is to improve the power quality, performance and stability of microgrid operation. As expressed earlier, a typical microgrid can have three different levels. In general, this dissertation aims to improve the performance of microgrids in all the mentioned levels such as: microgrid model, microgrid lower level control, and microgrid upper level control. For each level, sample problem is selected, extensive literature review is conducted to find the limitations and deficiencies of the proposed approaches in the literature, and finally a new method is presented to improve the results compared to the existing literature. In order to validate the proposed methods, for each topic, extensive analysis and experiments have been conducted and a detailed comparison with existing approaches is carried out.

1.5 Research Objectives

The key contributions of this dissertation are:

- 1- Improving the performance of Maximum Power Point Tracking (MPPT) for single phase PV systems
- 2- Minimizing the DC losses in offshore wind farms based on multi-terminal HVDC transmission systems via adaptive droop control
- 3- Designing a distributed control algorithm based on consensus theory for energy storage systems in microgrids with limited information exchange
- 4- Applying MIMO impedance analysis for HVDC converters connected to weak AC grids
- 5- Applying dynamic phasor analysis to analyze an unbalanced microgrid with single phase PV system

The first two objectives plan to enhance the performance of lower level control in microgrids, objective number 3 aims to improve the upper level control in microgrids and objectives number 4 and 5 try to conduct microgrid modeling and analysis through advanced analysis techniques.

1.5.1 Sub-Objectives

To accomplish the above objectives, the sub-objectives are as follows:

- 1- Detailed single phase PV model is studied
- 2- As the single phase PV controllers in the literature are based on a continuous time domain, a discrete domain technique is used to convert the controllers from continuous to discrete for real-time simulators
- 3- A detailed single phase PV model for the traditional and proposed MPPT algorithms are developed in an RT-LAB real-time simulation platform
- 4- A 6-terminal HVDC system including three offshore stations and three onshore stations is modeled in an RT-LAB real-time simulation platform
- 5- A DC circuit analysis is conducted for the 6-terminal HVDC system including controllers in order to minimize the losses
- 6- Adaptive droop control theory is applied to the 6-terminal HVDC system and the results have been compared to traditional approaches
- 7- Detailed battery models are simulated in the RT-LAB platform
- 8- A 14-bus microgrid model composed of three energy storage devices, an induction machine, transmission lines and multiple loads are simulated for grid connected and islanded operating modes in the RT-LAB test-bed
- 9- Upper level and lower level controllers are installed and tested for the 14-bus microgrid model
- 10- Battery energy storage dynamic models are simplified for analysis
- 11- Consensus theory is applied to the simplified energy storage model and results are analyzed in MATLAB®/Simulink model for simplified dynamics

- 12- A detailed 14-bus microgrid model is used and the consensus upper level coordination control is applied to the energy storage devices for islanded mode and grid connected operations
- 13- A back to back HVDC model is simulated in the RT-LAB for impedance analysis cases
- 14- Impedance analysis is conducted to derive the impedance of converters with vector control and power synchronization control
- 15- Nyquist stability criterion for an MIMO system is used to analyze the impedance of the vector control and the power synchronization in different conditions
- 16- Singular value analysis is conducted for the MIMO system with the vector control and the power synchronization in different scenarios
- 17- Power synchronization and vector control are applied to the back to back HVDC model in order to validate the impedance analysis results in weak AC grid connections
- 18- Dynamic Phasor (DP) model is derived for single phase PV system
- 19- DP model is derived for an unbalanced induction machine in positive-negative-zero sequence reference frames
- 20- DP model for an entire microgrid model is derived
- 21- Eigenvalue and root-locus analysis are conducted to test the dynamic phasor model of an entire microgrid
- 22- Microgrid model is built in MATLAB®/Simpowersystem toolbox in order to validate the dynamic phasor analysis results

1.6 Chapter Breakdown

This dissertation is divided into 8 main chapters for different levels of microgrid. In each chapter, a problem is formulated and corresponding solution with detailed analysis and simulations are also provided. The structure of the dissertation is organized based on the following:

- Chapter 2 provides the introduction of upper level control, lower level control and microgrid analysis approaches.
- Chapter 3 presents the lower level control improvements for a single phase PV system.
- Chapter 4 presents the lower level control improvements for multi-terminal HVDC systems.
- Chapter 5 presents the upper level distributed control based on consensus theory for battery energy storage systems in microgrids.
- Chapter 6 develops impedance analysis for converter-grid interaction analysis in microgrids.
- Chapter 7 investigates the unbalance issue in microgrids based on dynamic phasor approach.
- Chapter 8 summarizes the research findings and future research plans.

CHAPTER 2

MODELING AND CONTROL IN MICROGRIDS

2.1 Introduction

This chapter is dedicated to lower level and upper level control of distributed energy resources (DERs) and microgrids. Moreover, modeling techniques applied to DERs analysis in microgrids and power systems are also included and discussed in detail. Generally, each DER is composed of a power electronic device which converts energy from one form to the other. This device, which is called converter, performs energy conversion from AC to DC and/or DC to AC in each DER. The most commonly used type of energy conversion in DERs is DC to AC. The main task is to convert a constant DC voltage to a sinusoidal AC waveform by controlling the switching of each converter. VSC is the most popular type of converter in microgrids and DERs. However, generating a sinusoidal waveform from a DC voltage is not the only objective of a converter. As a result, controllability of the converter for power/voltage/frequency is desirable. By adding extra control loops to the pulse generation unit of each converter, multiple control objectives can be achieved. These objectives are considered as lower level control of a converter. An example for lower level control would be active/reactive power (PQ) control of a converter, or voltage/frequency (VF) control of converters. When there are more than one converters in the system, lower level droop control is used to share the control between converters based on the capacity of each converter. Upper level control on the other hand is in charge of generating the reference power/voltage/frequency based on the information of the entire system. This upper level controller can be a centralized controller, or a decentralized/distributed controller. In this dissertation, the distributed controller concept is used to investigate the upper level controller design in DERs. Analysis tools such as impedance analysis and DP can be used to evaluate the system stability when there is a converter connected to

a grid, or in case of unbalanced microgrid operation. Basic theory behind the impedance analysis and DP are also covered in this chapter.

2.2 Methodology

2.2.1 Voltage Source Converters (VSC)

VSC is a type of converter where a DC side voltage retains its polarity and the direction of the converter output power is decided by the direction of DC current flowing into the DC side. Basic diagram of a three-phase voltage source converter is illustrated in Fig. 2.1. In three phase power system application, this VSC is normally interfaced with the main AC system through a three-phase transformer. The conversion process in most of DERs in microgrids takes place in VSCs. The VSC in Fig. 2.1 is linked to the main grid via a filter.

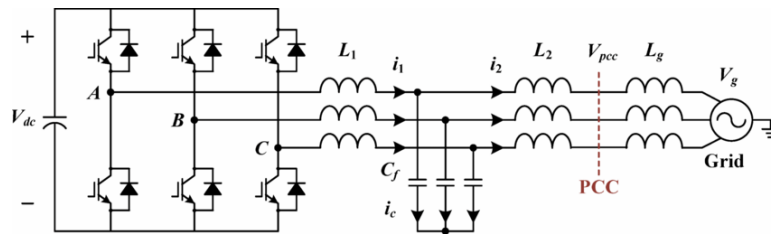


Figure 2.1. Basic diagram of a three phase voltage source converter connected to grid.

2.2.2 Control in DERs

Fig. 2.2 shows a typical structure of a microgrid. It can be connected to the main grid, or DERs can operate autonomously (islanded mode). Control structures are essential for the operation of DERs in microgrids. Based on grid connected or islanded operation of a microgrid, these control schemes may differ. These main control algorithms can be mentioned as frequency and voltage control, active and reactive power control between DER and main grid, synchronization of microgrid with main grid, energy management between DERs, and economic optimization. In order to standardize the operation of DERs in microgrid, hierarchical control of DERs has been proposed. In this control approach, primary and secondary controllers are defined.

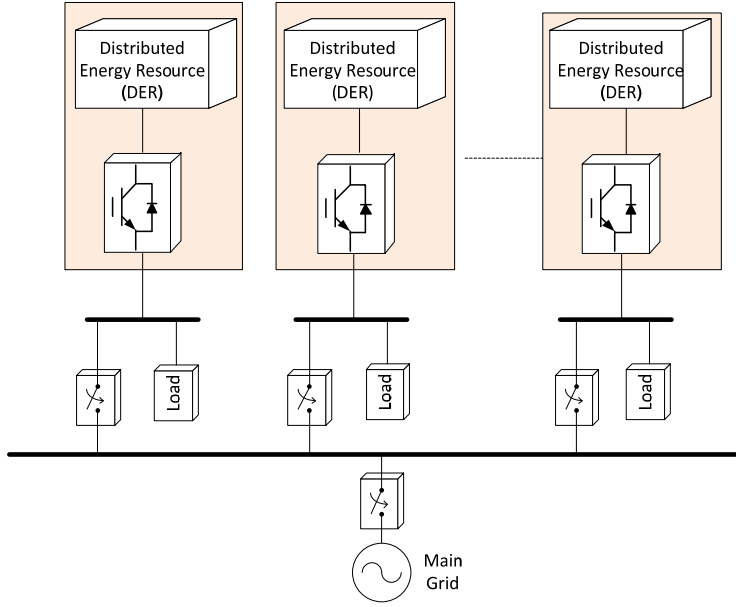


Figure 2.2. Microgrid structure in islanded mode and grid connected.

2.2.3 Lower Level Control/Primary Control

Primary control of DERs is the first level of control and is independent of the other control loops. Primary control mainly deals with the local control loops of DER unit. The key control loop in the primary controller is the inner current controller which controls the converter output current and protects the converter from over-currents caused by grid faults. Primary control may also be composed of voltage control loops, virtual impedances and active/reactive power controllers. Depending on the mode of the operation or type of the DER, these primary control loops might vary. Such a control loop has been illustrated in Fig. 2.3. If there are multiple converters operating in parallel, each converter will be supplemented with power-frequency droop and reactive power-voltage droop controllers as decentralized controllers for power sharing purposes. This level does not require a communication between DERs. Therefore, to achieve an optimal global controllability, secondary controllers are defined.

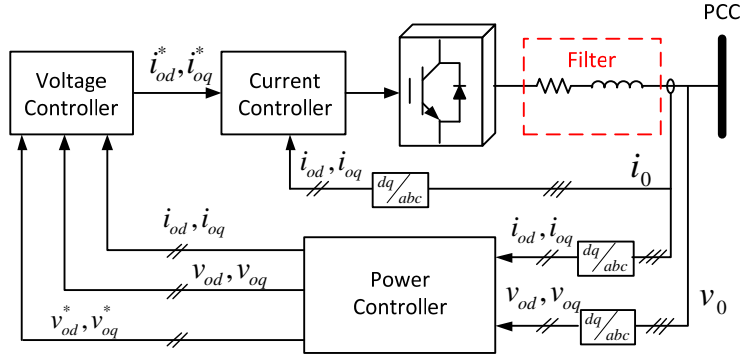


Figure 2.3. Lower level control of DERs.

2.2.4 Upper Level Control-Centralized Approach

As the primary controllers are local and there is no communication between DERs, secondary controllers/upper level controllers are used to achieve a global controllability. Secondary controller can be centralized; it means there are multiple DERs locally controlled by primary controllers and a secondary controller measures signals through remote sensing and sends the reference signal to the primary controllers of each DER through communications. Such a controller is illustrated in Fig. 2.4. One advantage regarding this controller is that the communication structure is only one way, as the secondary control sends a unified signal to each DER. The main drawback regarding this type of control is that any failure on secondary controller will stop the operation of secondary controller in the entire microgrid.

2.2.4.1 Centralized Secondary Control-Frequency Control

Frequency control is one of the major control algorithms applied to centralized secondary controllers. Traditionally, power systems were enhanced with secondary controller, which was simply a Proportional Integral (PI) controller regulated the frequency of the system, called Automatic Generation Control (AGC). Same concept has been used in microgrid application. For multiple converters enhanced with power-frequency droop, as the load changes, the frequency will change, in which case, a secondary controller can restore the frequency back to the nominal value. A unified PI controller is implemented to regulate the frequency deviations in the entire microgrid and

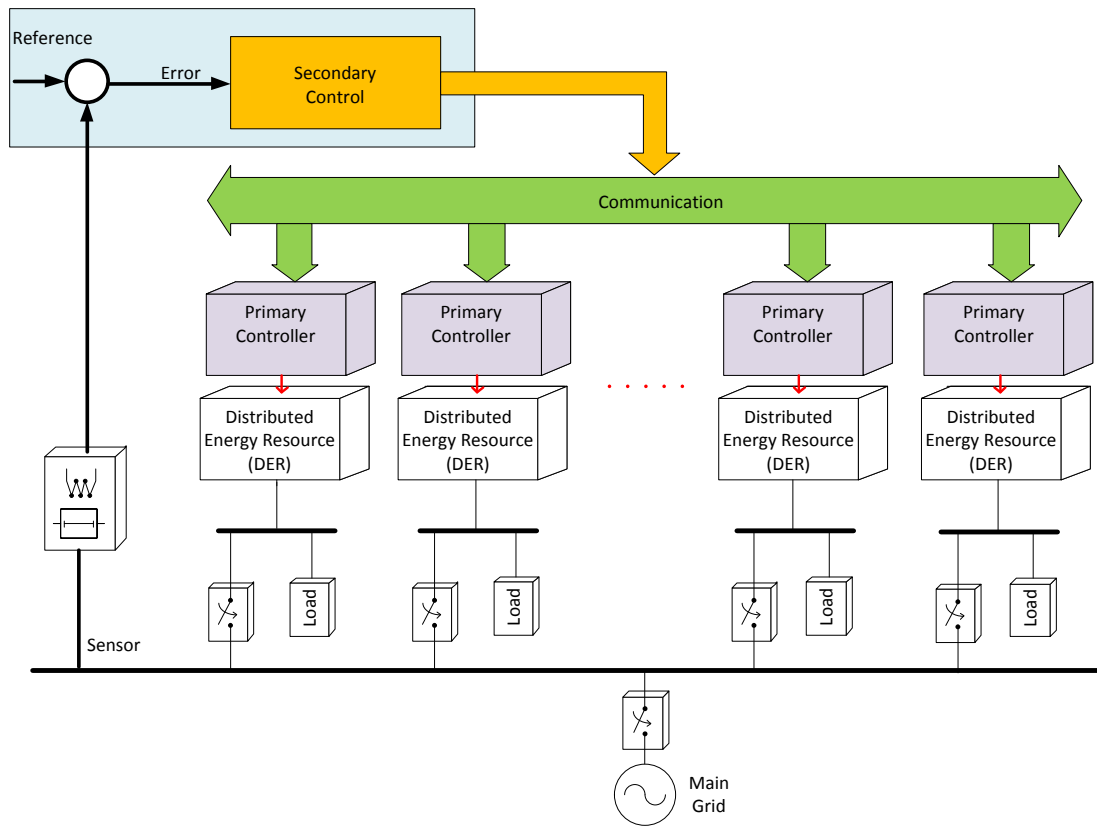


Figure 2.4. Upper level control of microgrids in centralized approach.

the output of this centralized secondary controller will be sent to all the DER units in order to compensate for the frequency.

2.2.4.2 Centralized Secondary Control-Voltage Control

Same notion as centralized secondary frequency control can be used for centralized secondary voltage control. When the voltage in a microgrid is not within the limit, a centralized secondary controller will regulate voltage deviations in the microgrid and sends the unified voltage restoration signal to the primary controllers of each DER.

2.2.5 Upper Level Control-Decentralized Approach

Decentralized control or distributed control is a type of secondary control where instead of single centralized secondary controller, there is a distributed secondary controller implemented for each DER. The distributed secondary controller can greatly improve the performance of the whole system, as single point of failure is not an issue anymore. The idea is to incorporate the primary and secondary together as a local controller for each DER, illustrated in Fig. 2.5. Secondary control is located between communication system and the primary control. In this case, there is a two-way communication link between the neighboring DERs, limiting the information transfer in the entire microgrid. Secondary controller in distributed approach can control voltage, frequency, or even reactive power sharing among DERs. However, the main contribution in this dissertation is to design a secondary controller for energy storage system based on distributed approach with limited information exchange among energy storage units in a microgrid. The final goal would be synchronization of power and energy for each energy storage.

2.2.6 Distributed Consensus Control Theory

Consensus theory is a useful theory for synchronization of the network of dynamic agents. It has been broadly employed in control systems and robotics. The application of consensus theory has enabled the distributed secondary control for DERs and microgrid applications to accomplish the global synchronization. Below is a brief introduction of consensus theory. A comprehensive description about implementation in microgrids will be covered in the following chapters.

2.2.6.1 Basics of Graph Theory

In a multi-agent system composed of many Distributed Generation (DG) units, the communication system can be modeled by a directed graph or simply digraph represented as: $G = [V_G, E_G, A_G]$. V_G is a set of N vertexes (nodes), $V_G = [V_1, V_2, \dots, V_n]$, $E_G \subset V_G \times V_G$ is the set of edges, where edge is a set of pairs of nodes. In our case, each DER is treated as a node in a multi-agent system, i.e. a microgrid. A_G is the $n \times n$ adjacency matrix that describes if two nodes are neighbors or at

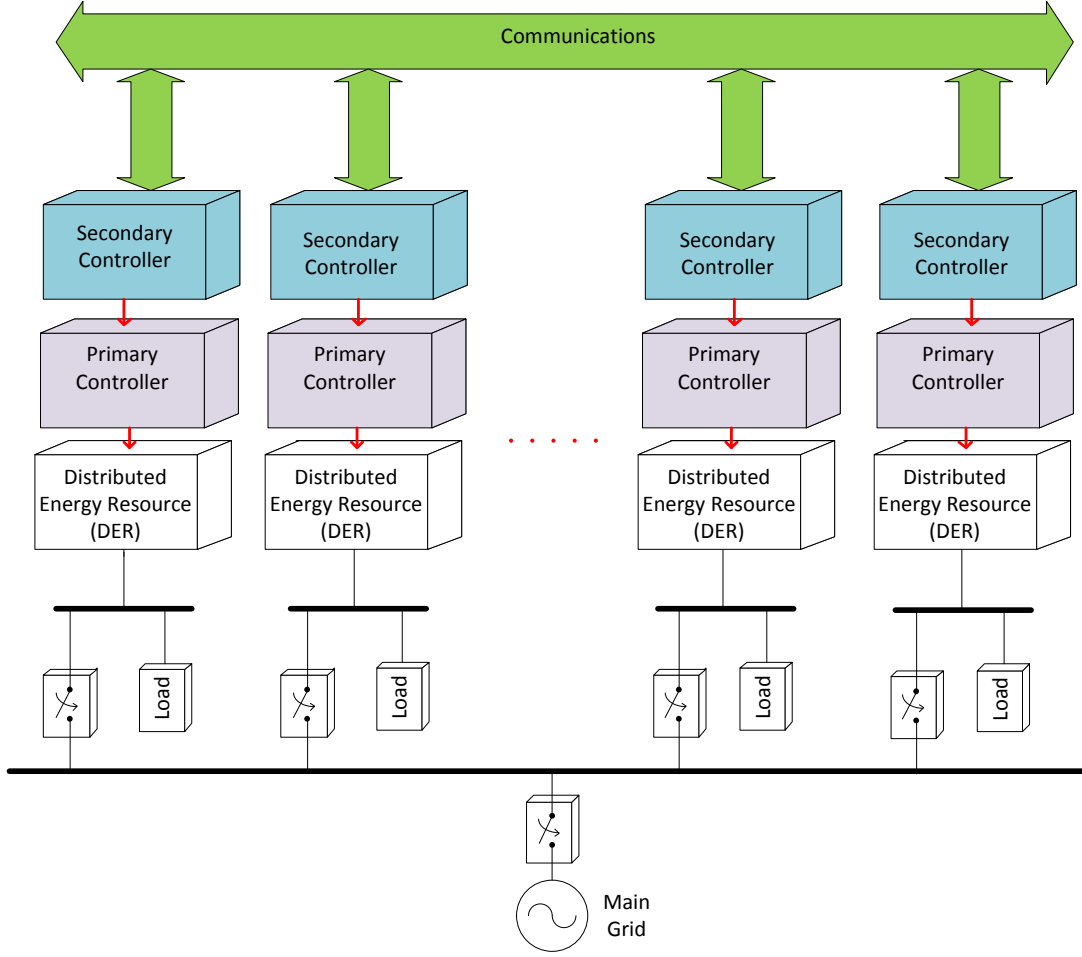


Figure 2.5. Distributed control of microgrids; upper level decentralized approach.

least have a common edge. $A_G = [a_{ij}]_{n \times n}$, and a_{ij} is the total number of common edges between node i and node j defined as:

$$a_{ij} = \begin{cases} 1 & \text{if } (j, i) \in E_G; \\ 0 & \text{otherwise.} \end{cases}$$

Two nodes are to be neighbors if there is at least a common edge between them. For example, node i is a neighbor of node j if $(V_i, V_j) \in E_G$. For a digraph G , if node i is a neighbor of node j , node j can get information from node i but it does not guarantee that node i also can get information from node j .

The other two important definitions are for in-degree (D) and Laplacian matrix (L) defined as:

$$D = \text{diag}[d_i] \in R^{n \times n}, d_i = \sum_{j=1}^n a_{ij}, \text{ and } L = D - A_G.$$

2.2.6.2 Consensus Based Secondary Control Design

In a multi-agent system composed of communication graph where each DER can communicate with its neighbors, consensus can be achieved using consensus theory design for network of dynamic agents. In this case, each DER will be formulated by nonlinear equations representing the state space model in the form of: $\dot{x}_i = Ax_i + Bu_i$. It is noted that, x_i is the state vector of each DER, A and B are state matrices of the nonlinear dynamic model, and u_i is the input of the DER.

Now, u_i can be designed in order to ensure that the states of the DERs will be synchronized based on consensus objective. The objective of the consensus based control is to synchronize the multi-agent systems. The final goal of synchronization can be accomplished if the state difference of DERs considering the state of its neighbors is sent to DER as an input of the controller. It is also noted that the $x = [x_1, x_2, \dots, x_n]^T$ is a global vector of state variables, and $u = [u_1, u_2, \dots, u_n]^T$ is the global vector of inputs in the systems. It is explained in [36] that in a local voting protocol, the consensus is reached by the agents (in this case DERs) in a balanced communication graph if the control input is selected as the average of agents initial states. The control input is designed as:

$$u_i = cK \sum_{j=1}^n a_{ij}(x_j - x_i) \quad (2.1)$$

where, x_j is the state of the DER_j in a microgrid. Moreover, c is a positive scalar coupling gain and K is the feedback control matrix variable. In order to analyze the stability of the proposed design, the global closed loop dynamics of the system should be considered. Adding the designed control input (2.1) into the state space equation of the system:

$$\dot{x} = Ax + cBK \sum_{j=1}^n a_{ij}(x_j - x_i) \quad (2.2)$$

The stability criteria to design the auxiliary control requires the A and B to be stabilizable. It means there should exist a matrix S such that the eigenvalues of $A - BS$ has strictly negative real parts. Moreover, a symmetric matrix Y is called positive definite if $x^T Y x$ is positive for all non-zero column vectors of x , and is zero only for $x = 0$.

Now, in order to design the stable auxiliary control, consider A and B are stabilizable and matrices Q and R are positive definite, the feedback gain K in (2.1) can be designed as:

$$K = R^{-1} B^T P_1 \quad (2.3)$$

where P_1 is the unique positive definite solution of the control algebraic Riccati equation (ARE) [37]:

$$A^T P_1 + P_1 A + Q - P_1 B R^{-1} B^T P_1 = 0 \quad (2.4)$$

Then, if the eigenvalues of the Laplacian graph matrix (L) are denoted as λ_i , the stability properties of the global system dynamics in (2.2) are equivalent to the stability properties of:

$$\dot{Z}_i = (A - \lambda_i c B K) z_i \quad i = 1, 2, \dots, n \quad (2.5)$$

Then the stability criteria requires $(A - \lambda_i c B K)$ to be Hurwitz, or all of its eigenvalues have a strictly negative real part. This condition requires c to be selected as:

$$c = \max \left(\frac{1}{2 \min \operatorname{Re}(\lambda_i)}, 1 \right) \quad i = 2, \dots, n \quad (2.6)$$

The design procedure mentioned above will assure the synchronization of the distributed secondary controllers in a multi-agent microgrid system.

2.2.7 Microgrid Modeling Techniques

One of the main challenges in microgrid and DER operation is the stability limitations and controllability of converters. Therefore, it is crucial to analyze the system before operation. Analysis tools can be implemented in microgrid design in order to find the unstable points in multiple operating conditions, or stability limits caused by different types of controllers in DERs. Such an analysis approach should consider all the details of the system including the nonlinearities and control characteristics. In this dissertation, two well-known analysis approaches are applied for DERs and microgrids. The first method is the impedance analysis, which is a useful tool to evaluate the resonances and interactions between the DER converters and the main grid. The second technique is the dynamic phasor, which can be used to model the nonlinearities even in unbalanced situations. A brief introduction of these theories is provided in the following.

2.2.7.1 Impedance Analysis

As the grid connected converters are controlled in current injection mode, a Norton equivalent circuit should be developed to set up an impedance based stability criterion. The small signal model of a converter connected to a grid then can be represented by Fig. 2.6.

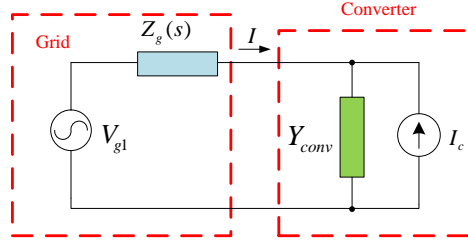


Figure 2.6. Small signal model of a converter connected to grid.

Referring to Fig. 2.6, the current flowing from grid to converter can be derived by [42]:

$$\begin{aligned}
 I(s) &= \frac{V_{g1}(s) - Z_{conv}(s)I_c(s)}{Z_g + Z_{conv}} \\
 &= \left[\frac{V_{g1}(s)}{Z_{conv}} - I_c(s) \right] \frac{1}{1 + Z_g(s)/Z_{conv}(s)}
 \end{aligned} \tag{2.7}$$

Now, under the main assumption that the grid voltage is stable without the converter ($V_{g1}(s)$ is stable) and inverter voltage is also stable when the grid impedance is zero, the left hand side of the (2.7) is stable. As a result, stability of the current in the converter grid system, shown in Fig. 2.6, is only related to the stability of $\frac{1}{1+Z_g(s)/Z_{conv}(s)}$. Impedance analysis starts with this observation that $\frac{1}{1+Z_g(s)/Z_{conv}(s)}$ is a negative feedback closed loop transfer function with forward gain of 1 and feedback gain of $Z_g(s)/Z_{conv}(s)$. To analyze the stability of current, referring to linear control theory, if $Z_g(s)/Z_{conv}(s)$ (or $Z_g(s)Y_{conv}(s)$) satisfies the Nyquist stability criteria, stability margin of the system is achieved [42].

2.2.7.2 Dynamic Phasor Analysis

The Fourier series of a time domain signal $x(\gamma)$ for the time interval of $\gamma \in (\gamma - T, t)$ [58] is defined as:

$$x(\gamma) = \sum_{k=-\infty}^{\infty} X_k(t) \cdot e^{jk\omega\gamma} \quad (2.8)$$

where $\omega = \frac{2\pi}{T}$ is the angular frequency and $X_k(t)$ is called the k^{th} complex Fourier coefficient. The Fourier coefficient is defined as dynamic phasor. If states of the system vary slightly with time, small signal analysis provides the best results. The dynamic phasors have the capability of varying slightly with time, and therefore are the perfect candidates for small signal analysis. Based on the above descriptions, the dynamic phasors of a complex time domain waveform $x(\gamma)$ are calculated based on [58]:

$$X_k(t) = \frac{1}{T} \int_{t-T}^t x(\gamma) e^{jk\omega\gamma} d\gamma = \langle x \rangle_k(t); \quad (2.9)$$

Parameter k should be selected in a way to result in a proper approximation of the original waveform. In modeling the power system components, as capacitors and inductances dynamics are introduced with derivative, dynamic phasor should also be defined for derivative functions using (2.8).

$$\left\langle \frac{dx}{dt} \right\rangle_k = \frac{dX_k}{dt} + jk\omega X_k; \quad (2.10)$$

This characteristic is the main feature of the DP modeling which will be employed in this dissertation to derive the DP model for an unbalanced microgrid.

2.3 Discussions

This chapter presents a basic introduction to microgrid modeling and control. Generally, microgrid has two levels of control; lower level and upper level. Lower level control is the basic control designed for each DER in order to perform a basic task. Upper level control is designed on top of the lower level control to achieve more controllability with DERs. There are two types of upper level control, centralized and decentralized. Since decentralized controllers provide a lot of advantages compared to centralized controllers, they are of interest. Consensus theory is selected in this dissertation for upper level control and a brief introduction is included. Microgrid modeling is also very important in order to find the stability limitations or operating point conditions in microgrids. In this dissertation, impedance modeling and DP are selected as two useful tools to analyze microgrids in different conditions and brief theory overview is also included.

CHAPTER 3

MPPT CONTROL FOR SINGLE PHASE PV

This chapter ¹ introduces a real-time modeling technique for single phase PV systems and proposes a new MPPT approach with high efficiency and fast response.

3.1 Introduction

PV is considered as a widely spread source of renewable energy due to its low operational cost, low maintenance cost, and renewable nature without pollution. According to the literature, PV cells will become the most important alternative renewable energy sources by 2040 [15, 16, 59, 60, 61].

Real-time digital simulation based high-fidelity modeling can give a close-to-reality representation of the system dynamic performance. In addition, simulation in real-time span can be achieved easily. Such simulation model can be used for prototype operation and control tests.

Modeling PV systems in real-time digital simulation has been mentioned in [62] where a PV serving a load through a DC/DC converter is modeled and simulated in Real Time Digital Simulator (RTDS). In another paper [63], a PV cell, its dc-link capacitor and a DC chopper are modeled in RT-Lab, while the physical controller for the chopper is integrated into the software simulation model through RT-Lab interface. A grid-connected PV system has a more complicated control system. Modeling such system has not been observed in the literature. The first objective of this chapter is to model a single-phase single-stage PV system in RT-Lab ².

Control of the interfacing DC/AC converter, including Proportional Resonance (PR) current control, Phase Locked Loop (PLL) and MPPT will all be modeled in RT-Lab. In addition, an

¹This chapter was published in Electric Power Systems Research Volume 123, pp. 85-91, June. 2015. Permission is included in Appendix B.

²This part was published in IEEE General Meeting Conference on Power & Energy Society, July. 2015 pp. 1-5. Permission for this part is included in Appendix B

improved MPPT will be proposed and modeled in this chapter. Various types of MPPT algorithms have been proposed in recent years, *e.g.*, Hill Climbing (HC) [64, 65], Perturb and Observe (PO) [66, 67, 68, 69], and Incremental Conductance (IC) [70, 71]. Among these types of algorithms, HC and PO are two commonly used approaches because of their simple control structures. The disadvantages associated with these methods are: increased losses at steady state due to large perturbation around maximum power point; reduced dynamic performance when there is a sudden change in irradiance or at any other sudden dynamic event [72, 73, 74], and large oscillations around the maximum point [75].

On the other hand, IC methods are based on the fact that the slope of the PV array power curve versus voltage is zero at the Maximum Power Point (MPP). IC method has several advantages compared to the PO method. It can exactly determine when the Maximum Power Point (MPP) is reached. In a PO method, there are oscillations around the MPP. Accuracy of the IC method in tracking the maximum power or responding to the irradiance changes is more than that of a PO method [72, 73]. Less ripples in output power are experienced during the operation compared with PO method [75]. In addition, dynamic behavior of the IC based methods are faster when an operating point change is applied to the system [75].

Complexity of the IC method have limited the widespread implementation of this algorithm [73]. Most of the previous researchers have focused on improving the dynamic response and steady state accuracy of the IC method [75, 76, 77, 78, 79]. In [75], it is demonstrated that the dynamic response of the IC method can be greatly improved if a Proportional Integral (PI) controller is used. Moreover, if the output of the PI controller aims to modify the PV current instead of the PV inverter's duty cycle, the dynamic response improves significantly. A variable step-size IC MPPT is proposed in [80]. The step size is automatically adjusted according to the derivative of power to voltage ($\frac{dP}{dV}$) of a PV array. The step size will become tiny as $\frac{dP}{dV}$ becomes very small around the MPP. Thus, it provides a great accuracy at steady state and thus the dynamics of the MPPT will be improved. However, the proposed method has added more complexity to the IC algorithm.

In this dissertation, a new algorithm is proposed to improve the steady state response and dynamic behavior of MPPT. In the proposed method, instead of using the traditional incremental

error $(\frac{dI}{dV} + \frac{I}{V})$, which could lead to spikes when dV is approaching zero, the proposed error will no longer contain dV at the denominator. This approach will remove the conditional statements from the IC-PI MPPT and lead to improvement in dynamic performance of the MPPT algorithm.

3.2 Methodology

3.2.1 System Configuration

The PV system configuration is illustrated in Fig. 3.1. The model is composed of a PV array, an inverter, and a filter. The PV array is composed of a number of parallel connected PV strings. These PV strings consist of a number of series connected PV cells. Parameters of these cells will be different for different commercial PV models. Each cell in a module can be modeled as a photo-generated current source in parallel with a diode and a shunt resistor, R_p , as well as in series with a series resistor, R_s as shown in Fig. 3.1. Main parameters of the system are expressed as: $L_a = 10$ mH, $L_b = 20$ mH, $C_f = 10$ μ F, $V_{gf} = 230$ V, Sunpower PV panel: $V_{PV} = 440$ V, $P_{PV} = 2.45$ kW. I_{ph} is photo-generated current and is proportional to the irradiance which will be normalized by

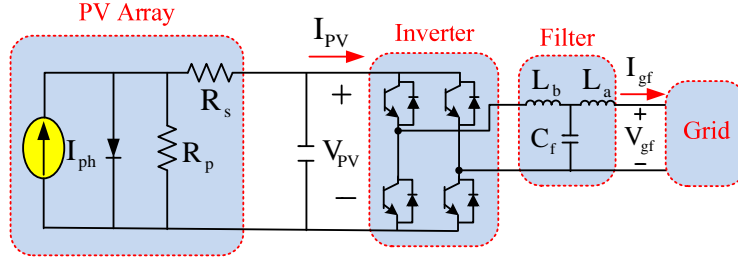


Figure 3.1. Topology of a single-phase PV grid integration system.

the short circuit current (I_{sc}) [81]:

$$I_{ph} = A_{ph} \cdot I_{sc} \cdot E_e \quad (3.1)$$

where E_e is the effective sun radiance considering the effect of incidence angles, transmission through glass, encapsulant and spectral responses of the cell. A_{ph} is the proportionality factor related to the cell temperature and is usually close to 1. Current through the diode can be represented by

the Shockley equation in the following [81]:

$$I_{\text{diode}} = I_{\text{sat}} e^{\frac{V_{\text{PV}} + I_{\text{PV}} \cdot R_s}{m V_T}} \quad (3.2)$$

where I_{sat} is the diode saturation current which strongly depends on the cell temperature. Cell voltage and current are notated as V_{PV} and I_{PV} , respectively. m is the diode factor, a measure of ideality of the diode, usually a number between 1 and 2. In situations where the PV array is modeled by two parallel diodes, m is set to 1, the ideal factor.

V_T is the thermal voltage related to Boltzmann's constant k , q is the elementary charge, and the cell temperature is T_{cell} [81].

$$V_T = \frac{k \cdot T_{\text{cell}}}{q}. \quad (3.3)$$

3.2.2 PV Control

The main block diagram of the PV control is illustrated in Fig. 3.2. The inputs of the MPPT block are the measurements from the PV array ($I_{\text{PV}}, V_{\text{PV}}$). The output of the MPPT block is then modified to shape the reference PV AC current magnitude. The measured AC current of the grid is then compared with the reference signal and the error will be sent to the Proportional Resonance (PR) controller. The output of the PR controller is then sent to the Pulse Width Modulation (PWM) block to generate pulses for the PV inverter. A single-phase Phase-Locked-Loop (PLL) is used to synchronize the PV reference current with the AC grid in Fig. 3.2. Since the real-time simulators are working in discrete time domain, all the controllers are modeled in discrete time domain.

3.2.3 Discrete Time Single Phase PLL

The primary role of PLL is to provide a reference phase signal synchronized with the AC systems. The reference phase is then used to generate a carrier waveform for firing pulses in control circuits of converters. PLL has the capability to dynamically change the reference phase due to

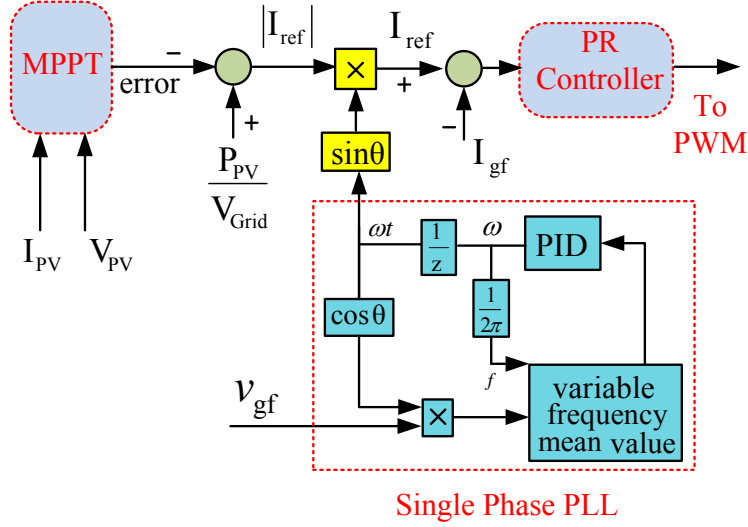


Figure 3.2. Block diagram of PV control system.

any dynamic variations in AC systems, ensuring synchronization of the converter's output with the AC system.

The PLL model in Simpower systems was developed by Pierre Giroux in 2007. Description of the PLL models can also be found in [82]. The continuous time PLL model will be converted to a model in discrete time. The main block diagram of the discrete time PLL is illustrated in Fig. 3.3, derived based on Fig. 3.2. The input of the PLL is the grid AC voltage, v_{gf} , and the output

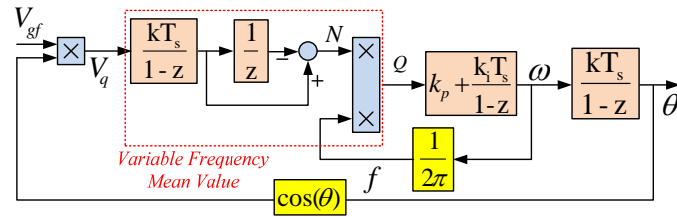


Figure 3.3. Discrete-time model of a single-phase PLL for the PV system.

is the frequency or angle, which is synchronized with the grid. Furthermore, there is a variable frequency mean value calculator represented by a simple integrator and a delay block. Suppose v_{gf} is sinusoidal and can be expressed as $v_{gf} = V_{gf} \sin \theta_g$. Then multiplied by $\cos \theta$, we have

$$V_q = \frac{1}{2} V_{gf} (\sin(\theta_{gf} + \theta) + \sin(\theta_{gf} - \theta)). \quad (3.4)$$

There are two components in V_q , one is a high frequency component, and the other is a low frequency one. If the angular speeds of θ_{gf} and θ match each other, the second component is a DC value. After passing the integrator, the effect will be mainly due to the second component, as the integration of the high-frequency component will be around zero. The main objective of the PI controller is to bring the second component in V_q to zero, i.e., $\theta_{gf} = \theta$. Thus, PLL can obtain the angle of v_{gf} . The frequency of the grid voltage can also be obtained.

3.2.4 Discrete Proportional Resonant (PR) Controller

A PR controller provides an infinite gain in a very narrow bandwidth that is centered at the resonance frequency (ω). As a result, steady-state error is eliminated at the resonance frequency ω . Therefore, a PR controller can track a sinusoidal reference signal. For a single-phase PV converter, the error signal is the mismatch of the grid AC reference current and measured grid instantaneous current. The general control block of the PR controller is illustrated in Fig. 3.4. The Bode plots of

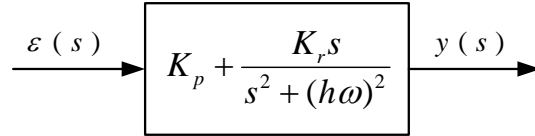


Figure 3.4. Control diagram of PR controller.

a PR controller with different resonance gains are illustrated in Fig. 3.5. It can be observed that at frequencies close to 377 rad/s or 60 Hz, the PR controller's gain is very large. As a result, the closed-loop system will have a very small gain at this frequency. Therefore, steady-state error at ω will approach to zero. In this study, the PR controller for the single-phase PV has been designed to compensate the high order frequencies of: 3rd, 5th, 7th, and 9th. The PR controller will be modeled in discrete time for RT-lab. The original system can be expressed as follows.

$$y(s) = \underbrace{K_p \varepsilon(s)}_{y_1(s)} + \underbrace{K_r \frac{s}{s^2 + \omega^2} \varepsilon(s)}_{y_2(s)} \quad (3.5)$$

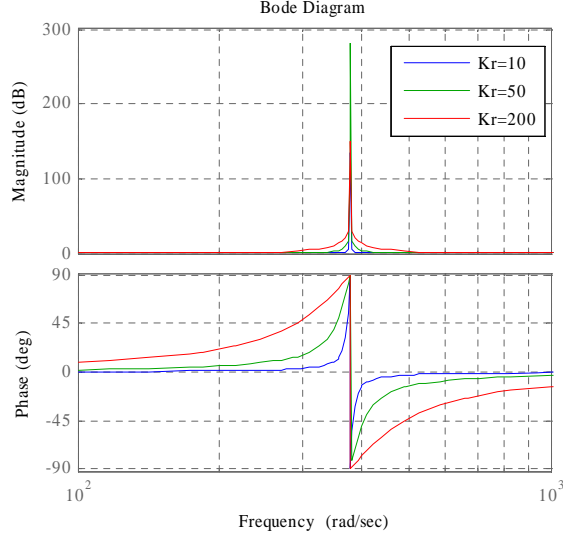


Figure 3.5. Bode plot for PR controller for different K_r , while $K_p = 1$ and $\omega = 377\text{rad/s}$.

The proportional block will remain the same in the discrete domain. In contrast, converting $y_2(s)$ into the discrete form requires derivation. The procedure can be found in [83] and also described as follows. Rearranging $y_2(s)$ will lead to:

$$\begin{aligned}
 y_2(s) &= K_r \frac{s}{s^2 + \omega^2} \varepsilon(s) \\
 \frac{s^2 + \omega^2}{s^2} y_2(s) &= \frac{K_r}{s} \varepsilon(s) \\
 y_2(s) + \frac{\omega^2}{s^2} y_2(s) &= \frac{K_r}{s} \varepsilon(s) \\
 y_2(s) &= \frac{1}{s} \left[K_r \varepsilon(s) - \frac{1}{s} \omega^2 y_2(s) \right]. \tag{3.6}
 \end{aligned}$$

Defining a new variable z , the simplified model of $y_2(s)$ is expressed by:

$$\begin{cases}
 y_2(s) &= \frac{1}{s} [K_r \varepsilon(s) - z(s)] \\
 z(s) &= \frac{1}{s} \omega^2 y_2(s).
 \end{cases} \tag{3.7}$$

Converting (3.7) to the discrete form is now limited to an integrator, which should be changed from s -domain into discrete time integrator, where $\frac{1}{s}$ corresponds to $\frac{T_s}{1-z^{-1}}$. The block diagram of

the proposed controller is illustrated in Fig. 3.6, but due to the space limitations, only the first harmonic has been shown here. The PR controller aims to control the grid side AC current. To

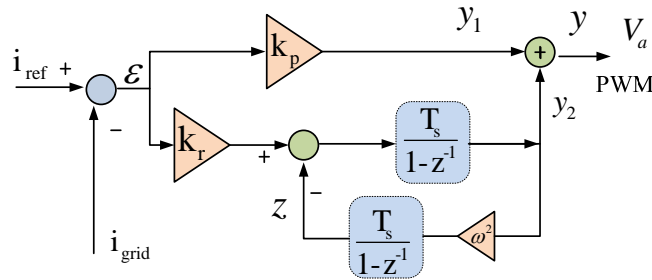


Figure 3.6. Structure of PR controller.

reach this goal, the error of the reference PV current and measured PV current will be used as the input for the PR controller. The reference current magnitude generated from the output of the MPPT block will be synchronized with the grid voltage before sending it to the PR controller. The synchronization steps will be carried out in a single-phase PLL block. The output of the PR controller is the voltage reference which will be directly sent to the PWM generation unit.

3.2.5 MPPT for PV Systems

The MPPT is the major part in the photovoltaic systems which can ensure the maximum power is captured from the PV array. It continuously tunes the system regardless of weather or load conditions change such as: irradiance change, ambient temperature, or wind, which can affect the PV array output. Conventional MPPT algorithms use $\frac{dP}{dV} = 0$ to ensure the maximum power harvest.

3.2.6 Traditional IC Method

The incremental conductance technique has been implemented here which directly focuses on power variations. It means the power slope of the PV is zero at MPP ($\frac{dP}{dV} = 0$), positive on the left hand side of MPP and negative on the right. The output current and voltage of the PV panel are used to calculate the conductance and incremental conductance. The basic approach is to compare

the conductance ($\frac{I}{V}$) with the incremental conductance ($\frac{dI}{dV}$) and then decide when to increase or decrease the PV voltage. In order to reach the maximum power point, the derivative of the power ($\frac{dP}{dV}$) should be always zero. Considering $P = V.I$ [73]:

$$\frac{dP}{dV} = \frac{d(V.I)}{dV} = I + V \frac{dI}{dV} = 0 \quad (3.8)$$

$$\Rightarrow \frac{dI}{dV} = -\frac{I}{V} \quad (3.9)$$

which means when the conductance is opposite of the incremental conductance, the maximum power is guaranteed.

The discrete real-time traditional IC MPPT model is shown in Fig. 3.7. The conductance will be added to the incremental conductance to generate an error signal. The objective of the PI controller is to make the error signal zero. For real-time simulations of IC, the output of the MPPT is directly sent to the current controller loop to take advantage of the fast response of the current controller loop. Here the output of the MPPT block will be added to a constant (PV power divided by the grid voltage RMS) to form the magnitude of reference current value. This current reference will be used in the current control to adjust the grid current by means of a PR controller. A dead band controller is used. If dV becomes zero, the error will be infinity and the proposed MPPT algorithm will not work properly. The traditional dead-band controller in Fig. 3.7 shows that if dV is zero, a very small value ($1e^{-6}$) is considered to avoid the error to be infinity. The problem with traditional dead-band controller is that even when dV is set to a small value, large spikes in the output of MPPT will appear, especially when dV is oscillating around zero. This is not acceptable for the controller.

Fig. 3.8 shows a sample V-I characteristic of a PV. Assume that the operating point is at point 1 where the error is greater than zero. According to the MPPT in Fig. 3.7, the output of the PI unit will increase, which in turn decreases the AC current reference. The grid voltage is constant. In addition, the current control response is much faster than MPPT and the current is synchronized with the grid voltage through PLL. Therefore, reduction in AC current leads to the reduction in active power at the AC side. Ignoring the switching losses, the average power at the

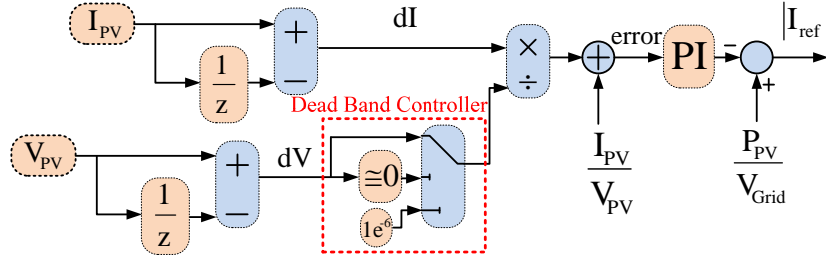


Figure 3.7. The MPPT structure for a single-phase PV in RT-Lab.

DC side should be the same of that at the AC side. Consequently, at the DC side of the converter, if we assume that the DC voltage V_{PV} is kept the same, then the DC current I_{PV} will reduce due to the reduction in the AC current magnitude. Reduction in I_{PV} will increase V_{PV} and P_{PV} (refer to P-V curve). Until the error reaches zero, the PI control will keep adjusting the AC current reference. Similarly, when the PV system is at point 3 where the error is less than zero, the AC

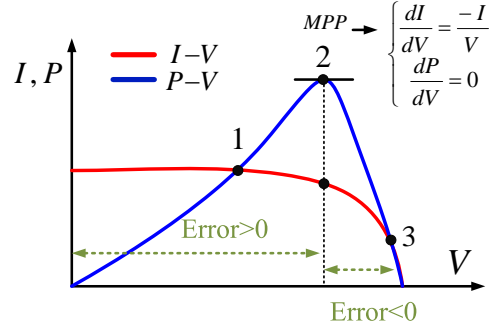


Figure 3.8. Error signal description based on I-V characteristic of PV.

current reference will increase, which in turn leads to an increase in I_{PV} and a reduction in V_{PV} . The combination leads to an increase in P_{PV} . It is possible to have oscillations in power if the gains of the PI controller are large. This can lead to an increase in the AC current reference and I_{PV} . Therefore, the error signal becomes greater than zero. The AC current reference then will reduce and this process repeats till the error approaches zero.

3.2.7 Modified IC-PI MPPT

For traditional IC-PI MPPT, when dV reaches to zero, the error signal will go to infinity and the output of the MPPT will have a spike. To solve this problem, the proposed algorithm suggests that the dV should be removed from the denominator of the error signal. Modified error signal can be considered as: $V.dI + I.dV$, which can be viewed as the previous error signal $(\frac{dI}{dV} + \frac{I}{V})$ multiplied by $V.dV$.

In this case, dV is no longer in the denominator and it will not cause any spikes in MPPT output even when dV is zero. However, the error signal should provide the same implication of operation point position as the previous error signal. Modification is presented as follows.

Analysis of the error signal used in traditional IC is presented as follows.

$$\text{If error} > 0 \left(\frac{dI}{dV} > -\frac{I}{V} \right) \Rightarrow \begin{cases} dV > 0 \Rightarrow VdI + IdV > 0 \\ dV < 0 \Rightarrow VdI - IdV < 0 \end{cases} \quad (3.10)$$

Equation (3.10) shows that if the traditional error is positive, the sign of the proposed new error will depend on the sign of dV . If dV is positive, the defined new error will be positive, same as the traditional error; but if dV is negative, the proposed new error will be negative, which is a contradiction. Same thing happens when the error is negative:

$$\text{If error} < 0 \left(\frac{dI}{dV} < -\frac{I}{V} \right) \Rightarrow \begin{cases} dV > 0 \Rightarrow VdI + IdV < 0 \\ dV < 0 \Rightarrow VdI - IdV > 0 \end{cases} \quad (3.11)$$

As a result, an effective alternative is required to ensure the modified error signal has the same implication as the traditional error signal.

The new error is now multiplied by the sign of dV . The sign of the new error will always match with the sign of the traditional error. The proposed error is very small in comparison with traditional error signal, which justifies a large gain ($K=1000$) before applying this error to a discrete PI controller. The improved MPPT algorithm is illustrated in Fig. 3.9. As it displayed in the figure, the error signal will be magnified by a gain, then the output will be sent to the PI controller.

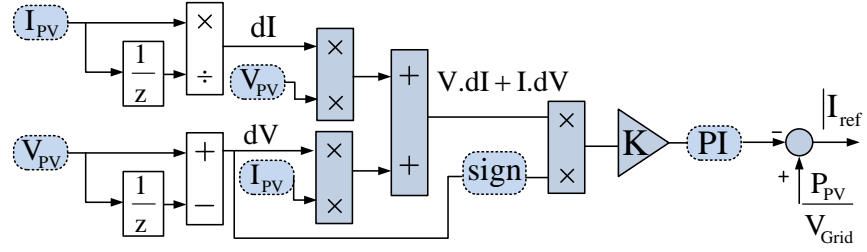


Figure 3.9. Improved IC MPPT for PV systems.

3.3 Results

3.3.1 Case Studies

This section presents the real-time simulation results, which have been conducted in real-time digital simulator RT-LAB.

A real PV model named as Sunpower SPR 305 WHT is considered to verify the proposed algorithm for IC-PI MPPT method. Parameters of the single phase PV model are listed in Table A.1 of the Appendix A. The PV model is composed of 96 cells combined in 8 series PV strings. For this type of PV panels, I_{ph} equals to 5.96 A, $R_p = 900\Omega$ and $R_s = 0.038\Omega$. The $V - I$ and $P - V$ curves for different irradiance values are illustrated in Fig. 3.10.

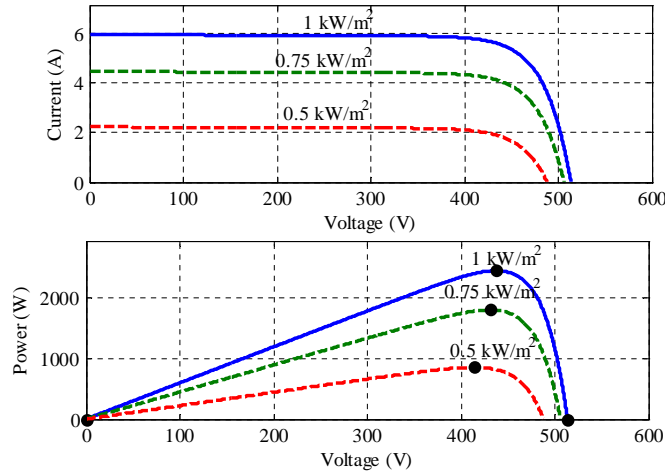


Figure 3.10. V-I and P-V curves for different irradiance values of Sunpower PV panel.

Various irradiance values will provide different $V - I$ curves. For 1 kW/m^2 , the maximum power will be around 2.45 kW when the voltage is 440 V . For the dynamic event, a step change in irradiance is applied at $t = 21 \text{ sec}$ from 1 kW/m^2 to 0.75 kW/m^2 , illustrated in Fig. 3.11. The input error for MPPT controller for both algorithms has also been shown in Fig. 3.11. It shows that the traditional method is negatively affected by high number of spikes during the simulation because the error is oscillating around zero, forcing the dead-band controller to act. In contrast, the proposed algorithm provides no spikes. The AC current magnitude reference $|I_{ref}|$ is plotted in

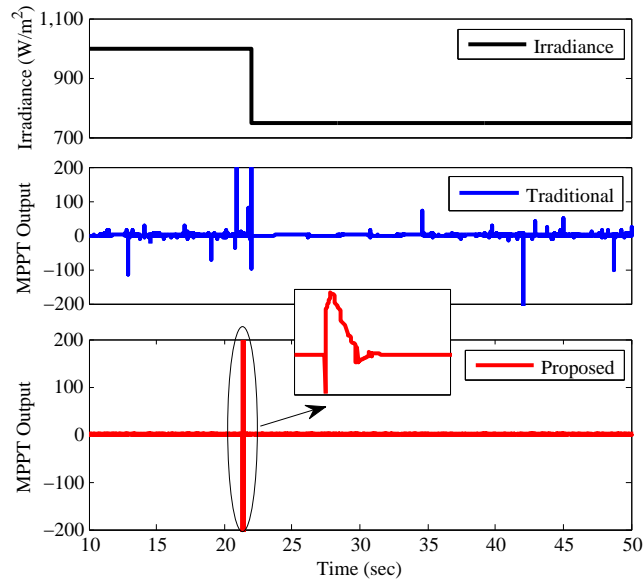


Figure 3.11. Irradiance step change and the MPPT input error.

Fig. 3.12 for both traditional MPPT and proposed MPPT. It can be observed that the proposed MPPT results in a much smoother $|I_{ref}|$.

Simulation results of the PV output power and current following the applied irradiance change are illustrated in Fig.3.13 and Fig. 3.14. After the sudden irradiance change, the traditional IC-PI method will face a lot of dynamics and it takes longer time for the active power to reach to the new steady state value. In contrast, the proposed IC method can respond to the sudden dynamic event very fast and it will track the new reference value quickly. The DC voltage is shown in Fig. 3.15. As the irradiance is changed at 21 sec , the maximum power is then set to the new value and referring to the $V - I$ characteristic presented in Fig. 3.10, the output voltage will be set to the

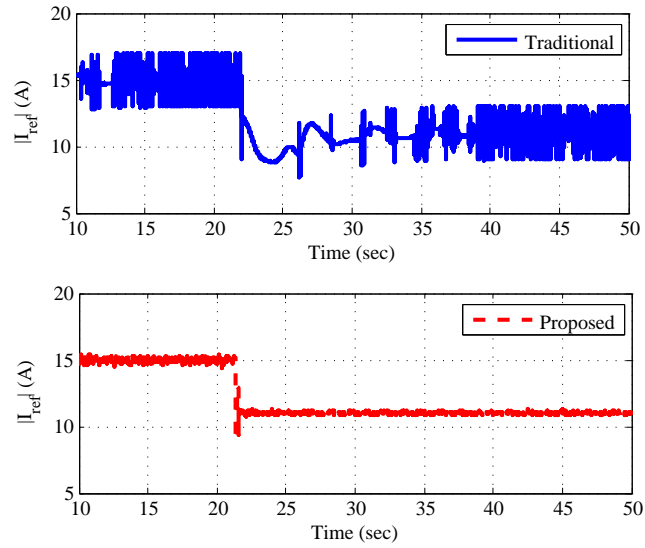


Figure 3.12. The AC current magnitude reference.

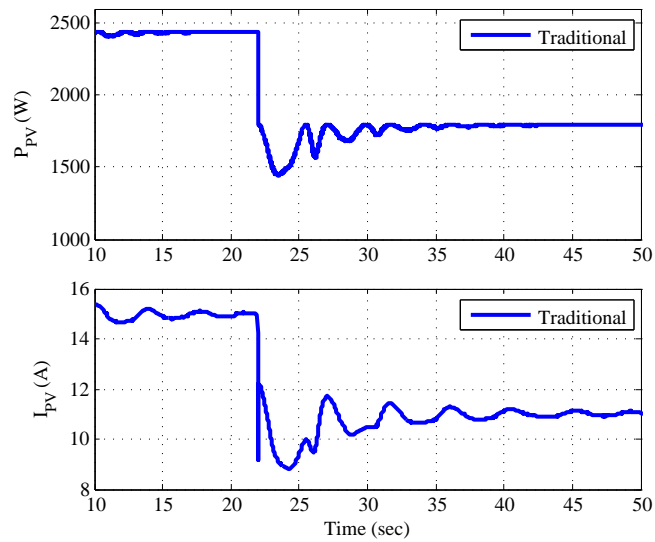


Figure 3.13. PV output power and DC current for traditional MPPT.

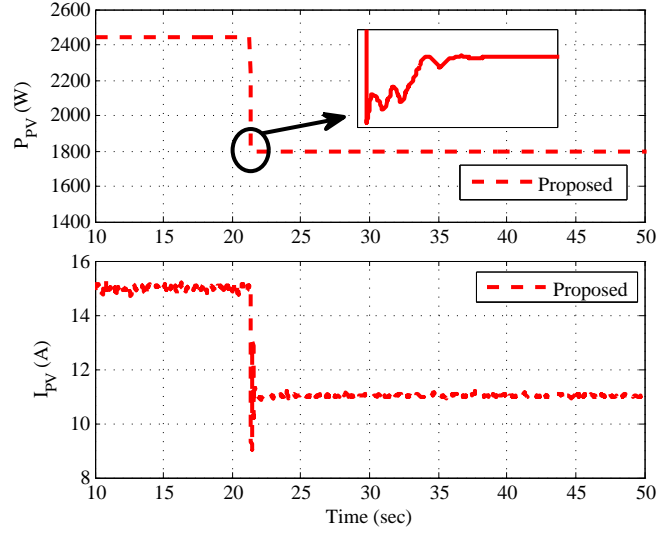


Figure 3.14. PV output power and DC current for the proposed MPPT.

new value (425 V), which is less than the previous value. Compared to the traditional method, the proposed method can fix the voltage to the new set-point very fast and without much dynamics. Results of operating point change have shown a great improvement in the MPPT algorithm. The

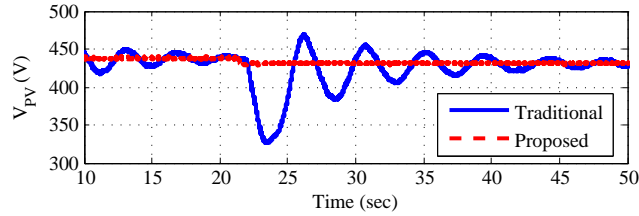


Figure 3.15. PV voltage in operating point change case.

proposed algorithm not only is easy to implement, but also provides faster response and improves the dynamic performance of the PV systems.

3.3.2 RT-LAB Performance

To examine the performance of real time simulators, the performance metrics of the model are extracted through Opmonitor Block in the RT-LAB. The Opmonitor block provides necessary information regarding the performance of the RT-LAB. It mainly records computation time, step

size, idle time, and number of overruns. Computation time is the time spent in calculation of the previous step time excluding the communication overhead in microseconds. Step size clarifies the real step size which has been selected for the model during the run, i.e. 25 microseconds in this study. Idle time refers to the idle time during the execution of previous time step. The idle time plus the computation time should be equal to the real step size. Number of overruns is the number of overruns during the run, which is zero in this case, indicating the stable condition of running. Results of the Opmonitor block are included in Fig. 3.16. In this case study, the computation time is less than 1 microsecond which verifies the CPU usage of the model is less than 4 % ($\frac{25-24}{25}100\%$). Furthermore, there is no overrun detected by the simulator which means all the cores are performing in a balanced manner.

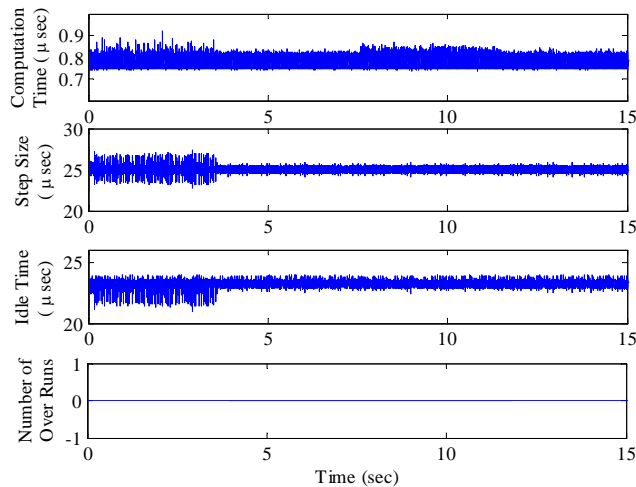


Figure 3.16. Simulation results from Opmonitor block in RT-LAB.

3.4 Discussions

This chapter presents the real-time digital simulation-based modeling of a single-phase single-stage PV grid integration system. Models for the PV panel, the PLL, the PR current control and the MPPT are all developed in a discrete domain. In addition, an improved MPPT algorithm is proposed. The proposed MPPT algorithm does not need a dead-band controller, used in traditional

IC MPPT control. Simulation case studies demonstrate that the proposed MPPT has a superior performance compared to the traditional MPPT.

CHAPTER 4

MINIMIZATION OF LOSSES IN MULTI-TERMINAL HVDC SYSTEM

This chapter ¹ investigates an adaptive droop control approach for multi-terminal HVDC system to minimize the DC loss.

4.1 Introduction

Multi-Terminal HVDC (MTDC) systems have been proposed to deliver offshore wind power [22, 23, 24, 25, 26]. The basic configuration of the MTDC system is illustrated in Fig. 4.1. The MTDC system is composed of two parts: wind farm side and grid side. At the wind farm side, a rectifier will be used to convert AC electricity to DC electricity. A DC cable is used to join the terminal to the sending end (point S). Electricity will be transferred via a DC cable to the receiving end point (point R), and finally reaches to inverter terminals. At the inverters side, electricity will be converted from DC to AC for grid connection.

The inverter controls have to be coordinated for power sharing. There are two well-known methods for inverter control coordination: master-slave control [84] and droop control [85, 26]. In the master-slave control paradigm, one inverter (master) will be controlled in constant DC voltage mode and serves as a DC voltage source. The rest of the inverters (slaves) can be controlled in power mode. Therefore, all other inverters except the master can have scheduled power outputs, while the master serves as a slack bus to absorb the rest of the power. It is required for the master inverter to have a high capacity so it can accommodate the power. The master-slave control demonstrates some reliability issues. When the master converter is lost, the entire system will be shut down.

¹This chapter was published in Electric Power Systems Research Volume 126, pp. 78-86, Sep. 2015. Permission is included in Appendix B.

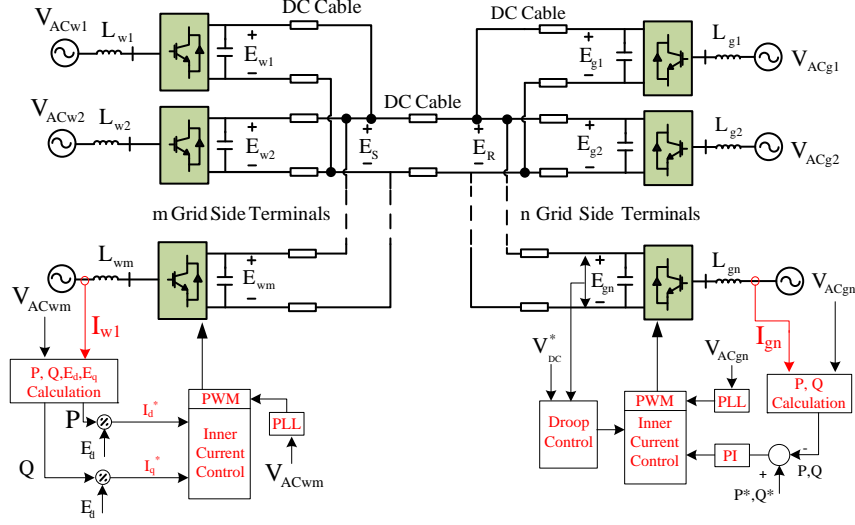


Figure 4.1. A 6-terminal MTDC schematic.

On the other hand, in droop control, inverters share power based on their droop control characteristics. If one inverter is lost, the rest of the system can still operate [85, 26]. Hence, a variety of droop schemes have been proposed for MTDC. In [86, 87], active power-DC voltage droop control is proposed. In [27], DC current-DC voltage droop control is proposed.

Appropriate design of droop control not only can facilitate power sharing among inverters, but also provides other features, *e.g.*, robust dynamic performance, post-contingency power sharing, and loss minimization. For example, in [85, 88], robust control method is adopted to design droop control for MTDC. Instead of using fixed values for droop control gains, [86] uses different droop control gains at post-contingency operating conditions so that each inverter has an adequate sharing of “headroom” (difference between the rated capacity and present loading). In [27], a methodology is proposed to minimize the copper losses in DC cables by keeping all the DC voltages at the grid side constant and selecting the droop gains proportional to the corresponding cable resistances.

Minimizing DC cable loss has been also addressed in [28]. The proposed method is to recognize each inverter’s DC side setting point through an optimization algorithm. Inverters are controlled in constant DC voltage mode. Droop control is not in the picture. The proposed “optimum voltage control” can minimize the loss, however, it cannot fulfill the power sharing.

This dissertation intends to design droop control for MTDC systems to have the function of power sharing, at the same time, to achieve minimum DC system loss. Although [89, 90] have discussed the effect of droop control in MTDC systems on the entire AC/DC system power flow, the proposed research in this paper is limited to DC systems only.

The droop control adopted in this chapter is DC current-DC voltage droop control similar as those presented in [27]. Advantage of this type of droop, compared to power-DC voltage droop used in [86, 87], is that the droop control can be considered as a Thevenin equivalent voltage source behind a resistor (where the resistance is equal to the droop gain). Plus, this type of droop control does not need to consider the impact of power-DC voltage droop on the DC system power/currents, as demonstrated in [87].

Compared to the research on droop control-based system loss minimization in the literature, *e.g.*, [27], the contributions of this chapter are listed as follows.

- 1- A comprehensive circuit analysis including the rectifier terminals, the inverter system terminals, and the effect of droop gains has been carried out. Proposed approach not only indicates that the inverter droop gains should be proportional to the corresponding cable resistances similar as the conclusion drawn in [27], but also proposes a procedure to compute the droop gains. Moreover, it is observed in the proposed design that: in order for the system to achieve minimum loss, one of the rectifier terminals should have the maximum allowed voltage level.
- 2- Droop gain computation for abnormal scenarios is proposed to keep the inverter terminal DC voltages constant.
- 3- While the research in the literature focuses on circuit analysis [27], this chapter gives circuit analysis results, along with the analytical results of detailed model based simulations. In the designed approach, converter controls and PWM dynamics have been included in the simulation model, which provides more realistic verification.

4.2 Methodology

4.2.1 Operation and Control of a MTDC System

The general structure of the MTDC system with m terminals at the rectifier side and n terminals at the inverter side is illustrated in Fig. 4.1. Each AC grid is designed as a voltage source connected to a converter through a series-connected inductor. For the DC system, each terminal is connected to a DC cable and these cables will be connected to a common coupling point. A DC cable will connect the rectifier side and the inverter side together. Detailed parameters of the system are listed as: AC voltage level: 100 kV; DC voltage level: 250 kV, $C = 350\mu\text{F}$, DC cables have the same resistance: $2.78 \times 10^{-2}\Omega/\text{km}$, DC cable lengths: rectifier1: 10km, rectifier2: 20 km, rectifier3: 30 km, inverter1: 60 km, inverter2: 50 km, inverter3: 70 km, cable SR: 100 km.

The rectifiers are controlled in the mode to transmit the generated power. The inverters are in charge of controlling their DC voltage levels, as well as reactive power to the AC systems. The voltage droop control is implemented to adjust the DC voltage reference, shown in Fig. 4.1. Both inverter and rectifier controls are generating pulses through an inner current control loop. The PWM unit for each converter aligns the output converter voltage with the AC side voltage using a PLL.

4.2.2 Rectifier Control

For the rectifier side of the MTDC, the control mode is set to $P - Q$ control in order to control the active and reactive powers of the generation unit independently. The control system for the rectifier side of the MTDC is shown in Fig. 4.2.

In Fig. 4.2, ω_s is the angular frequency of the AC system, V_{ACw1} represents the vector of the Point of Common Coupling (PCC) instantaneous abc phase voltages, E_d represents the d-axis voltage from V_{ACw1} after abc/dq conversion ($E_q = 0$ due to the alignment of the reference frame with the PCC voltage), V_a , V_b and V_c represent the converter output voltage, i_d and i_q represent the d - and q -axis currents flowing to the VSC, respectively. This control system consists of two loops: the inner current control loop and the outer power control loop.

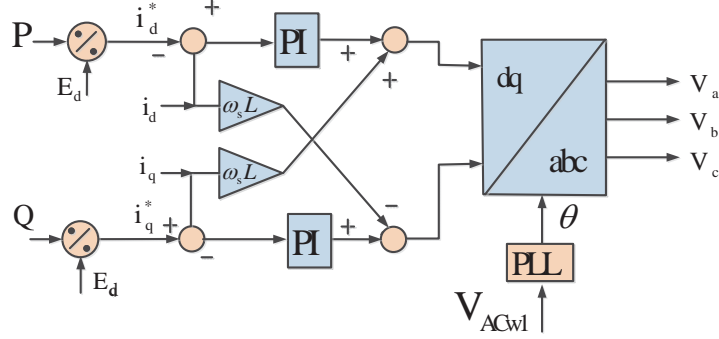


Figure 4.2. Control of wind-side converters.

4.2.3 Inverter Control

At the inverter station, the control mode is set to the DC voltage and reactive power control. The droop control is used to share the active power among the inverters. The droop control modifies the reference DC voltage at each grid-side converter. A PI controller is employed to regulate the DC voltage to follow the reference ($V_{DC}^{ref} = V_{DC0} + KI_{DC}$). The control system is shown in Fig. 4.3.

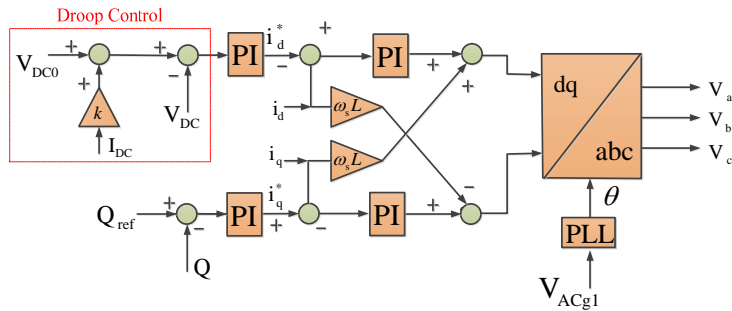


Figure 4.3. Control of grid-side converters.

4.2.4 Circuit Analysis and Optimal Setting of Droop Gains

The objective of this chapter is to set the droop gains adaptively to achieve minimum DC system loss. Circuit analysis and optimization will be carried out in this section. Firstly, the equivalent circuit of the MTDC system is derived and illustrated in Fig. 4.4(a).

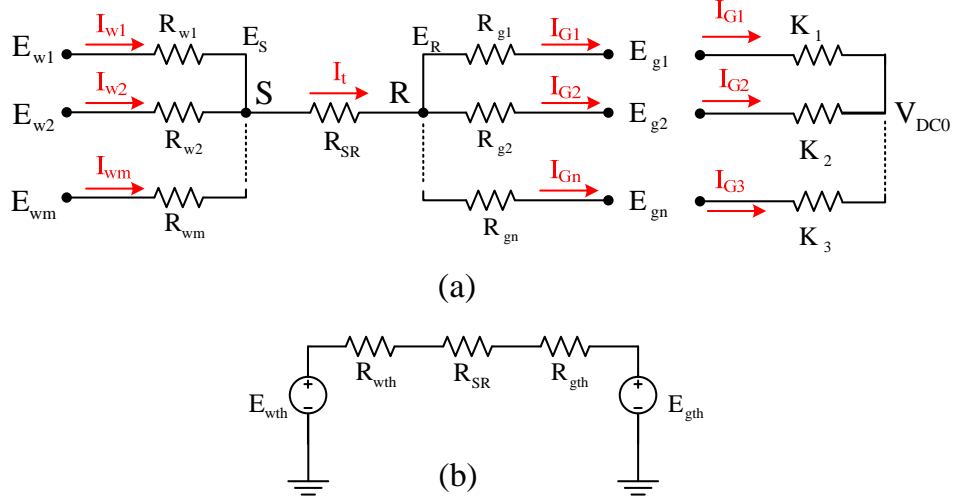


Figure 4.4. Simplified equivalent DC model for MTDC.

The dc cables are modeled as resistors. E_{w_i} and E_{g_i} represent the DC voltages of the wind farm terminals and voltages of the grid terminals, respectively. The Thevenin circuit including the droop gain effect is also illustrated in Fig. 4.4(a), where V_{DC0} is the reference DC voltage used in inverter controls.

The system can be further simplified as Fig. 4.4(b), where the Thevenin equivalent voltages and resistances are expressed as follows:

$$E_{g_{th}} = \frac{\sum_{j=1}^n \frac{E_{g_j}}{R_{g_j}}}{\sum_{j=1}^n \frac{1}{R_{g_j}}} \quad (4.1)$$

$$R_{g_{th}} = \frac{1}{\sum_{j=1}^n \frac{1}{R_{g_j}}} \quad (4.2)$$

$$E_{w_{th}} = \frac{\sum_{i=1}^m \frac{E_{w_i}}{R_{w_i}}}{\sum_{i=1}^m \frac{1}{R_{w_i}}} \quad (4.3)$$

$$R_{w_{th}} = \frac{1}{\sum_{i=1}^m \frac{1}{R_{w_i}}} \quad (4.4)$$

The DC system loss is composed of three components: the loss due to R_{w_i} , the loss due to R_{SR} , and the loss due to R_{gi} . Since the cable between S and R is the major transmission link, loss on this cable will be the major component of the total loss. Therefore, in order to have minimum DC system loss, it is desirable to have minimum I_t .

4.2.5 Rectifier Side Analysis

Given a fixed power level P_{w_i} from a converter terminal, the DC current I_{w_i} will be minimum when the DC voltage level E_{w_i} reaches its maximum. Since the voltage at the joint point S ($E_s = E_{w_i} - R_{w_i} \frac{P_{w_i}}{E_{w_i}}$) depends on each terminal voltage E_{w_i} , if more than one terminal voltages are scheduled, there will be conflicts for E_s . Consequently, only one terminal will operate at the maximum voltage level.

An iterative method is performed to search for the rectifier terminal that should be on the maximum level at each operating point. After identifying that terminal, a step by step procedure is applied to find the desired I_t . The procedure is listed:

- Active power at each rectifier terminal is given (P_{w_i} for $i = 1, 2, \dots, m$).
- After finding one rectifier that should work on its maximum voltage (E_{w_k} is assumed), the converter's DC current is derived by: $I_{w_k} = \frac{P_{w_k}}{E_{w_k}}$.
- The sending end voltage is then derived by:

$$E_s = E_{w_k} - R_{w_k} I_{w_k} \quad (4.5)$$

- I_t is computed by the following equations:

Since $E_{w_i} = E_S + R_{w_i} \frac{P_{w_i}}{E_{w_i}}$, we can determine an expression for I_{w_i} in terms of P_{w_i} and E_S as:

$$I_{w_i} = \frac{-E_S + \sqrt{E_S^2 + 4R_{w_i}P_{w_i}}}{2R_{w_i}}. \quad (4.6)$$

Therefore,

$$I_t = \sum_{i=1}^m I_{w_i} = \sum_{i=1}^m \left(\frac{-E_S + \sqrt{E_S^2 + 4R_{w_i}P_{w_i}}}{2R_{w_i}} \right) \quad (4.7)$$

- The receiving end voltage E_R , as well as the Thevenin equivalent terminal voltage E_{gth} can also be obtained.

The rectifier side analysis gives the desired total current I_t , the desired rectifier side terminal voltages E_{w_i} , the desired E_S , the desired E_R , and the desired E_{gth} .

Note that the converter controls of the rectifiers only determine the scheduled power level P_{w_i} . Thus, the rectifier controls alone cannot recognize the steady-state DC currents and voltage levels. It is left to the inverter controls, specifically droop gains, to identify the steady-state DC currents and voltage levels.

4.2.6 Inverter Side Analysis

Given the desired I_t , the next task is to allocate current to each inverter to have minimum loss on the cables connecting the inverters. The loss related to the inverter-side cables can be written as:

$$P_{loss_g} = \sum_{j=1}^n R_{g_j} I_{g_j}^2. \quad (4.8)$$

Further modification will lead to:

$$P_{loss_g} = \sum_{j=1}^{n-1} R_{g_j} I_{g_j}^2 + R_{g_n} \left(I_t - \sum_{k=1}^{n-1} I_{g_k} \right)^2. \quad (4.9)$$

In order to define the optimal solution of current allocation $I_{g_j}^*$, the partial derivative of losses versus any I_{g_j} evaluated at $I_{g_j}^*$ should be zero.

$$\begin{aligned} \left. \frac{\partial P_{loss_g}}{\partial I_{g_j}} \right|_{I_{g_j}^*} &= 2R_{g_j}I_{g_j}^* - 2R_{g_n} \left(I_t - \sum_{k=1}^{n-1} I_{g_k}^* \right) = 0 \\ \Rightarrow R_{g_j}I_{g_j}^* &= R_{g_n} \left(I_t - \sum_{k=1}^{n-1} I_{g_k}^* \right) \quad \text{for all } j = 1, \dots, n-1 \end{aligned} \quad (4.10)$$

Combining $I_t = \sum_{i=1}^m I_{w_i} = \sum_{j=1}^n I_{g_j}$ and the $n-1$ equations of (4.10) results in the following finding:

$$R_{g_j}I_{g_j}^* = R_{g_n}I_{g_n}^* \quad (4.11)$$

$$E_{g_j}^* = E_{g_n}^* = E_{g_{th}} \quad \text{for all } j = 1, \dots, n. \quad (4.12)$$

It proves that to minimize the losses at the inverter side, the terminal voltage of the converters should be equal. This finding has also been documented in [27].

The finding indicates that the active power sharing among inverters is proportional to the current sharing:

$$\frac{P_{gj}}{P_{gk}} = \frac{E_{gj} \cdot I_{gj}}{E_{gk} \cdot I_{gk}} = \frac{I_{gj}}{I_{gk}} \quad (4.13)$$

In addition, based on the voltage/current relationship for the circuit in Fig. 4.4(a) ($E_{g_j} = V_{DC0} + K_j I_{g_j}$ and $E_{g_j} = E_R - I_{g_j} R_{g_j}$), the currents are inversely proportional to the droop gains and the cable resistances.

$$\frac{P_{gj}}{P_{gk}} = \frac{I_{gj}}{I_{gk}} = \frac{R_{gk}}{R_{gj}} = \frac{K_k}{K_j} \quad (4.14)$$

The important conclusion derived from the above analysis is that the droop gains should be selected in proportional to the cable resistances ($K_j \propto R_j$).

The droop gain K_j can be calculated by further analysis. Since the droop gains are correlated to the cable resistances, the current sharing among inverters will be inversely proportional to the cable resistance at each branch. Therefore,

$$I_{g_j} = \frac{\frac{1}{R_{g_j}}}{\sum_{k=1}^n \frac{1}{R_{g_k}}} I_t \quad (4.15)$$

The droop gains can be computed based on $E_{g_j} = E_{g_{th}}$ and I_{g_j} .

$$K_j = \frac{E_{g_j} - V_{DC0}}{I_{g_j}} \quad (4.16)$$

The proposed algorithm for droop gain calculation works for any operating point. It can ensure the minimum total current (I_t) from the rectifier side analysis. It is noted that, when the power level P_{w_i} changes, the droop gains should be recalculated. This is due to the fact that I_t varies with P_{w_i} and the droop gain depends on I_t . Furthermore, when the system topology changes, *e.g.*, a grid-side converter is lost, the droop gains should be recalculated. In the following subsection, the droop gains will be updated when one of the grid-side converters is lost.

4.2.7 Analysis of an Abnormal System

To conduct the analysis, we assume that one inverter is lost. The power levels are intact. The desired total current I_t and the desired grid terminal voltage $E_{g_{th}} = E_{g_j}$ will be the same. What is changed is the current allocation to each inverter.

$$I_{g_1} = \frac{\frac{1}{R_{g_1}}}{\frac{1}{R_{g_1}} + \frac{1}{R_{g_2}}} I_t \quad (4.17)$$

$$I_{g_2} = \frac{\frac{1}{R_{g_2}}}{\frac{1}{R_{g_1}} + \frac{1}{R_{g_2}}} I_t \quad (4.18)$$

The droop gains will be found from the following equations.

$$K_1 = \frac{E_{g1} - V_{DC0}}{I_{g1}} \quad (4.19)$$

$$K_2 = \frac{E_{g2} - V_{DC0}}{I_{g2}} \quad (4.20)$$

4.3 Results

4.3.1 Case Studies

The study system is constructed in RT-LAB, a real-time digital simulator manufactured by OPAL-RT, which can simulate the power system model with detailed power electronic switches in real-time [91]. As a result, it can provide precise simulation results and take the switching details of IGBTs into the account.

The test system is a 6-terminal MTDC system composed of three rectifier side terminals and three inverter side terminals as shown in Fig. 4.1. The base voltage is set to 250 kV and the base power is set to 100 MW. Fixed generated power is considered at each rectifier side, set to 100, 90, and 110 MW, respectively. Parameters of the system are listed in Table A.2 and Table A.3 of Appendix A.

The maximum voltages for converters are 260 kV and maximum current settings of the converters are set to 1 kA. The optimal droop gains are computed and listed in Table 4.1. The terminal voltages and currents are also listed. The DC voltage setting in the inverter control V_{DC0} is 240 kV.

Table 4.1. Droop gains at the base case

Converter	Inverter Side			Rectifier Side		
	Droop	$R_g(\Omega)$	E_g (kV)	I_g (A)	E_w (kV)	I_w (A)
1	41.89	1.69	255	375	260	380
2	35	1.39	255	447	260	342
3	48.82	1.95	255	320	260	420

It is observed that at the inverter side, all the inverters are working at the same voltage of 255 kV. The total current flowing in the major DC cable SR (I_t) is 1142 A. Besides, at the wind farm side, as the maximum voltage for all the converters are the same, all of them are operating at their

maximum. This will assure the maximum power transmission through MTDC system, as well as minimum loss condition.

4.3.2 One of the Inverter Side Terminals Is Tripped

In this case study, we investigate the effect of adaptive droop gains when one inverter is tripped. Two cases are included here:

- Case 1: the droop gains will not be updated after the trip.
- Case 2: the droop gains will be updated using proposed algorithm.

In case 1, the droop gains are obtained from the proposed algorithm as $K_1 = 41.89$, $K_2 = 35$, and $K_3 = 48.82$ for the nominal operating condition. Further, the gains are fixed. The steady-state voltages and currents after an inverter is tripped are listed in Table 4.2. The circuit calculation displays that the DC voltages all rise up. Dynamic simulation results will be presented following the circuit analysis results.

Table 4.2. Droop gains, voltages and currents for case 1 in line trip event

Converter	Inverter Side			Rectifier Side		
	Droop	$R_g(\Omega)$	E_g (kV)	I_g (A)	E_w (kV)	I_w (A)
1	41.89	1.69	261	510	265	375
2	35	1.39	261	614	265	337
3	48.82	1.95	261	0	265	412

Results of the voltages at rectifier and inverter side are shown in Fig. 4.5. After the fault at 5 sec, the voltages at both sides will rise. The maximum voltage for the rectifier side before the fault is set to 260 kV. After the fault, the voltage levels reached 265 kV. This 5 kV increase in the voltage will cause damage to converters.

Results of the rectifier side and inverter side currents for case 1 are illustrated in Fig. 4.6. As demonstrated, the current for the third terminal eventually reaches zero. Oscillations around zero are observed during the transients. The oscillations are absorbed by the DC-link capacitors.

In case 2, the proposed algorithm will update the droop gains at each operating point in order to guarantee the minimum loss within the system. In the normal operation, the proposed algorithm will result in optimized steady state droop gains as: $K_1 = 41.89$, $K_2 = 35$, and $K_3 = 48.82$. After 5

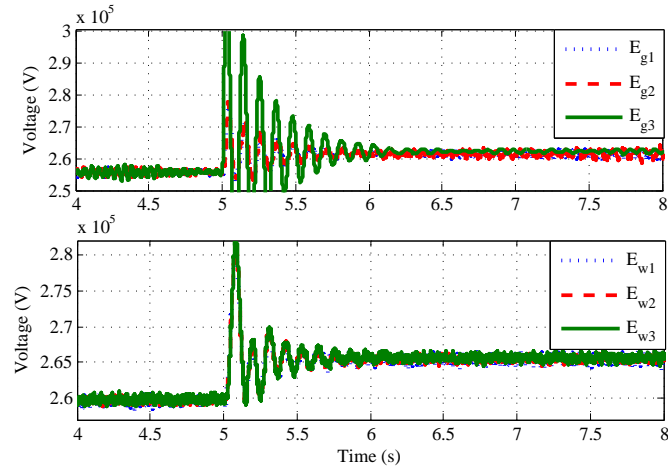


Figure 4.5. Voltages at grid side and wind farm side terminals for case 1 in line trip event.

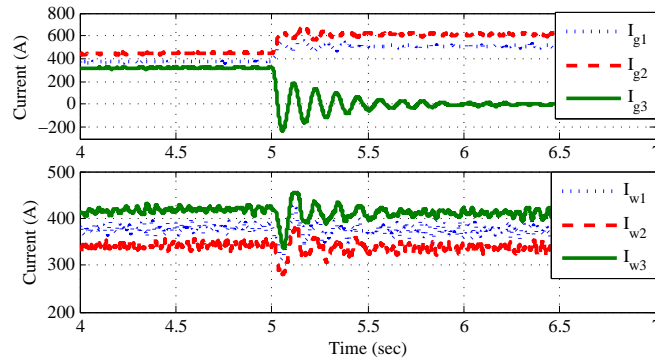


Figure 4.6. Currents at grid side and wind farm side terminals for case 1 in line trip event.

seconds, the contingency is considered as a three-phase line trip in the third inverter side terminal. The droop gains are recomputed and listed in Table 4.3.

Table 4.3. Droop gains, voltages and currents for case 2 in line trip event

Converter	Droop	Inverter Side			Rectifier Side	
		$R_g(\Omega)$	E_g (kV)	I_g (A)	E_w (kV)	I_w (A)
1	29.7	1.69	255	517	260	380
2	24.7	1.39	255	620	260	340
3	-	1.95	255	0	260	417

Change of droop gains is illustrated in Fig. 4.7. After the fault, the third terminal is out and its droop gain is shown as zero.

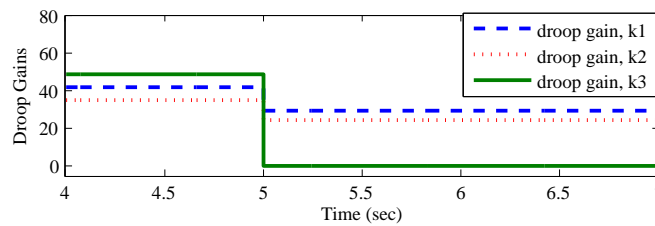


Figure 4.7. Droop gain change of grid side terminals for case 2 in line trip event.

Simulation results of the terminal voltages at the inverter side and rectifier side are illustrated in Fig. 4.8. Simulation results for the currents are shown in Fig. 4.9. It can be observed that after the fault at 5 sec, the rectifier side and inverter side voltages remain the same as they were before the fault. As the rectifier side converters are working at their maximum voltage limit, the rectifier side is guaranteed to work on minimum loss. Moreover, at the inverter side, all the terminal voltages are equal, which ensures the minimum losses in the inverter side. The other important result is that the DC voltages did not rise up after the fault. It shows that the proposed algorithm not only ensures the minimum losses in the MTDC system, but also ensures constant DC voltage level.

4.3.3 Change of Active Power Generated by Wind Farms

In this case study, we examine the effect of active power change on droop gain calculation and system performance. Generated power in one rectifier side terminal is increased from 90 MW to 120 MW at 5 seconds. The other two terminal powers are kept the same (100 and 110 MW). Two cases are compared.

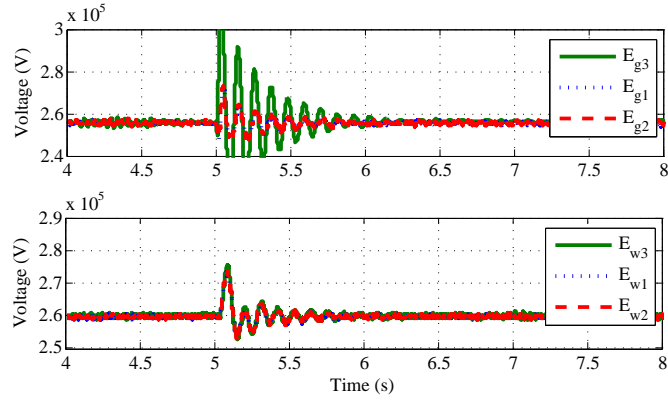


Figure 4.8. Voltages at grid side and wind farm side terminals for case 2 in line trip event.

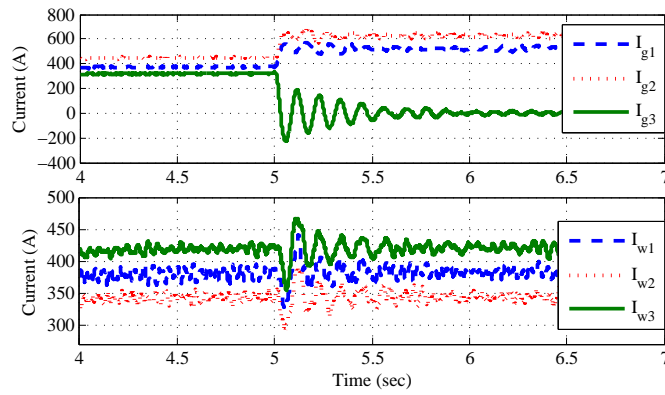


Figure 4.9. Currents at grid side and wind farm side terminals under optimized operation.

- Case 1: the droop gains will not be updated after the power change.
- Case 2: the droop gains will be updated by proposed algorithm.

The droop gains, DC voltages and currents at steady-state for case 1 are listed in Table 4.4. It can be seen that the wind side terminals will have over voltages.

Table 4.4. Droop gains, voltages and currents for case 1 in active power change

Converter	Droop	Inverter Side			Rectifier Side	
		$R_g(\Omega)$	E_g (kV)	I_g (A)	E_w (kV)	I_w (A)
1	41.89	1.69	257	400	262	380
2	35	1.39	257	483	262	428
3	48.82	1.95	257	345	262	420

Fig. 4.10 shows the terminal voltages of rectifier side and inverter side when fixed droop gains are used. The optimal droop gains are applied in this case, same as previous cases ($K_1 = 41.89$, $K_2 = 35$, and $K_3 = 48.82$). After the change in power, the droop gains will stay the same. As it appears, both terminal voltages will rise up after the operating point change.

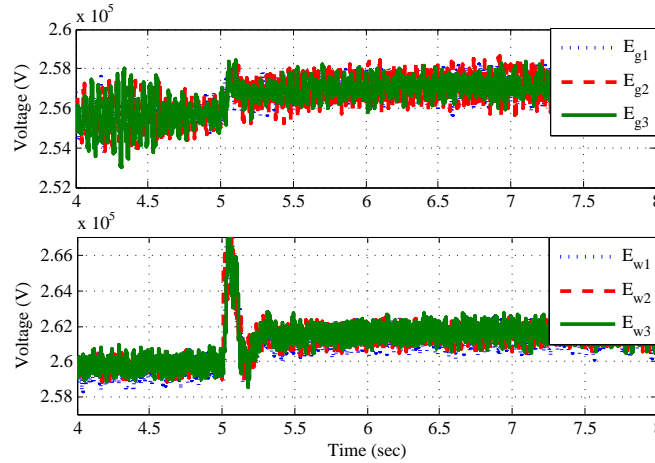


Figure 4.10. Voltages at grid side and wind farm side terminals for fixed droop gains in active power change.

In case 2, the droop gains are recomputed for the updated power level. The results are listed in Table 4.5. It can be observed that the steady-state DC voltage levels are kept the same as the base case. Simulation studies for the optimized case where droop gains are updated are also carried out. The simulation results are illustrated in Fig. 4.11, show that even with power change at one terminal, the proposed adaptive droop strategy fixes the voltages of the inverter and rectifier side.

Table 4.5. Droop gains, voltages and currents at steady-state for case 2 in active power change

Converter	Droop	Inverter Side			Rectifier Side	
		$R_g(\Omega)$	E_g (kV)	I_g (A)	E_w (kV)	I_w (A)
1	37.1	1.69	255	413	260	385
2	30.9	1.39	255	493	260	457
3	43.3	1.95	255	356	260	420

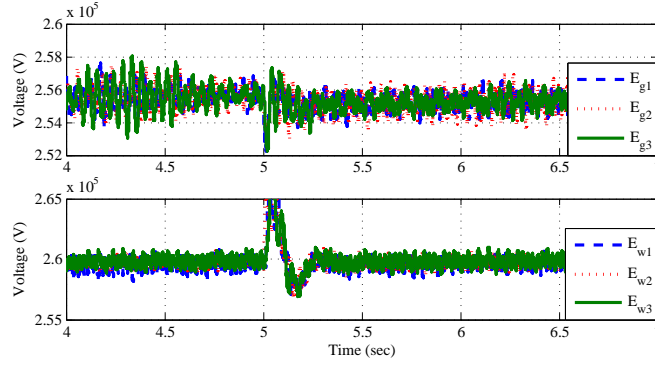


Figure 4.11. Voltages at grid side and wind farm side terminals for adaptive droop gains in active power change.

4.4 Discussions

This chapter proposes a droop control-based DC system loss minimization strategy. Through setting droop gains for grid-side converters, the MTDC system can achieve minimum DC loss and constant DC voltage level for any operating conditions. The change in operating conditions can be an increase in power transfer or loss of a grid-side converter. The proposed droop gain computation algorithm has two notable features: (i) droop gains are proportional to the cable resistances; (ii) one of the wind farm terminals will work at maximum voltage level. Real-time digital simulation-based tests are carried out to demonstrate the proposed adaptive droop control performance in keeping the DC voltage level and minimizing DC loss in various operating conditions.

CHAPTER 5

DISTRIBUTED CONTROL FOR ENERGY STORAGE SYSTEM

Distributed coordination or decentralized control is a recently proposed topic in power systems. It was originally applied to the secondary controllers to restore frequency and voltage of converters in a distributed manner. The idea in this chapter is to use the distributed coordination control to synchronize the energy storage devices in a microgrid. To design a unified controller with limited information exchange, consensus theory is applied.

5.1 Introduction

Microgrid technology provides an effective solution to integrate renewable energy sources, loads, and energy storage systems. This chapter focuses on coordination of batteries to synchronize the state of the charge (SOC) and power level via distributed control. This introduction covers the justification of the distributed coordinated control instead of centralized coordination, consensus control philosophy, and significance of this research over the existing research.

One of the most significant concerns related to the renewable energy sources in microgrids is their limited operating times due to the uncertain behavior. For example, PV modules can only generate electricity in presence of sun irradiance [29, 30], or wind farms can only operate in places where the sufficient amount of wind exists [31]. Therefore, battery energy storage systems are commonly implemented as the energy buffers [32, 33, 34]. Recent studies have implemented energy storage in the microgrid to cooperate with the renewable energy sources. For example, [33] studies the smoothing performance of PV and wind generation in presence of battery energy storage systems as a hybrid microgrid. Similarly, [35] reviews the challenges of integrating the energy storage in distribution power systems, and describes different control methodologies implemented for energy storage systems.

Although the battery energy storage system can facilitate the operation of renewable energy sources in microgrids, its function is not limited to a single task. Similar as traditional power systems, a hierarchical control has been designed in microgrids. The hierarchical control of energy storage system is a recently proposed topic that enables the energy storage system with multi-task operation capabilities [92, 93].

Hierarchical control proposes three various control levels known as: primary, secondary, and tertiary. Droop control is the most common approach in primary frequency controllers for batteries in an autonomous microgrid [94, 95]. Since droop parameters determine load sharing among batteries, droop control gains can be associated with the SOC of batteries [96, 97, 98]. This approach can push the batteries with high SOC to share more, whereas batteries with lower SOC share less. In the secondary frequency control, a control center measures frequency and tie-line power deviations and sends the Area Control Error (ACE) signal into an integral control. Furthermore, the output is sent out to each converter. In the tertiary control, a control center calibrates the power level of each converter and sends the power commands to each converter to change the power order. Traditionally, secondary and tertiary controllers were centralized controllers.

Why distributed control? Centralized controllers need communication network in order to send the control command to the entire network. A centralized controller manages a large amount of data, which is vulnerable to a single point of failure. Advanced distributed control structures are recently proposed to increase the reliability of hierarchical control systems in microgrids. The main purpose of the distributed cooperative control is to achieve a general agreement among all of the control agents with a limited data transfer. In addition, if either of the communication or the physical system fails, the whole system will not be shut down and thus it only will affect the faulted elements.

Distributed control has been proposed for the secondary control in microgrids [36, 37, 38, 39]. For example, [37] proposes the feedback linearization based consensus control design for inverters in islanded microgrids. The authors used the consensus input to synchronize the inverter voltages. Furthermore, [38] proposes the consensus based distributed control for synchronizing the active and reactive power sharing in different droop control methodologies applied in microgrids. Consensus

control has also been applied in battery converters to achieve the consensus for the SOC and power levels [41].

Consensus SOC and power level are often desirable among energy storage systems and provide the energy storage with higher efficiency and State of Health (SOH). If the SOC and the power of energy storage systems are consensus, during the operating point or load change, no single energy storage tends to go beyond the permitted threshold. Accordingly, the power capacity of the energy storage is maximized during the operation.

There are a few papers investigated the SOC balancing with various algorithms [99, 100, 101]. For example, [99] has introduced a consensus input that will directly modify the energy storage power to accomplish the consensus state of charge. However, this design will finally reduce the reference powers of the energy storage devices down to zero, as the consensus input will be zero when the synchronization is achieved. Furthermore, [101] introduces a multi-agent based synchronization algorithm for SOC balancing in energy storage devices with frequency scheduling instead of droop control. The average SOC of each energy storage is calculated through a consensus method and each energy storage is commanded to follow the obtained average. This design is also not thorough, since it needs the SOC for all the energy storage units, while does not provide the limited information transfer. Among all of the mentioned references, general assumption is that the energy storage devices are working in one operating mode (islanded mode) and if the operating mode changes, the design needs to be revised as well. This research mostly focuses on synchronizing the energy storage power and SOC with limited information exchange. Plus, a generalized controller will be designed, which works for both operating modes of a microgrid without any modifications.

The objective of this chapter is to synchronize the SOC and power level for energy storage devices in a microgrid. This topic was studied in [41] based on the following assumptions; (i) Each battery has exactly the same control architecture and control parameters. (ii) All the states including the SOC, the power, the current and the voltage of a battery will reach consensus. These two assumptions are very restrictive. Batteries may have different control architectures and parameters. There is also no need to achieve consensus for all states (including currents and voltages). The consensus design in [41] is based on a very complicated model for a specific control

architecture and specific operation mode. Such design cannot be applicable if the operation mode of a microgrid is changed from autonomous to grid-connected. The data exchange is also required for all the states of neighboring agent which is not favorable.

The designed approach in this dissertation follows a simple second-order analytic model including battery SOC and power as the control input. The outcome of the design is a simple distributed control architecture with only SOC and power as the exchanging information among agents. This control design is applicable in any operating modes: autonomous or grid-connected.

The assumption of the design is that the power order of a battery is generated by an integral controller. Compared to consensus control, dynamics of the power controller are very fast. In the consensus design step, a double integrator model is considered. The function of the consensus control is to adjust power orders of the batteries to achieve SOC/power consensus, while keeping the total power from the batteries constant. In that sense, consensus control alone cannot bring system frequency back to nominal. Therefore, similar as the ACE signal, this consensus input signal is combined with frequency deviation to be sent to the integrator to generate power order for each battery converter. This design combines the consensus control with the secondary frequency control.

When the system has a load change, the designed control can bring the system frequency back to nominal and keep the battery SOC/power consensus. The designed approach is validated by simulation of a complicated microgrid model built in RT-LAB.

5.2 Methodology

5.2.1 Distributed Control Design Philosophy

The objective of this problem is to synchronize the battery SOC and power. The foremost assumption is that the power order of a battery is generated through an integrator. Further, each converter has an integrator. Secondary frequency control uses integrator, which can also be used for consensus power and energy.

Consensus control will be designed to be much slower than frequency control. Hence, when there is a load change, frequency control quickly increases or decrease the total power to match the

load. Afterwards, consensus control adjusts the power among the batteries, while keeping the total power constant.

5.2.2 System Model and Communication Graph

A simplified three-battery system model is given as follows assuming that the dynamics from the power order to power measurement is negligible.

$$\begin{cases} \dot{E}_1 = -\frac{P_1}{3600} \\ \dot{P}_1 = u_1 \\ \dot{E}_2 = -\frac{P_2}{3600} \\ \dot{P}_2 = u_2 \\ \dot{E}_3 = -\frac{P_3}{3600} \\ \dot{P}_3 = u_3 \end{cases} \quad (5.1)$$

where E and P are the per unitized energy and power. Since batteries use kWh and kW as the units for energy and power, a $1/3600$ coefficient is applied in the time scale of seconds. A battery's per unit energy is the same as its SOC if the energy base is the same as the battery capacity.

Now look at the communication graph of this system as shown in Fig. 5.1. This graph can be represented by a Laplacian matrix L .

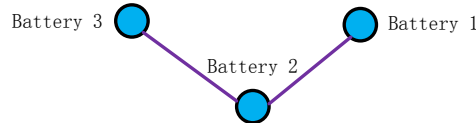


Figure 5.1. Communication graph of the proposed system.

$$L = \begin{bmatrix} 1 & -1 & 0 \\ -1 & 2 & 1 \\ 0 & -1 & 1 \end{bmatrix} = \underbrace{\begin{bmatrix} 1 & 0 & 0 \\ 0 & 2 & 0 \\ 0 & 0 & 1 \end{bmatrix}}_D - \underbrace{\begin{bmatrix} 0 & 1 & 0 \\ 1 & 0 & 1 \\ 0 & 1 & 0 \end{bmatrix}}_A \quad (5.2)$$

where $L_{ij} = -a_{ij}, i \neq j$ and i . $a_{ij} > 0$, when i is connected with j and $a_{ij} = 0$ when i is not connected to j . $L_{ii} = \sum_j a_{ij}$. D is a diagonal matrix with diagonal elements representing the degree of each node. A is a non-negative matrix with zero diagonal components.

The Laplacian matrix L has a trivial eigenvalue 0 with the corresponding right eigenvector of $\mathbf{1}$, a column vector with every element as 1.

$$L\mathbf{1} = 0 \tag{5.3}$$

For the balanced graphs like the one in Fig. 5.1, L is a symmetric matrix, therefore,

$$\mathbf{1}^T L = (L\mathbf{1})^T = 0 \tag{5.4}$$

5.2.3 Design of the Inputs

To facilitate the design process, it is assumed that the battery energy storage can track the reference power fast and accurate. Moreover, in islanded mode operation, it is assumed that the frequency controllers can quickly restore the frequency to its nominal value. As a result, the dynamics of the inner loops, the secondary frequency control, and the power controllers are neglected in this case. This will simplify the design without neglecting the controller dynamics. The battery energy can be written in terms of battery power too.

Therefore, dynamics of each battery energy storage can be written as:

$$\underbrace{\begin{bmatrix} \dot{E}_i \\ \dot{P}_i \end{bmatrix}}_{x_i} = \underbrace{\begin{bmatrix} 0 & -1/3600 \\ 0 & 0 \end{bmatrix}}_A \underbrace{\begin{bmatrix} E_i \\ P_i \end{bmatrix}}_{x_i} + \underbrace{\begin{bmatrix} 0 \\ 1 \end{bmatrix}}_B u_i \tag{5.5}$$

where A and B are state matrices of the system. Now, u_i can be designed in order to synchronize the energy and power levels of energy storage based on consensus objective.

For linear interconnected systems, consensus control design can be based on Lyapunov design, or optimal control design [102]. In this chapter, optimal control design [103] is adopted. The

dynamic model of each energy storage is represented as a state space model ($\dot{x} = Ax + Bu$). The final goal of synchronization can be obtained if the difference between the power and energy of the energy storage and the power and energy of its neighbours is sent to each battery energy storage as an input of the controller. It is also noted that the $x = [x_1, x_2, \dots, x_n]^T$ is a global vector of state variables, and $u = [u_1, u_2, \dots, u_n]^T$ is the global vector of inputs in the systems. The control input is designed as:

$$u_i = cK \sum_{j=1}^n a_{ij}(x_j - x_i) = cK \sum_{j=1}^n a_{ij} \begin{bmatrix} E_j - E_i \\ P_j - P_i \end{bmatrix} \quad (5.6)$$

where a_{ij} is the element of the matrix A in (5.2), c is a positive scalar gain and K is the variable for the feedback control matrix.

The vector of all the inputs can be expressed as

$$u = cL \begin{bmatrix} Kx_1 \\ \vdots \\ Kx_n \end{bmatrix} \quad (5.7)$$

Therefore,

$$\sum_i u_i = \mathbf{1}^T u = c\mathbf{1}^T L \begin{bmatrix} Kx_1 \\ \vdots \\ Kx_n \end{bmatrix} = 0 \quad (5.8)$$

This is an important characteristic of consensus control. The summation of the inputs are always 0. This also means that the summation of the power orders of all batteries should be constant. The role of the consensus control is to adjust the power generated by each battery, while keeping the total power constant. This function can be combined with secondary frequency control so that when there is a load change, the secondary frequency control will take care of the load change and modify the power orders of each battery.

K can be found using Linear Quadratic Regulator (LQR) design. Given two matrices Q and R are positive definite, the feedback gain K in (5.6) can be designed as:

$$K = R^{-1}B^T P_1 \quad (5.9)$$

where P_1 is the unique positive definite solution of the control algebraic Riccati equation (ARE) [37]:

$$A^T P_1 + P_1 A + Q - P_1 B R^{-1} B^T P_1 = 0 \quad (5.10)$$

5.2.4 Stability Analysis

The closed-loop system dynamics should be considered for analyzing the stability of the designed method. Adding the designed control input (5.6) into the state-space model of each agent leads us to (5.11).

$$\dot{x}_i = Ax_i + cBK \sum_{j=1}^n a_{ij}(x_j - x_i) \quad (5.11)$$

The overall global closed-loop system can be represented as (5.12):

$$\dot{x} = (I_n \otimes A)x - cL \otimes BKx \quad (5.12)$$

The stability criteria for the interconnected system that combines the control design requirements with the graph properties is given in [103]. If the eigenvalues of the Laplacian graph matrix L are denoted as λ_i , the stability properties of the global system dynamics in the equation (5.12) are equivalent to the stability properties of:

$$\dot{z}_i = (A - \lambda_i cBK)z_i \quad i = 1, 2, \dots, n \quad (5.13)$$

The stability criteria requires $(A - \lambda_i c B K)$ to be Hurwitz, or all of its eigenvalues have a strictly negative real part. A sufficient condition requires c to be selected as:

$$c = \max \left(\frac{1}{2 \min \operatorname{Re}(\lambda_i)}, 1 \right) \quad i = 2, \dots, n \quad (5.14)$$

5.2.5 Numerical Example

For a system with three energy storage units, solving for the Riccati equation in (5.10) provides matrix P if R and Q are given. The control input K can be selected referring to the equation (5.9) as $K = [K_1 \quad K_2]$ and c can be selected as equation (5.14) to be 1. The designed controller will be the input of the battery energy storage in order to synchronize the energy levels. Considering the communication graph of the system shown in Fig. 5.1, three inputs can be selected as:

$$\begin{aligned} u_1 &= -c[K_1 \quad K_2] \begin{bmatrix} E_1 - E_2 \\ P_1 - P_2 \end{bmatrix} \\ u_2 &= -c[K_1 \quad K_2] \begin{bmatrix} 2E_2 - E_1 - E_3 \\ 2P_2 - P_1 - P_3 \end{bmatrix} \\ u_3 &= -c[K_1 \quad K_2] \begin{bmatrix} E_3 - E_2 \\ P_3 - P_2 \end{bmatrix} \end{aligned} \quad (5.15)$$

Fig. 5.2 illustrated the communication block diagram for the system shown in Fig. 5.1 with simplified dynamic models of the batteries presented in (5.5) and consensus control inputs presented in (5.15). The combined system can provide a clear idea about how the proposed algorithm can synchronize the energy levels of each battery energy storage unit. It is also noted that the simplified models can be used for eigenvalue analysis and stability analysis where the complicated network communication graph is existed.

Fig. 5.3 shows a sample design by choosing a set of Q and R . The resulting system dynamics show that battery 1's power may increase 50% due to its high SOC. Battery 3's power is reduced

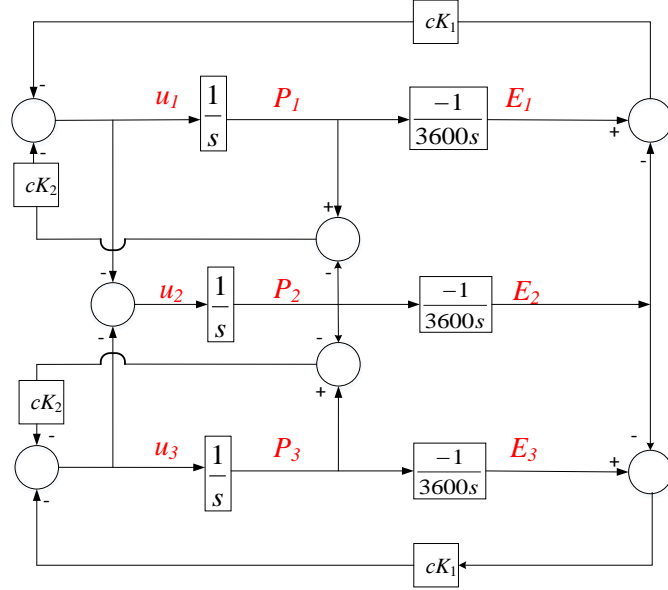


Figure 5.2. Block diagram of the simplified battery models including consensus based SOC management control.

to almost zero. In real-world scenarios, battery's power is limited. It is also not desirable to have batteries operating in different modes, with some charging and some discharging. Therefore, a less dramatic change is expected. Fig. 5.4 shows a different set of parameters which leads to a better performance.

Both designs are tested when the power limits are enforced. Fig. 5.5 shows the comparison. It is obvious that design 2 leads to a more desirable performance. Design 1 will lead to various operation modes for batteries. One battery will work in charging mode whereas two will work in discharging mode.

5.2.6 Test System Circuit Configuration

The system to be investigated is a 14-bus microgrid model composed of three detailed battery modules with parallel adjustable loads and an induction machine. The entire system can be linked to the AC grid through a transmission line and breaker, illustrated in Fig. 5.6. Each inverter has the capability to connect to the main system and perform the independent power control. However, an energy management technique for energy storage system will also be supplemented to

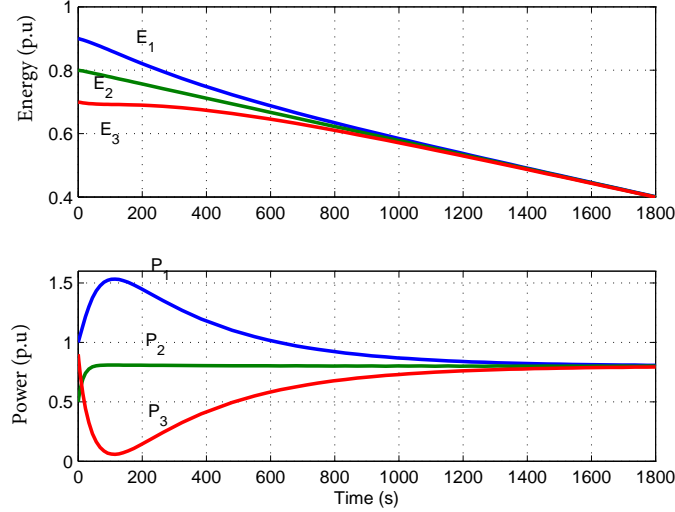


Figure 5.3. Simulation results of the analysis model; $Q = \text{diag}([800, 10])$, $R = 200$, $K_1 = -20$, $K_2 = 2.23860$, $c = 0.01$.

the primary power control loops which will be discussed shortly. In a case that the microgrid loses the connection to the grid, primarily, the battery inverters should be able to retain the voltage and frequency. Many parameters of the system are selected as: battery voltage level is 400 V, grid voltage is 13.8 kV, battery size is 100 kW/200 kWh, transmission lines have the same impedance of $0.0825 + j0.284\Omega/kM$. The detailed parameters of the system are provided in Table A.4, Table A.5, Table A.6, and Table A.7 of Appendix A.

5.2.7 Detailed Battery Models

Several battery models have been proposed for the past few years. However, electrical models provide more accuracy, and a balance between electrochemical and mathematical battery models. The electrical models are composed of voltage sources, resistors, and capacitors, which are the best options for co-simulations. There are several electrical models such as: impedance based, Thevenin based, and runtime based [104]. The same model developed in [96] is adopted in this research, which provides an accurate electrical model with transient and steady state dynamic response. Such a model is illustrated in Fig. 5.7.

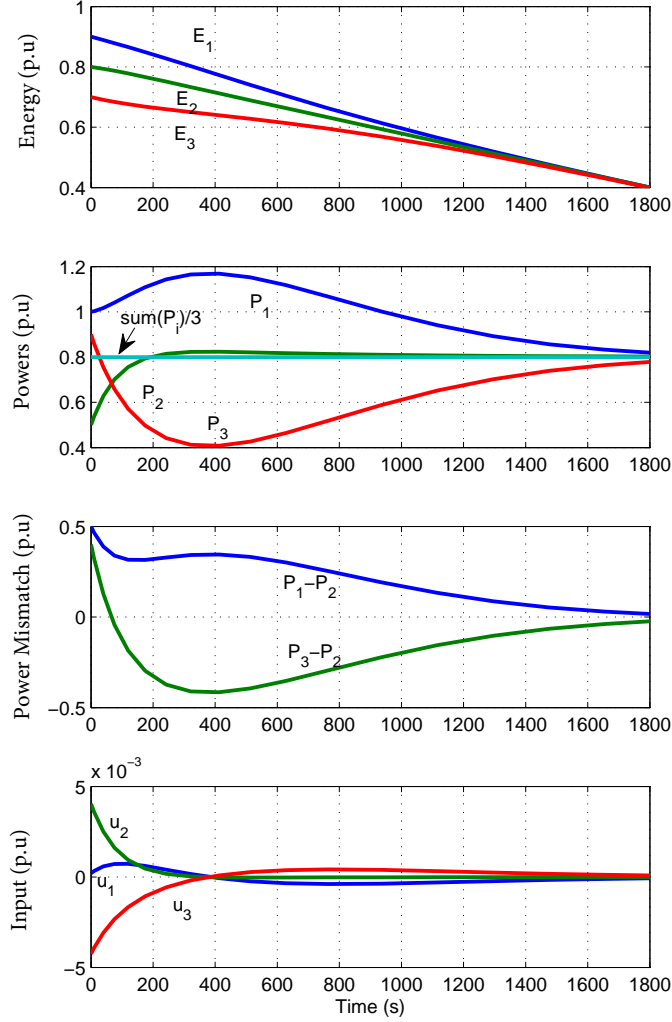


Figure 5.4. Simulation results of the analysis model; $Q = \text{diag}([300, 10])$, $R = 5000$, $K_1 = -2.4495$, $K_2 = 0.4487$, $c = 0.01$.

In this study, each battery is designed for 100 kW base power and is chosen to be the Li-ion type. The capacity of the battery in Farad (C_c), which defines the full capacity when it is fully charged, is expressed by :

$$C_c = 3600 \frac{P_n \cdot f_1 \cdot f_2}{V_n} \quad (5.16)$$

where P_n is the nominal energy of the battery in Whr, V_n is the nominal battery voltage, f_1 and f_2 are correction factors. Parameters of the battery then can be derived by:

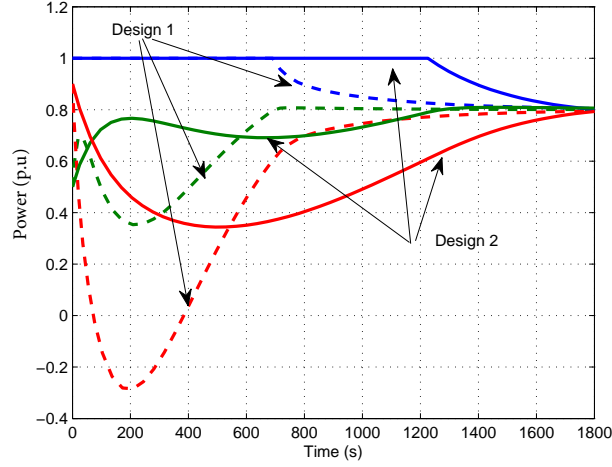


Figure 5.5. Comparison of two designs when power limits are enforced.

$$\begin{aligned}
 V_{SOC} &= -1.03e^{-35SOC} + 3.6 + 0.2SOC - 0.1SOC^2 + 0.3SOC^3 \\
 R_s &= 0.1562e^{-24.37SOC} + 0.07446 \\
 R_{TS} &= 0.3208e^{-29.14SOC} + 0.04669 \\
 C_{TS} &= -752.9e^{-13.51SOC} + 703.6 \\
 R_{TL} &= 6.603e^{-155.2SOC} + 0.04984 \\
 C_{TL} &= -6065e^{-27.12SOC} + 4475
 \end{aligned} \tag{5.17}$$

It should be mentioned that, R_{SD} is the self discharge resistor, R_{TS} is the short transient resistor, R_s is the series resistor, and R_{TL} is the long transient resistor. C_{TS} and C_{TL} are short and long transient capacitors. In this study, P_n is set to 200 kWh and V_n is set to 400 V. Derived parameters are then tested to validate the accuracy of designed battery. The detailed battery model is then connected to an inverter to convert the DC signals to AC as illustrated in Fig. 5.6.

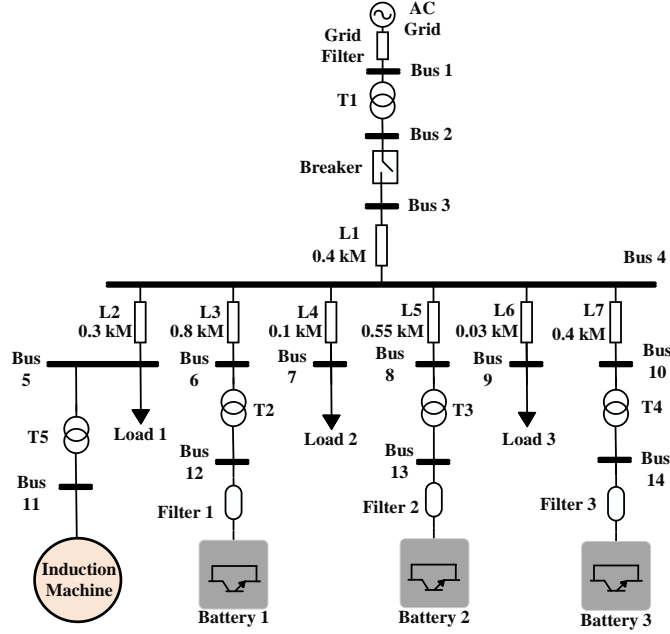


Figure 5.6. Microgrid system composed of battery energy storage systems and loads.

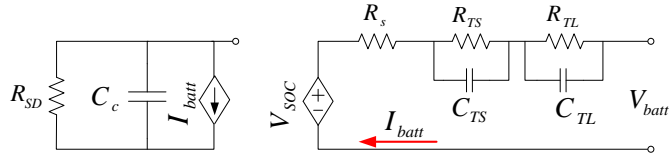


Figure 5.7. Detailed electrical battery model.

5.2.8 Battery Converter Controls

The converter control blocks are shown in Fig. 5.8, including inner current control, power following control, voltage controller, primary frequency control, and secondary frequency control. The consensus control input is notated as u_i in Fig. 5.8. This signal combined with the frequency deviation will be fed into an integrator to generate power orders.

The inner current loops are in charge of generating reference voltages in dq frame based on input reference currents in dq frame. The feed-forward items v_{fd} and v_{fq} are the point of common coupling (PCC) voltage in the dq reference frame passed from a low pass filter to mitigate the unwanted harmonics from the PCC (Bus 4) voltage [44]. The transfer function of the first order

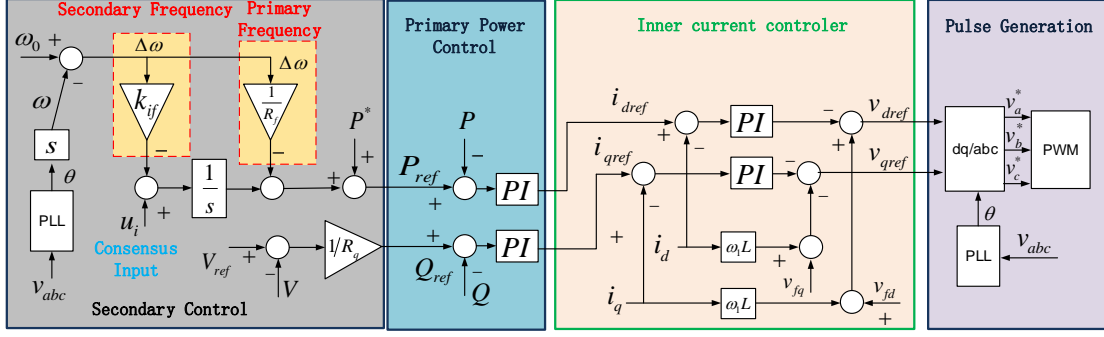


Figure 5.8. Battery converter control blocks.

filter is expressed as:

$$G_f(s) = \frac{\alpha_f}{s + \alpha_f} \quad (5.18)$$

Dynamic equations related to the inner current loop are given below:

$$\bar{v}_{ref} = \left(k_{pi} + \frac{k_{ii}}{s} \right) (\bar{i}_{ref} - \bar{i}) - j\omega L \bar{i} + \bar{v}_f \quad (5.19)$$

where $\bar{v}_{ref} = v_{dref} + jv_{qref}$, $\bar{i}_{ref} = i_{dref} + ji_{qref}$, $\bar{i} = i_d + ji_q$, and $\bar{v}_f = v_{fd} + jv_{fq}$ is the filtered battery voltage in dq frame.

The next control level is the power control. Two PI controllers are used to force the steady state error to zero. Dynamic equations of the power control loop are given below:

$$\begin{aligned} i_{dref} &= \left(k_{pp} + \frac{k_{ip}}{s} \right) (P_{ref} - P) \\ i_{qref} &= \left(k_{pp} + \frac{k_{ip}}{s} \right) (Q_{ref} - Q). \end{aligned} \quad (5.20)$$

Primary frequency control is designed as a primary droop control and the secondary frequency control will provide a frequency control in the case of dynamic events. Frequency and frequency deviations are measured by the PLL block. Primary voltage control is also equipped for reactive

power sharing. Dynamic equations of the primary control loops are provided below:

$$\begin{aligned}
 P_{ref} &= P^* + (\omega_0 - \omega) \left(\frac{-1}{R_f} + \frac{-k_{if} + u_i}{s} \right) \\
 Q_{ref} &= (V_{ref} - V) \frac{1}{R_q}
 \end{aligned} \tag{5.21}$$

where R_f is the droop gain for active power droop controller loop, R_q is the droop gain for reactive power droop loop, and k_{if} is the secondary frequency controller gain to bring the steady state frequency deviation to zero. Furthermore, u_i is the consensus distributed secondary controller input, which will be designed shortly, ω_0 is the reference angular frequency in p.u, P^* is the initial reference active power command, and V_{ref} is the reference magnitude of the voltage control loop.

In the grid-connected mode, $\Delta\omega$ will be zero and frequency control loops will be deactivated. However, the consensus control inputs still will be activated for grid connected mode, which enables the energy management technique without having to deactivate the control loops.

The combined signal of consensus input and frequency deviation has a similar representation of Area Control Error (ACE) signal employed in power systems for tie-line power scheduling and secondary frequency control. The innovative design showing in this chapter is the first of such in the literature for converter coordination.

The controller parameters are listed in Table 5.1.

Table 5.1. Parameters of controllers

Control	Value
Inner current	$k_{pi}=5, k_{ii}=100$
Outer power	$k_{pp}=0.1, k_{ip}=100$
Secondary frequency	$k_{if1} = 0.01, k_{if2} = 0.02, k_{if3} = 0.04$
Primary frequency	$R_{f1} = 0.04, R_{f2} = 0.06, R_{f3} = 0.08$
Reactive droop	$R_{q1}= 0.002, R_{q2}= 0.0025, R_{q3}= 0.0033$

5.3 Results

5.3.1 RT-Lab Simulation Results

In this section, real-time simulations with RT-LAB are conducted to validate the results of analysis and designed controller performance. The main advantages of the real time simulators are their fast response, real time runtime, and precision. By separating each simulation model into different subsystems, RT-LAB, which has multiple processing cores, will assign each subsystem to be compiled in one core. Therefore, the entire simulation can be run concurrently in multiple cores to increase the simulation speed.

The power electronic devices details are entirely included in the switching. Such switching details make the results of real time simulators to be close to the real-world system. Two case studies are carried out: (1) a discharging case when the microgrid is in islanded mode, and (2) a charging case when the microgrid is in grid-connected mode.

5.3.2 Discharging Event

A discharging event is designed to evaluate the response of the designed consensus control when the microgrid is working in the islanded mode and thus the energy storage should support the loads. In this case, initially a 66 kW load is considered. The SOC and power levels of batteries are all different. The consensus control is enabled after 300 seconds. The consensus control parameters are $cK_1 = -0.0822$, $cK_2 = 0.042$. SOC and power levels achieve consensus at 2300 seconds. At about 2458.5 seconds, a 30 kW load increase occurs. After the transient due to frequency control, SOC and power consensus again are achieved. Simulation results are shown in Figs. 5.9, 5.10 and 5.11.

5.3.3 Charging Event

This case is considered to evaluate the designed consensus control performance for a charging case. Simulation results for a charging event are illustrated in Fig. 5.12. The total charging power is 96 kW. Before the consensus control is enabled, each battery is charged at different power level.

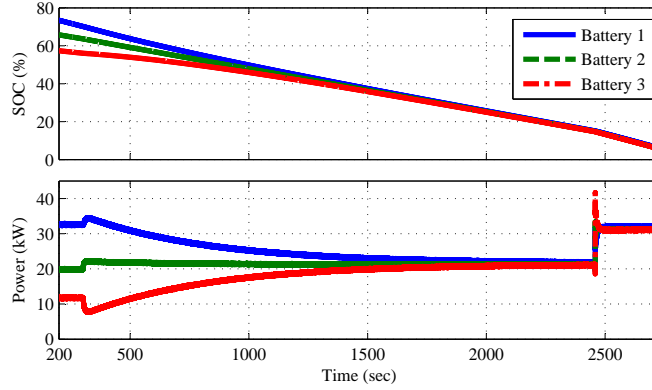


Figure 5.9. Discharging case; consensus control has been enabled at 300 seconds and consensus achieves at 2300 seconds and power levels achieve consensus at 2600 seconds, each 32 kW.

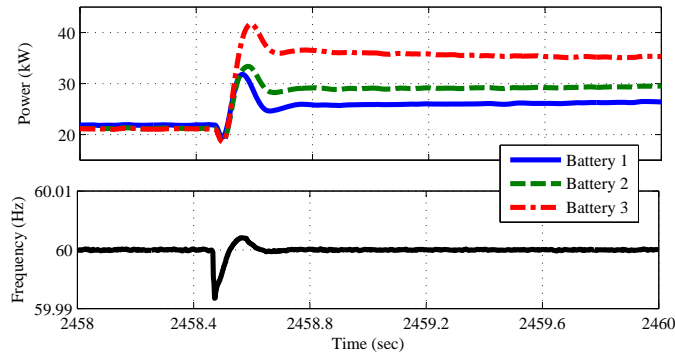


Figure 5.10. Load increase occurs at 2458.5 seconds, frequency is brought back to 60 Hz by secondary frequency control, battery power levels are different at 2458.5 seconds due to various gains for secondary frequency control: $K_{if1} = 0.01, K_{if2} = 0.02, K_{if3} = 0.04$.

After the consensus control is activated, SOC and power levels achieve consensus at 2500 seconds. The consensus control parameters are $cK_1 = -0.0513, cK_2 = 0.018$.

5.4 Discussions

This chapter applies consensus control to design battery coordination schemes. The design objective is to synchronize the SOC and power regardless of charging, discharging, or load varying operating modes. The main contribution is to treat the battery's SOC, power, and consensus control input as a double integrator system. The main assumption used in this design is; (i) there is an integrator to generate power order, and (ii) the consensus dynamics are much slower than the rest

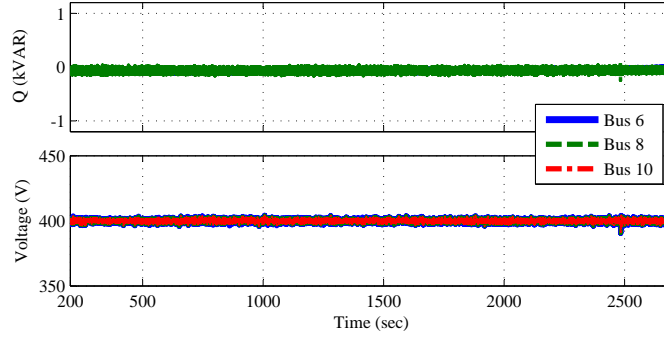


Figure 5.11. Reactive power and voltage for three batteries; the reference reactive power is set to 0 and voltage reference is set to 400 V.

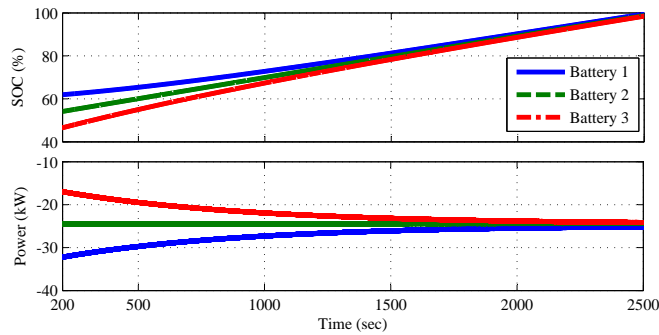


Figure 5.12. A charging event shows power and SOC consensus are achieved after around 2500 seconds.

of the system dynamics with primary and secondary control. Accordingly, the assumption of the double integrator as the plant model is valid. This design philosophy renders a simple distributed control design with only SOC and power as exchange information.

The proposed design also considers real-world battery operations and experiments various cases to guarantee that all the batteries operate at the same mode and power limits are met. The design is validated by RT-lab simulation for a high-fidelity 14-bus microgrid system with three batteries. Demonstration is carried out for a discharging, a load change, and a charging event. Simulation results proved the superior performance of the proposed consensus control.

CHAPTER 6

IMPEDANCE MODELING AND MIMO ANALYSIS

This chapter investigates the impedance modeling and MIMO analysis for vector control and power synchronization control of HVDC transmission system when connected to very weak AC grid.

6.1 Introduction

Conventional Line Current Commutating Converter (LCC)-HVDC transmission systems can not perform properly if the AC system is not strong enough [105, 106, 107]. The strength of an AC system is commonly defined by Short Circuit Ratio (SCR), which depends on HVDC nominal power and the strength of the AC system. Normally, systems with SCR values of less than 1.5 are considered as weak AC systems [108, 109, 44]. In contrast to the traditional HVDC transmissions, Voltage Source Converter HVDC (VSC-HVDC) has the ability to connect to weak AC grids without any reactive compensation [110]. Vector current control is a popular control scheme in the VSC-HVDC systems [111, 112]. Vector control of the VSC-HVDC not only is able to be linked to weak AC grids, but also provides an independent active or reactive power support to the grid [113, 114].

However, there are some barriers regarding vector control of VSC, especially when it is linked to a very weak AC grid. Studies have shown that vector current control of VSC-HVDC cannot transfer the power of more than 0.4 p.u once connected to a grid with *SCR* level of 1 [115, 46]. Analytical studies indicated that the limiting factors of vector control can be the current control grid interactions [44, 47] and/or PLL dynamics [44, 47, 48]. It is mentioned in [44, 47] that low frequency resonances may interact with the vector current control in weak AC systems. Additionally, the PLL dynamics will cause problems when the converter is synchronized with the weak grid. To overcome

the weak grid issue, [48] applied gain scheduling to design the the outer loop power/voltage, which resulted in an increase in power transfer.

Another solution is Power Synchronization Control (PSC). Compared to the gain scheduling control where the controller's gain varies, PSC serves as a classical controller with a fixed structure and parameters. The PSC has also been shown as a superior alternative for vector control in weak AC grids [46, 116, 117, 118, 119]. Unlike the PLL that synchronizes the converter to the Point of Common Coupling (PCC), the PSC directly synchronizes the converter to the grid through a power control loop.

The application of the PSC has also been studied in a few papers. In the first paper on the PSC [46], the power synchronization is introduced as an alternative to the conventional vector control in weak AC systems. In [116], the PSC performance is evaluated in connection of two very weak AC grids. The effect of different parameters on the stability of the system is also investigated. The application of the PSC for offshore wind farms is introduced in [117]. Stability limitations of various control loops in HVDC system enhanced with PSC are studied in [118]. They found that the alternating voltage control provides more stability compared to reactive power control when PSC is used in weak AC systems. Moreover, the impact of the converter with the PSC control on Sub-Synchronous Resonance (SSR) damping is studied in [119], showing that the PSC can greatly improve the damping of SSR modes.

The key contribution of this chapter is to derive an impedance model of PSC, carry out stability analysis, and compare PSC with vector control. In the original PSC paper, the power/angle transfer function is used to perform stability analysis. The impedance modeling approach is a popular approach adopted in converter related stability analysis [42, 44, 45, 120, 121]. The impedance model of converters with vector control has been developed in the literature, as shown in [47, 44]. However, the derived impedance is not exactly the same for the VSC-HVDC system used in this study.

The impedance model of a VSC with PSC has been derived in [119] with the main focus on sub-synchronous damping in the presence of synchronous generators. In addition, [119] focuses on analyzing the real part of the total impedance matrix (converter + grid) and MIMO system

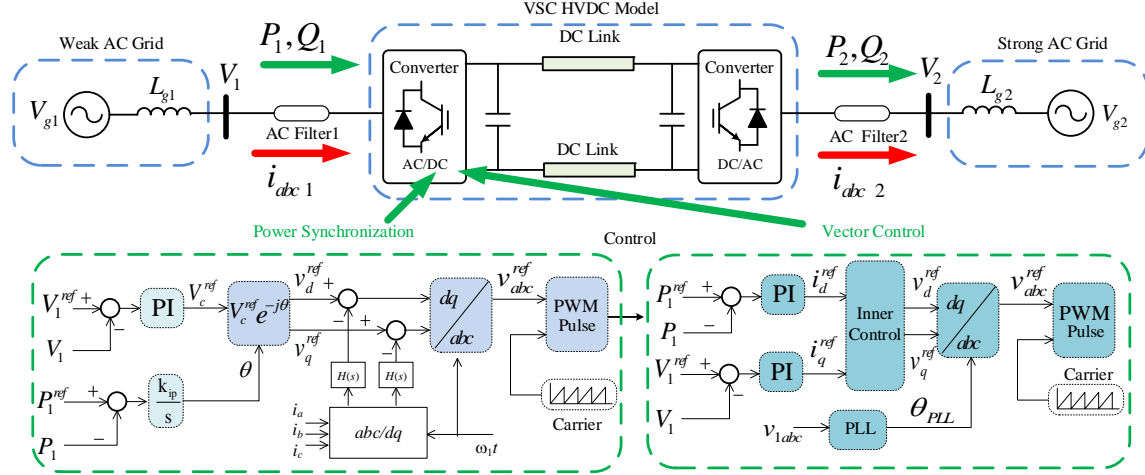


Figure 6.1. Back-to-back VSC-HVDC connected to a weak AC grid with two different controls at the rectifier side.

analysis techniques were not adopted. The effect of PSC on weak AC grids by impedance-based analysis yet to be studied.

This dissertation will present an impedance-model based MIMO analysis for a back-to-back VSC-HVDC system connected to a weak AC grid. Nyquist theory and the singular value of the return matrix are applied for the stability and robustness analysis, respectively. The eigen loci and singular value plots of the return difference matrix are employed in the MIMO stability analysis. The circuit and control diagrams are shown in Fig. 6.1. PSC is implemented on the rectifier side converter of the VSC-HVDC system. For comparison, the impedance models for vector control of VSC-HVDC are also derived. Two types of vector controls (with and without power outer loops) will be examined.

6.2 Methodology

6.2.1 Power Synchronization Control

Fig. 6.2 illustrates a simple representation of the system in Fig. 6.1. $Z_g = R_g + j\omega_1 L_g$ is the total impedance of the weak AC grid and its transformer, Z_{conv} is the impedance which is seen from the converter point of view, v_c is the converter output voltage and v_{g1} is grid voltage. The AC filter is considered as a simple L filter. As it can be observed, the rectifier side is equipped with

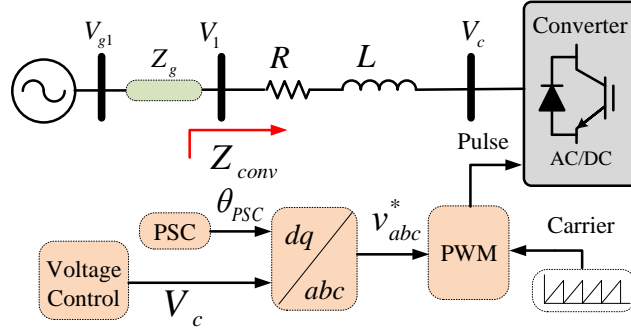


Figure 6.2. Simplified model of the system with PSC; $R = 0 \Omega$, $L = 0.04 \text{ H}$, $R_g = 0.1 \Omega$, $L_{g1} = 0.25 \text{ H}$ for $SCR = 1$, $L_{g1} = 0.088 \text{ H}$ for $SCR = 2$ and $L_{g1} = 0.048 \text{ H}$ for $SCR = 3$.

the PSC and an alternating voltage control. The main equation of the system in time domain and based on dq reference frame can be expressed by:

$$\bar{V}_1 - \bar{V}_c = L \frac{d\bar{I}}{dt} + j\omega_1 L \bar{I} + R \bar{I} \quad (6.1)$$

where \bar{V} is the complex voltage and \bar{I} is the complex vector for the current ($\bar{V}_1 = v_{1d} + jv_{1q}$, $\bar{I} = i_d + ji_q$ and $\bar{V}_c = v_{cd} + jv_{cq}$) in the dq -reference frame, which are rotating at the speed of ω_1 . The converter output voltage is defined as:

$$\bar{V}_c = V_c e^{-j\theta} = V_c \cos(\theta) - jV_c \sin(\theta) \quad (6.2)$$

where θ is the output from the power control. Replacing (6.2) in (6.1) and separating it to dq components:

$$\begin{aligned} v_{1d} - V_c \cos \theta &= L \frac{di_d}{dt} - \omega_1 L i_q + R i_d \\ v_{1q} + V_c \sin \theta &= L \frac{di_q}{dt} + \omega_1 L i_d + R i_q \end{aligned} \quad (6.3)$$

The key structure of the PSC is illustrated in Fig. 6.1. The idea behind the PSC comes from the analogy of power angle relationship in synchronous machines [46]. In PSC, synchronization takes place through active power control loop and the output is used as the reference angle for VSC

PWM unit. By applying this method, the PLL is not needed. Referring to Fig. 6.1, the difference between the reference active power of the converter and the measured power is sent to an integrator controller ($\frac{K_{ip}}{s}$), and the output of which represents the synchronization angle (θ).

$$\theta(s) = \frac{K_{ip}}{s}(P^{ref}(s) - P(s)), \quad \theta_{PSC} = \omega_1 t - \theta. \quad (6.4)$$

The small-signal equations of active and reactive power are as follows:

$$\begin{aligned} \Delta P &= \Delta v_{1d}i_{d0} + \Delta i_d v_{1d0} + \Delta v_{1q}i_{q0} + \Delta i_q v_{1q0} \\ \Delta Q &= \Delta v_{1q}i_{d0} + \Delta i_d v_{1q0} - \Delta v_{1d}i_{q0} - \Delta i_q v_{1d0} \end{aligned} \quad (6.5)$$

Therefore, the small-signal representation of power synchronization loop is derived:

$$\Delta \theta = -\frac{K_{ip}}{s}(\Delta v_{1d}i_{d0} + \Delta i_d v_{1d0} + \Delta v_{1q}i_{q0} + \Delta i_q v_{1q0}) \quad (6.6)$$

6.2.2 Transfer Function from Angle to Power

Given the power control loop, it is natural to seek the relationship between complex power S injected to the converter versus the voltage magnitude V_c and the angle θ . The small-signal model of the complex power in the dq reference frame is used for analysis. A comparison of such derivation and the one presented in [46] verifies that the following derivation employs the concept of line impedance model and is very easy to follow.

In the synchronous rotating frame, the converter voltage complex vectors and the grid voltage complex vectors are as follows:

$$\bar{V}_c = V_c \angle -\theta, \quad \bar{V}_{g1} = V_{g1} \angle 0 \quad (6.7)$$

where V_{g1} is assumed to be constant, while V_c and $-\theta$ are controllable.

The electromagnetic dynamics of the line will not be neglected. As a result, the current and voltage relationship in the dq reference frame is expressed as:

$$\bar{I}(s) = \frac{\bar{V}_{g1}(s) - \bar{V}_c(s)}{\tilde{R} + (s + j\omega_1)\tilde{L}}. \quad (6.8)$$

where \tilde{R} and \tilde{L} are the total line resistance and line inductance between the two nodes. Note that the line impedance model in abc reference frame is $\tilde{R} + s\tilde{L}$, while in a synchronous reference frame it becomes $\tilde{R} + (s + j\omega_1)\tilde{L}$.

Complex power to the converter $S = \bar{V}_c \bar{I}^*$ can be expressed in Laplace domain as:

$$\Delta S(s) = \bar{V}_{c0} \Delta \bar{I}^*(s) + \bar{I}_0^* \Delta \bar{V}_c(s) \quad (6.9)$$

where the subscript 0 notates the initial conditions.

Substituting $\Delta \bar{I}(s)$ in the above equation by (6.8), assuming the grid voltage is constant ($\Delta \bar{V}_{g1} = 0$), we have

$$\Delta S = -\frac{\bar{V}_{c0}}{\tilde{R} + (s - j\omega_1)\tilde{L}} \Delta \bar{V}_c^*(s) + \bar{I}_0^* \Delta \bar{V}_c(s) \quad (6.10)$$

Note that $\bar{V}_c = V_c e^{-j\theta}$, therefore in Laplace domain it will be:

$$\Delta \bar{V}_c = -jV_{c0} e^{j\theta_0} \Delta \theta + e^{-j\theta_0} \Delta V_c \quad (6.11)$$

$$= -jV_{c0} \Delta \theta + e^{-j\theta_0} \Delta V_c \quad (6.12)$$

Substituting ΔV_c and ΔV_c^* in (6.10) by (6.12) leads to (6.13).

$$\Delta S = \begin{bmatrix} \frac{jV_{c0}^2}{\tilde{R} + (s - j\omega_1)\tilde{L}} - jS_0 \\ \frac{-V_{c0}}{\tilde{R} + (s - j\omega_1)\tilde{L}} - I_0 \end{bmatrix}^T \begin{bmatrix} \Delta \theta(s) \\ \Delta V_c(s) \end{bmatrix} \quad (6.13)$$

Separating the real and imaginary parts, we can find $\Delta P = J_{P\theta}\Delta\theta + J_{PV}\Delta V_c$. The power to angle transfer function can be found as:

$$J_{P\theta} = Q_0 - \frac{\omega_1 L V_{c0}^2}{(\tilde{R} + s\tilde{L})^2 + (\omega_1 \tilde{L})^2} \quad (6.14)$$

The above transfer function indicates that there are 60 Hz resonances due to the line electromagnetic dynamics. This phenomenon has been mentioned in [46] and a high-pass filter is used to increase the damping of this oscillation mode. The control idea is to increase the total resistance by introducing a virtual resistance via a high-pass filter. The resulting power angle transfer function becomes:

$$J_{P\theta} = Q_0 - \frac{\omega_1 L V_{c0}^2}{(\tilde{R} + H(s) + s\tilde{L})^2 + (\omega_1 \tilde{L})^2} \quad (6.15)$$

where $H(s)$ is the filter transfer function. The virtual resistance will provide damping at 60 Hz. A high pass filter will fulfill this task: $H(s) = \frac{0.5s}{s+40}$. The implementation of the filter should be in the dq reference frame with a constant rotating speed ω_1 as shown in Fig. 6.1.

6.2.3 Alternating Voltage Control Loop

As illustrated previously in Fig. 6.1, the AC voltage controller regulates the magnitude of the rectifier voltage to maintain the grid side voltage. A simple PI regulator is used to control the voltage magnitude, the output of which is employed to generate the reference dq -axis currents of the converter. Dynamic equation for the alternating voltage controller can be expressed by [119]:

$$V_c = \left(k_{pv} + \frac{k_{iv}}{s} \right) (V_1^{ref} - V_1). \quad (6.16)$$

where V_1^{ref} is the reference magnitude of the PCC voltage, and V_1 is the measured magnitude of PCC voltage, $\sqrt{v_{1d}^2 + v_{1q}^2}$. Therefore, the small signal representation of V_1 can be represented by:

$$\Delta V_1 = \frac{1}{V_1} (v_{1d0}\Delta v_{1d} + v_{1q0}\Delta v_{1q}) \quad (6.17)$$

Applying small-signal analysis in (6.16) and replacing ΔV_1 by (6.17) leads us to:

$$\Delta V_c = -\frac{k_{pv} + \frac{k_{iv}}{s}}{V_1} (v_{1d0}\Delta v_{1d} + v_{1q0}\Delta v_{1q}) \quad (6.18)$$

6.2.4 Impedance Model of VSC with PSC Control

In this subsection, impedance model of the PSC converter viewed from the PCC bus is derived. The effect of voltage control loop is considered in the derivation, while the effect of the high pass filter will be added after the derivation.

Separating the real and imaginary parts of (6.2) will result in:

$$\begin{aligned} \Delta v_{cd} &= \cos \theta_0 \Delta V_c - V_{c0} \sin \theta_0 \Delta \theta \\ \Delta v_{cq} &= -\sin \theta_0 \Delta V_c + V_{c0} \cos \theta_0 \Delta \theta. \end{aligned} \quad (6.19)$$

The small-signal model of (6.1) is as follows.

$$\begin{aligned} \Delta v_{1d} - \Delta v_{cd} &= (Ls + R)\Delta i_d - \omega_1 L \Delta i_q \\ \Delta v_{1q} + \Delta v_{cq} &= \omega_1 L \Delta i_d + (Ls + R)\Delta i_q \end{aligned} \quad (6.20)$$

Substituting (6.6) and (6.18) into (6.19), and finally into the above equation and reorganizing the equations, the following equations can be obtained:

$$\begin{aligned} A\Delta v_{1d} + B\Delta v_{1q} &= C\Delta i_d + D\Delta i_q \\ E\Delta v_{1d} + F\Delta v_{1q} &= G\Delta i_d + H\Delta i_q \end{aligned} \quad (6.21)$$

where, A, B, C, D, E, F, G, H are expressed as:

$$\begin{aligned}
A &= 1 + \left(k_{pv} + \frac{k_{iv}}{s} \right) \cos \theta_0 - V_{10} \sin \theta_0 i_{d0} \frac{k_{ip}}{s} \\
B &= -V_{10} \sin \theta_0 i_{q0} \frac{k_{ip}}{s} \\
C &= (Ls + R + V_{10}^2 \sin \theta_0) \frac{k_{ip}}{s} \\
D &= -\omega_1 L \\
E &= - \left(k_{pv} + \frac{k_{iv}}{s} \right) \sin \theta_0 - \frac{k_{ip}s}{V_{10}} \cos \theta_0 i_{d0} \\
F &= 1 - V_{10} \cos \theta_0 i_{q0} \frac{k_{ip}}{s} \\
G &= \omega_1 L + V_{10}^2 \cos \theta_0 \frac{k_{ip}}{s} \\
H &= Ls + R
\end{aligned}$$

Simplifying (6.21) and writing it in a matrix form:

$$\begin{bmatrix} \Delta v_{1d} \\ \Delta v_{1q} \end{bmatrix} = \underbrace{\begin{bmatrix} A & B \\ E & F \end{bmatrix}^{-1} \begin{bmatrix} C & D \\ G & H \end{bmatrix}}_{Z_{cp}} \begin{bmatrix} \Delta i_d \\ \Delta i_q \end{bmatrix} \quad (6.22)$$

where Z_{cp} is a 2×2 converter impedance matrix with PSC. Considering the high-pass filter, the impedance is expressed as:

$$Z_{conv} = \begin{bmatrix} H(s) & 0 \\ 0 & H(s) \end{bmatrix} + Z_{cp}. \quad (6.23)$$

6.2.5 Impedance of Vector Control

In order to calculate the impedance of a vector controlled converter with outer loops and a PLL, the dynamic equations of the converter output voltage, referring to Fig. 6.1, should be considered.

The dynamics of inner current controller can be expressed as [44]:

$$\bar{V}_c^c = - \left(k_p + \frac{k_i}{s} \right) (\bar{I}_{ref}^c - \bar{I}_1^c) - j\omega L \bar{I}_1^c + \frac{1}{s\tau + 1} \bar{V}_1^c \quad (6.24)$$

where superscript c denotes the converter $d-q$ frame, \bar{V}_1^c is the PCC voltage converted to dq frame, and I_1 is the converter dq frame current obtained from I_{1abc} . It is noted that the time constant of the first order filter is 0.001 ($\tau=0.001$). Rearranging (6.24) and separating it to $d-q$ components [44]:

$$\mathbf{I}_1^c = \underbrace{\begin{bmatrix} g_c(s) & 0 \\ 0 & g_c(s) \end{bmatrix}}_{G_c(s)} \mathbf{I}_{ref}^c + \underbrace{\begin{bmatrix} y_i(s) & 0 \\ 0 & y_i(s) \end{bmatrix}}_{Y_i(s)} \mathbf{V}_1^c \quad (6.25)$$

where \mathbf{I}_1^c , \mathbf{I}_{ref}^c and \mathbf{V}_1^c are vectors of d -axis and q -axis variables in converter $d-q$ frame.

$$\begin{cases} g_c(s) = \frac{k_p s + k_i}{L s^2 + k_p s + k_i} \\ y_i(s) = \frac{s^2}{(L s^2 + k_p s + k_i)(s\tau + 1)} \end{cases} \quad (6.26)$$

Now, impedance of the vector controlled converter can be derived if \mathbf{I}_{ref} can be expressed by voltage and current vectors in the grid $d-q$ frame. The PLL is in charge of converting the components from the converter $d-q$ frame to the grid $d-q$ frame by synchronizing the angle. In the next subsections, the effect of outer loops and the PLL will be added to derive the impedance model of the vector controlled converter. Applying the small signal analysis to (6.25) will result in:

$$\Delta \mathbf{I}_1^c = \underbrace{\begin{bmatrix} g_c(s) & 0 \\ 0 & g_c(s) \end{bmatrix}}_{G_c(s)} \Delta \mathbf{I}_{ref}^c + \underbrace{\begin{bmatrix} y_i(s) & 0 \\ 0 & y_i(s) \end{bmatrix}}_{Y_i(s)} \Delta \mathbf{V}_1^c \quad (6.27)$$

6.2.6 Outer Loop Effects

Outer PI outer loops are illustrated in Fig. 6.5, where the d axis will control the active power and q axis is in charge of the converter output voltage. The dynamic equations of the outer loops

can be expressed as:

$$\begin{cases} I_{dref}^c &= (P_{ref} - P)F_{PI} \\ I_{qref}^c &= (V_{ref} - V_1)F_{VI} \end{cases} \quad (6.28)$$

where V_1 is the voltage magnitude of the PCC, V_{ref} is the reference PCC voltage magnitude, F_{PI} is the PI controller transfer function $(k_{pp} + \frac{k_{ip}}{s})$ for power control loop, and F_{VI} is the PI controller transfer function $(k_{pv} + \frac{k_{iv}}{s})$ to track the PCC voltage magnitude. Applying the small signal analysis to (6.28):

$$\begin{cases} \Delta I_{dref}^c &= -F_{PI}\Delta P \\ \Delta I_{qref}^c &= -F_{VI}\Delta V_1 \end{cases} \quad (6.29)$$

The magnitude of the PCC voltage can be derived by: $V_1 = \sqrt{V_{1d}^2 + V_{1q}^2}$, and the converter output active power can simply be derived by: $P = V_{1d}I_{1d} + V_{1q}I_{1q}$. Therefore, applying small signal analysis:

$$\Delta P = I_{1d0}\Delta V_{1d} + V_{1d0}\Delta I_{1d} + I_{1q0}\Delta V_{1q} + V_{1q0}\Delta I_{1q} \quad (6.30)$$

$$\begin{aligned} \Delta V_1 &= \frac{V_{1d0}\Delta V_{1d} + V_{1q0}\Delta V_{1q}}{\sqrt{V_{1d0}^2 + V_{1q0}^2}} \\ &= \frac{V_{d0}}{V_0}\Delta V_{1d} + \frac{V_{q0}}{V_0}\Delta V_{1q} \end{aligned} \quad (6.31)$$

By replacing the (6.30) and (6.31) into (6.29):

$$\Delta \mathbf{I}_{ref}^c = \underbrace{\begin{bmatrix} -F_{PI}v_{1d0} & -F_{PI}v_{1q0} \\ 0 & 0 \end{bmatrix}}_{G_1(s)} \Delta \mathbf{I}_1^c + \underbrace{\begin{bmatrix} -F_{PI}I_{d0} & -F_{PI}I_{q0} \\ -\frac{V_{d0}}{V_0}F_{VI} & -\frac{V_{q0}}{V_0}F_{VI} \end{bmatrix}}_{G_2(s)} \Delta \mathbf{V}_1^c \quad (6.32)$$

The impedance of the vector controlled converter with outer loops and without the PLL is then derived by substituting (6.32) into (6.27):

$$\Delta \mathbf{I}_1^c = \underbrace{\frac{G_e(s)G_2(s) + Y_i(s)}{I - G_e(s)G_1(s)}}_{[Z_{Rec}^c]^{-1}} \Delta \mathbf{V}_1^c \quad (6.33)$$

6.2.7 The PLL Effect

Impedance analysis of the PLL has been performed in [44] in detail. The final equations are adopted here and detailed analysis can be found in [44]. The main goal is to convert the \bar{I}_1^c and \bar{V}_1^c from the converter frame to the grid frame components (\bar{I}_1 and \bar{V}_1) by :

$$\begin{aligned} \Delta \mathbf{I}_1^c &= \Delta \mathbf{I}_1 - \underbrace{\begin{bmatrix} 0 & \frac{Q_0}{V_0} G_{PLL} \\ 0 & \frac{Q_0}{V_0} G_{PLL} \end{bmatrix}}_{G_{PLL}} \Delta \mathbf{V}_1 \\ \Delta \mathbf{V}_1^c &= \underbrace{\begin{bmatrix} 1 & 0 \\ 0 & 1 - V_{10} G_{PLL} \end{bmatrix}}_{G_{sPLL}} \Delta \mathbf{V}_1 \end{aligned} \quad (6.34)$$

where G_{PLL} is a simple PI controller as: $G_{PLL} = K_p^{PLL} + \frac{k_i^{PLL}}{s}$. For deriving the impedance model of the vector controlled converter with an outer power loop and the PLL effect, (6.34) is substituted into (6.33), then the result will be:

$$Z_{Rec}(s) = \frac{1}{G_{PLL} + [Z_{Rec}^c]^{-1} G_{sPLL}} \quad (6.35)$$

The derived impedance is combined with the grid impedance for the impedance and singular value analysis then.

6.2.8 Parameter Selection

For vector control, the inner current controller should be designed to respond faster than outer power control loops. For more information, the step by step procedure for vector control is given below. Same approach is used for PSC parameters.

The inner current controllers in the vector control should be designed to be much faster than the outer power control loops. The converter voltage in abc frame is notated as v_{abc} and the current is notated as i_{abc} . The voltage at the PCC is notated as v_1 . An RL circuit is considered between the converter and the PCC. Therefore:

$$L \frac{d\vec{i}}{dt} + R\vec{i} = \vec{v} - \vec{v}_1. \quad (6.36)$$

where $\vec{\cdot}$ is the space vector. In order to describe the above relationship, the dq reference frame is utilized. It is assumed that the d -axis will be aligned with the space vector of the PCC voltage, thus:

$$\begin{aligned} L \frac{d(i_d + ji_q)}{dt} + j\omega L(i_d + ji_q) + R(i_d + ji_q) \\ = v_d + jv_q - v_{1d}. \end{aligned} \quad (6.37)$$

Separating equation (6.37) into dq -axes, the plant model for the current control design is derived:

$$L \frac{di_d}{dt} + Ri_d = \underbrace{v_d - v_{1d} + \omega Li_q}_{u_d} \quad (6.38)$$

$$L \frac{di_q}{dt} + Ri_q = \underbrace{v_q - \omega Li_d}_{u_q} \quad (6.39)$$

The plant model for the current controller is assumed as $1/(R + sL)$ for both d and q axes. The inputs are u_d, u_q , while the outputs are i_d and i_q . The feedback controls are designed for the dq -axis to track the reference currents. In addition, to generate the dq components of the converter voltage, the cross coupling and feed-forward voltage terms should be added to the design. A simplified inner current control block is illustrated in Fig. 6.3. The loop gain of system is represented by:

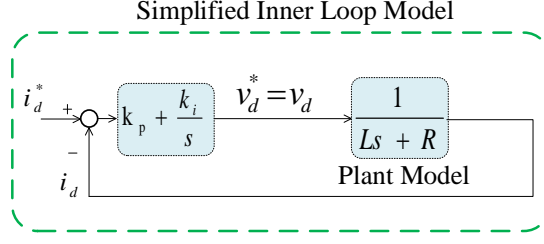


Figure 6.3. Simplified block diagram for inner loop control

$$l(s) = \frac{k_p}{Ls} \left(\frac{s + \frac{k_i}{k_p}}{s + \frac{R}{L}} \right). \quad (6.40)$$

As it is mentioned in [113], the plant pole is fairly close to the origin. Therefore, this plant pole is canceled by the compensator zero and the the loop gain becomes:

$$l(s) = \frac{k_p}{Ls} \quad (6.41)$$

The closed-loop transfer function can be represented as:

$$G_{Inner}(s) = \frac{l(s)}{1 + l(s)} = \frac{1}{\tau s + 1} \quad (6.42)$$

where $\tau = \frac{L}{k_p}$ and $k_i = \frac{R}{\tau}$. The inner loop gains are designed so that the bandwidth of the inner loop with $k_p = 50$, $k_i = 100$, and $L = 0.04H$ is around 1250 rad/s. Compared to the inner current controller, the outer loop is designed to be very slow to reflect the dynamic changes. The simplified outer control loop structure is illustrated in Fig. 6.3. As the dq reference frame is aligned with the PCC voltage, the real and reactive powers can be expressed as $P = V_1 i_d$ and $Q = V_1 i_q$. A closed-loop simplified transfer function is represented as:

$$G_{outer}(s) = \frac{\left(k_p + \frac{k_i}{s} \right) V_1}{1 + \left(k_p + \frac{k_i}{s} \right) V_1} = \frac{\frac{k_p}{k_i} s + 1}{\left(\frac{1}{V_1 k_i} + \frac{k_p}{k_i} \right) s + 1} \quad (6.43)$$

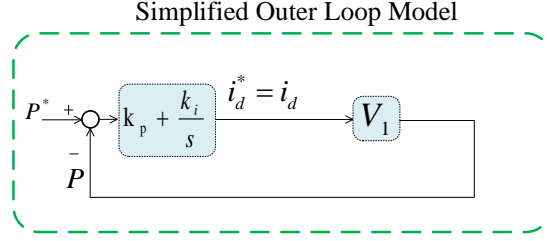


Figure 6.4. Simplified block diagram for outer loop control

This is a first order transfer function to the form of $\frac{as+1}{\tau s+1}$, where τ is the time constant ($\tau = \left(\frac{1}{V_1 k_i} + \frac{k_p}{k_i}\right)$) and the system bandwidth can be found as $1/\tau$. In this study, the outer loop gains are designed so that the bandwidth of the outer loop with $k_p = 0.1$ and $k_i = 5$ is 4 rad/s. This bandwidth is 300 times slower than the inner control bandwidth.

The AC voltage PI controller is designed based on $\Delta Q = V_1 \Delta i_q$, where V_1 is the PCC voltage. Furthermore, the PCC voltage change ΔV_1 is proportional to ΔQ . Hence, the plant model is derived as:

$$\Delta V_1 = \frac{\Delta Q}{SCR} = \frac{V_1}{SCR} \Delta i_q \quad (6.44)$$

The closed-loop system transfer function can be computed as:

$$\frac{\Delta V_1}{\Delta V_1^*} = \frac{k_p s / k_i + 1}{(k_p + SCR)s / k_i + 1} \quad (6.45)$$

It can be assumed that V_1 is approximately 1 pu. Therefore, the time constant and the bandwidth are as follows:

$$\tau = \frac{k_p + SCR}{k_i} \quad (6.46)$$

$$\omega_{bw} = 1/\tau \quad (6.47)$$

For $k_p = 0.01$, $k_i = 100$ and $SCR = 1$, the bandwidth is 100 rad/s. For $SCR = 2$, the bandwidth is 50 rad/s. More information regarding the bandwidth design can be found in [113].

6.3 Results

6.3.1 MIMO Stability Analysis and Validation

For grid-connected converter in current control mode, a Norton equivalent circuit should be developed, as shown in Fig. 6.5.

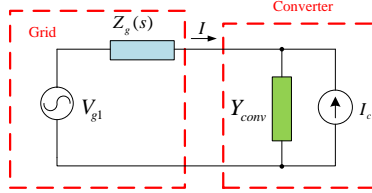


Figure 6.5. Impedance model of a converter connected to grid.

According to Fig. 6.5, the current passing from the grid to the converter can be derived [42]:

$$\begin{aligned}
 I(s) &= (Z_g + Z_{conv})^{-1}(V_{g1} - Z_{conv}I_c) \\
 &= (Z_g + Z_{conv})^{-1}Y_{conv}^{-1}Y_{conv}(V_{g1} - Z_{conv}I_c) \\
 &= [Y_{conv}Z_g + Y_{conv}Z_{conv}]^{-1}Y_{conv}(V_{g1} - Z_{conv}I_c) \\
 &= [I + Y_{conv}Z_g]^{-1}(Y_{conv}V_{g1} - I_c)
 \end{aligned} \tag{6.48}$$

For the above system, two assumptions are placed. (i) The grid voltage $V_{g1}(s)$ is stable; (ii) the current is stable when the grid impedance Z_g is zero, i.e., $Y_{conv}V_{g1}(s) - I_c(s)$ is stable. The first assumption is valid for the real-world scenarios as long as the grid voltage is within the limits. For properly designed converters, the second assumption is also true. Therefore, for the current $I(s)$ to be stable, we only need to examine the denominator: $I + Y_{conv}(s)Z_g(s)$. In order to claim that the system is stable, the zeros or roots of the characteristic function $\det(I + Y_{conv}(s)Z_g(s)) = 0$ should be located in the left half plane (LHP).

As both the grid and converter impedances are 2×2 matrices, the circuit analysis problem becomes a MIMO system stability problem. The MIMO system stability criterion is given in [122]. The characteristic function, $\det(I + Y_{conv}Z_g) = 0$ should have no zeros in the RHP.

Such stability criterion can be examined by checking the eigen loci or the Nyquist plots of the eigenvalues of $Y_{conv}Z_g$. If the eigen loci do not encircle $(-1, 0)$, then the system is stable. This technique has been extensively used in the impedance-based stability analysis of the power electronic converters [47, 121]. On the other hand, the minimum singular value in the frequency domain of the return difference matrix $I + Y_{conv}Z_g$ provides an index of gain margin and phase margin [123]. The singular value plots have been adopted in the authors' previous publication [124] to conduct impedance-based stability analysis. The minimum singular value indicates how close the return difference matrix is to singularity or $\det(I + Y_{conv}Z_g) \rightarrow 0$ at which frequencies. The greater the minimum singular value, the more robust the system. Resonance frequency can be identified as the frequency when the singular value is the minimum.

Results of the stability analysis will be validated by the high-fidelity model based simulation. The topology of the simulation model has been illustrated in Fig. 6.1 in detail. For real-time simulations, RT-LAB is considered. The detailed RT-LAB model includes switching details which can reflect the nonlinear behavior of the model perfectly. In addition to the PSC, two types of vector controls are designed for comparison. The first vector control type has an outer power controller loop, a fast inner current controller, and a PLL synchronization, shown in Fig. 6.1. The second type has no outer power control. Instead, the current references are computed directly from power reference. This type of the vector control has been analyzed in [47].

To verify the strength of the system in analysis and simulations, three different SCR values are considered; $SCR = 1$ resembles a very weak AC system, $SCR = 2$ for a normal AC system, and $SCR = 3$ which is a strong system. The base values to calculate the SCRs are included below: $V_{base}(LL) = 100$ kV, $S_{base} = 100$ MVA, $P_{HVDC} = 100$ MVA, $L_{f1} = 0.04$ H, $L_{g1} = 0.25$ H for $SCR = 1$, $L_{g1} = 0.088$ H for $SCR = 2$ and $L_{g1} = 0.048$ H for $SCR = 3$. The detailed system parameters are listed in Table A.8 to Table A.11 of Appendix A.

6.3.2 Impedance of the Converter for Different Control

In the first case, impedances of the converter are derived for three separate controls. Fig. 6.6 shows the 3D diagonal (dd) component of $Z_{conv}(s)$ with the three controllers, where the gray

surface is the surface where the real part of the impedance is zero. It is observed that with the power synchronization, the converter impedance is positive for the frequency ranges of more than 50 Hz for low power angles (or low power transfer level). It is also noted that as the power angle increases, the positive impedance occurs at a higher frequency. For instance, for the power angle of 80 degrees, the positive impedance happens at 70 Hz. Therefore, as the angle increases, the impedance becomes more negative at fundamental frequency. Compared to the power synchronization, the vector control has negative impedance for frequency ranges of less than 120 Hz in low power angles. With an increase in the power angle, the impedance will be more negative. This shows that the PSC provides a positive impedance or more damping within the frequency ranges where the vector control provides a negative impedance.

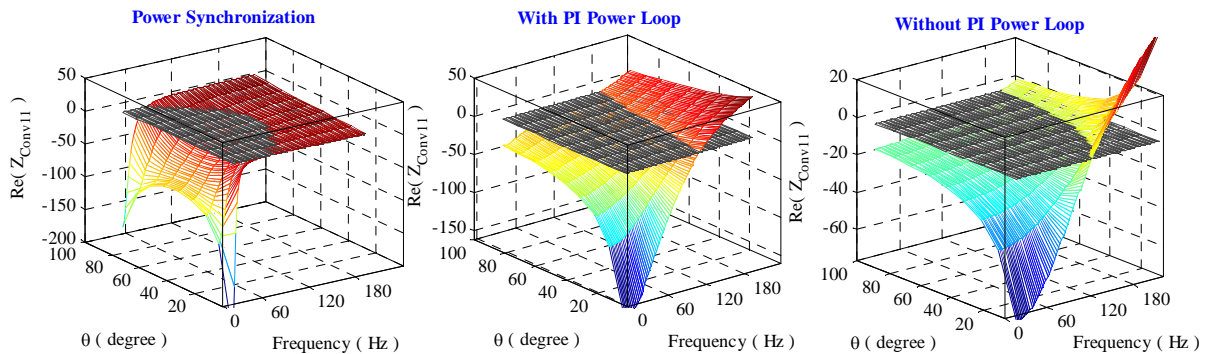


Figure 6.6. Comparison between real parts of converter impedances, $Z_{conv}(s)$ for different controllers of rectifier side converter.

6.3.3 Stability under Different SCR Scenarios

The first case study is designed to compare PSC and two other types of vector control for systems with different SCRs. The Nyquist plots for different controllers are illustrated in Fig. 6.7 and the singular plots for the return matrix are shown in Fig. 6.8.

Fig. 6.7 shows that for $SCR = 3$ none of the Nyquist plots encircles $(-1,0)$ in a clockwise direction. All the control methods result in stable system operation. When the SCR decreases, all the control methods's performance deteriorates due to the gain and phase margins reduction, illustrated in Fig. 6.7. While the PSC shows robustness against the SCR change, the vector control

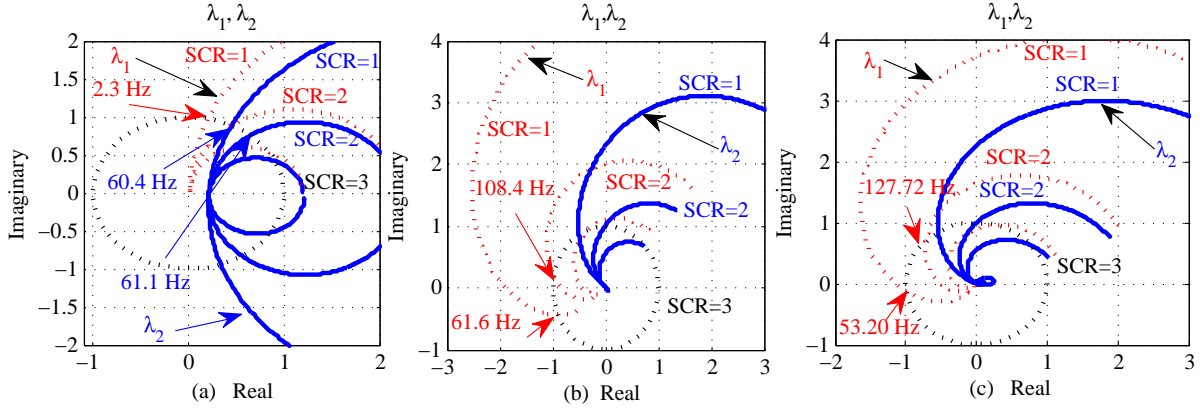


Figure 6.7. Comparison of eigen loci of $Z_g(s)Y_{conv}(s)$ for different SCR values and controllers of the rectifier side converter; power transfer level is 100 MW; (a) PSC; (b) vector control with PI power loop; (c) vector control without PI power loop.

methods deteriorate. By decreasing the SCR to 1, the vector controls encircle the point $(-1, 0)$ in a clockwise direction, indicating instability. However, the PSC still provides robust performance.

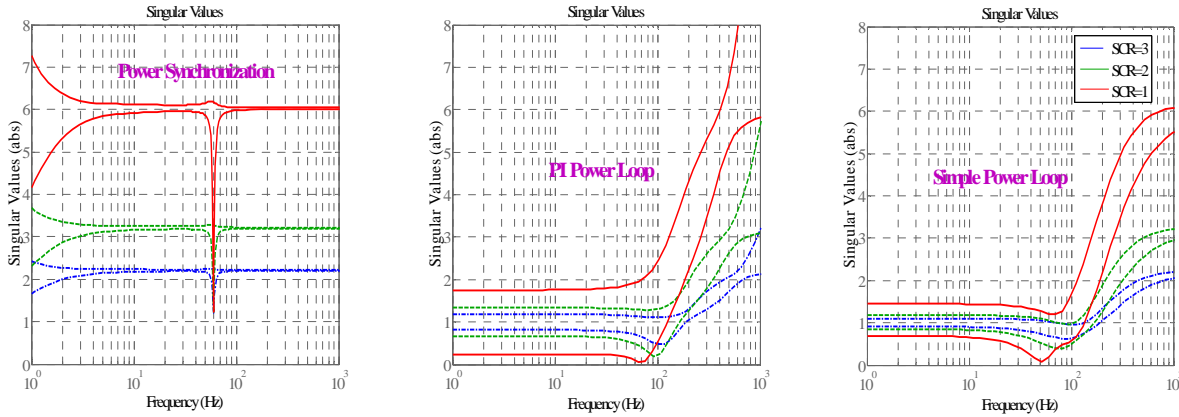


Figure 6.8. Comparison of singular value plots of $I + Z_g(s)Y_{conv}(s)$ for the different SCR values and controllers of the rectifier side converter; power transfer level is 100 MW; high pass filter is included for the PSC.

The singular value plots show that PSC with the high pass filter has the minimum singular values of greater than 1 for varied SCR scenarios. This indicates a robust stability margin and immunity against the SCR. On the other hand, the vector controls have the minimum singular values of less than 1. When the SCR reduces, the minimum singular value also reduces, which

indicates that the vector controls are prone to instability when the grid is weak. The singular value plots indicate that the resonance frequency in the dq reference frame is 60 Hz for PSC.

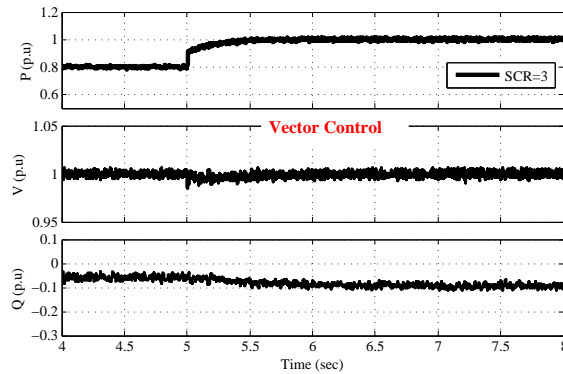


Figure 6.9. Simulation results for step change in real power when vector control is applied and SCR is 3.

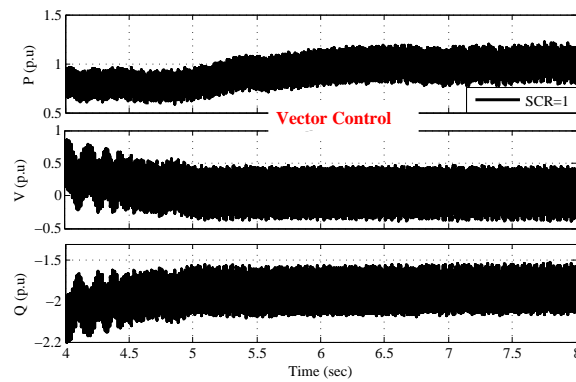


Figure 6.10. Simulation results for step change in real power when vector control is applied and SCR is 1.

Simulation results for vector control (with outer loop) are shown in Fig. 6.9 and Fig. 6.10. For simplicity, only two SCR values are included. The vector current control regulates the active power from the grid to the converter and the terminal voltage in the rectifier station. The step reference power change is applied to change the reference power from 0.8 p.u to 1 p.u at the time 5 sec. It is observed that when the SCR is 3, vector control can follow the reference active power step change. In contrast to the strong system, when the system is weak (SCR is 1), vector control fails to support the power transfer to 0.8 p.u. Results of simulation are in agreement with the stability analysis illustrated in Figs. 6.7 and 6.8.

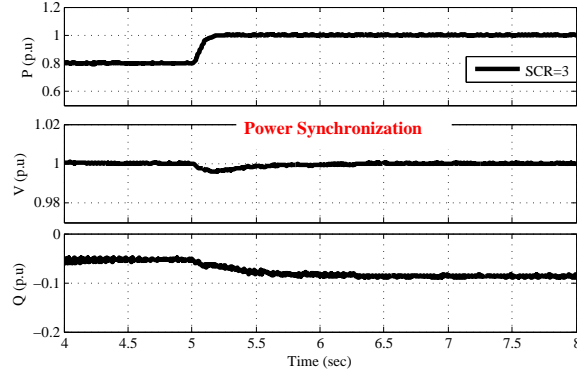


Figure 6.11. Simulation results for step change in real power when PSC is applied and SCR is 3.

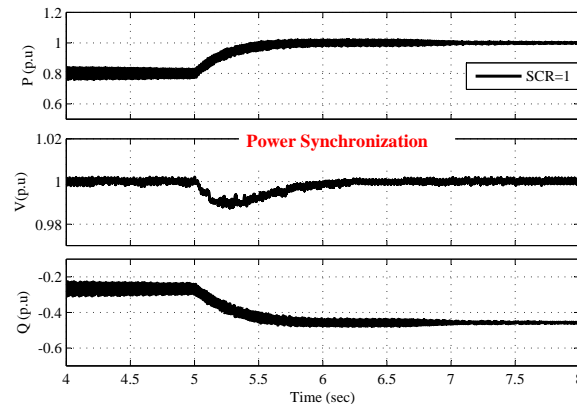


Figure 6.12. Simulation results for step change in real power when PSC is applied and SCR is 1.

Fig. 6.11 and Fig. 6.12 present the simulation results for the PSC for strong and weak AC grid. Same as the previous case, an active power change is applied to change the power transfer from 0.8 p.u to 1 p.u at the time 5 sec. It is shown that for both cases, the system is stable and PSC can successfully transfer the amount of active power which is needed. Compared to the vector control, PSC can transfer 1 p.u even in a very weak ac system connection.

Multiple power transfer levels for three separate controllers are presented in Fig. 6.13. The first figure is for the vector control with simple power loop controller. Compared to the simple power loop controller, the vector control with PI power loop provides a better results for power levels of 80 MW and 100 MW. However, vector control fails to transfer 150 MW in this case. In contrast, PSC can transfer all three active power levels.

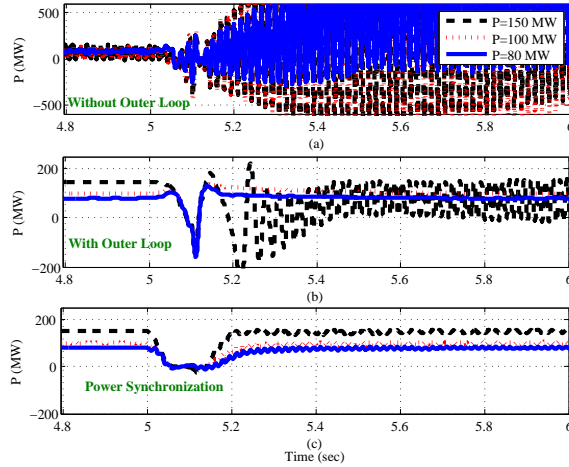


Figure 6.13. Simulation results for different active power levels for three different control approaches; (a): Vector control without outer power loops, (b) Vector control with outer power loops, (c) power synchronization control, a three-phase balanced fault is applied at $t = 5$ s at the inverter AC side and cleared after one cycle, SCR for this case is set to 2.

6.3.4 The Effect of Filter

The effect of a high pass filter is examined in this subsection. The studied filter will move the 60 Hz resonant poles to the left hand plane (LHP) and provides more stability margin to the PSC controller. The results of the root locus (on the open loop transfer function $J_{p\theta} \frac{K_{PSC}}{s}$) comparison for two cases of with and without filter are shown in Fig. 6.14. It is observed that by adding the filter, two resonant 60 Hz poles will move to the left hand side, providing more damping.

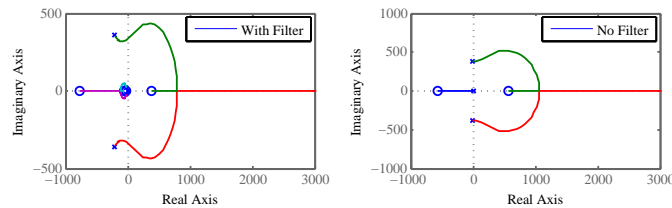


Figure 6.14. Effect of filter on root locus curves of the system when SCR is 1.

The simulation results displayed in Fig. 6.15 validate the analysis results. The system is simulated without a filter at the beginning and then the filter is activated at time 5 seconds. It is observed that after activating the filter, 60 Hz oscillations caused by resonant poles are being damped well.

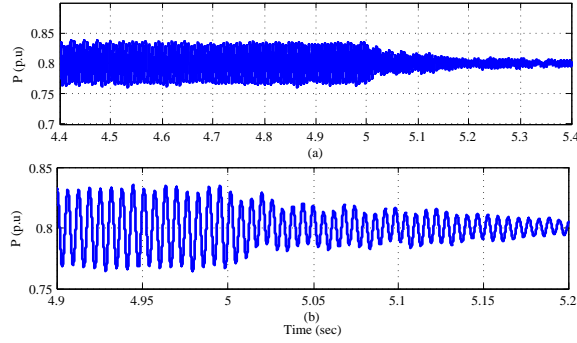


Figure 6.15. Real-time simulation results for the effect of filter when SCR is 1 shown in different scales; (a): effect of filter during the operation, (b): zoom in version of the first subplot.

6.3.5 The Effect of PSC Loop Gain

A high integral PSC gain ensures a fast response. However, high gain can result in an instability. This issue was mentioned in [46] without presenting any analysis and simulation. In this subsection, the root loci of the open loop transfer function (power/angle) are used to indicate the range of K_{PSC} .

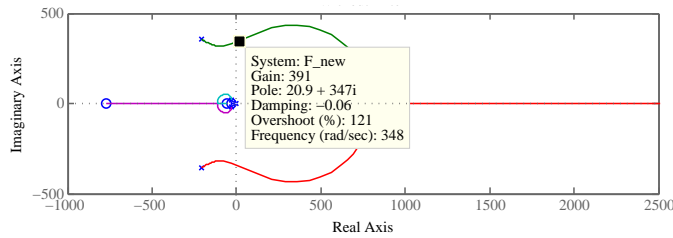


Figure 6.16. Root loci of PSC for SCR equal to 1, with the high pass filter.

Results of root locus analysis of the system with PSC control is illustrated in Fig. 6.16. By increasing the PSC gain to 390, the resonant poles in 60 Hz will move to the right hand side of the s -plane and make the system unstable. Simulation results for different PSC gain loop are presented in Fig. 6.17. When the PSC loop gain is set to 390, large oscillations are observed and power commands can not be followed. However, with a gain as low as 50, the system will be stable.

The developed impedance model is also used to investigate the filter and a high PSC gain effects. Fig. 6.18 shows the effect of filter and high gain on singular value plots. The findings verify that presence of a high pass filter helps to improve the minimum singular value. On the other hand,

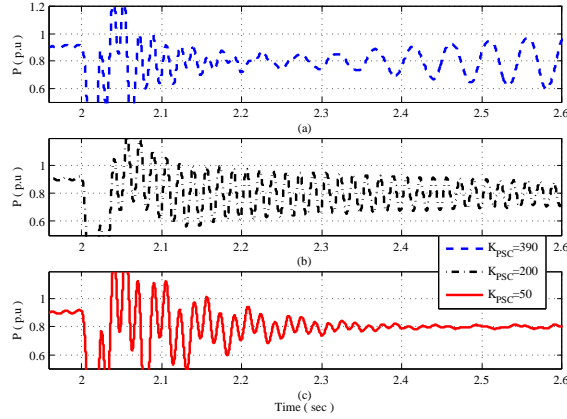


Figure 6.17. Real-time simulation results for different PSC gain loops when the SCR=1; (a): PSC loop gain is 390, (b): PSC loop gain is 200, (c) PSC loop gain is 50.

when the gain is increased from 50 to 200, the minimum singular value becomes less than 1. The MIMO system analysis results corroborate with the analysis results drawn from the power/angle transfer function analysis and the simulation.

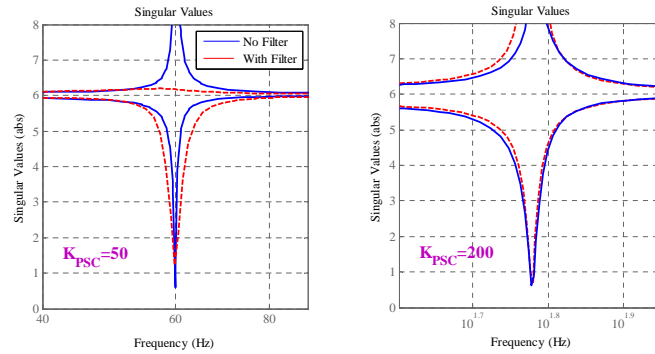


Figure 6.18. Effect of filter and high gain PSC.

6.4 Discussions

The stability analysis of the VSC-HVDC system connected to very weak AC grid is presented in this study. Three different controls for VSC are considered including a power synchronization control, a vector control with PI outer power loops, and a vector control with simple power loops. The impedance based analysis intends to derive the converter input impedance considering the detailed controllers for each control. The derived impedance model is then combined with the grid

impedance to investigate the interactions between the converter and the weak AC grid. MIMO system analysis is utilized to evaluate the system stability under several control strategies and operating conditions. The case studies show that the PSC is capable of providing better stability when connected to a weak grid. PSC can handle higher power transfers compared to the vector controlled methods. Moreover, the 60 Hz resonance stability of PSC is greatly improved by a high pass filter. However, high PSC gain loop will result in the system instability. The overall results of the simulation and analysis demonstrate the superior performance of the PSC when the AC grid is weak.

CHAPTER 7

DYNAMIC PHASOR MODELING FOR UNBALANCED MICROGRIDS

This chapter ¹ investigates dynamic phasor modeling technique for microgrids with PV penetration in unbalanced conditions.

7.1 Introduction

Governmental laws and economical countermeasures have limited the implementation of fossil fuels and inspired the application of renewable energy generation. Among multiple available renewable energy generation units, PV energy generation has become an extensively grown renewable energy alternative during the past decade. The total installed grid connected PV capacity was 300 MW in 2000 which was increased to 21 GW in 2010 [49]. More recently, PV system has been employed as a major source in microgrids to supply loads [50, 51, 52].

Among many types of PV systems, a grid connected single phase PV has the advantages of a good tradeoff between the extracted energy and the design complexity of power inverters. Furthermore, the reduced cost of PV have extensively improved its application in the grids. However, a high installation number of single-phase PV will impose technological challenges to the microgrids associated with: harmonics and power quality, reliability of entire system, voltage rise, and inaccurate energy and demand metering [53, 54].

In [53], it has been mentioned that in the near future, there will be more operating points and functions provided by single phase PVs during the grid faults. As a result, special care should be taken into account in regulating the single-phase PV in microgrids in order to avoid the power quality and propagating harmonics issues. The effect of unbalance caused by harmonic currents

¹This chapter was published in IEEE Transactions on Power Systems, vol.30, no.6, pp. 3102-3109, Nov. 2015. Permission is included in Appendix B.

injected by single-phase PV into microgrids are not comprehensively investigated. Moreover, there is no proper management algorithm for selecting the parameters for various microgrid elements to lay the foundation of how each individual component can cause instability in the system, or which component is highly prone to produce resonances in microgrids.

As a result, the main goal of this chapter is to model the microgrid in presence of a single phase PV system, and clarify the effect of various components on overall stability of the system. The overall stability of a system is guaranteed when the voltage and the frequency fluctuations remain within acceptable limits. To achieve this point, the dynamic analysis of microgrid can be assessed. Among various methods of dynamic analysis, Dynamic Phasor (DP) analysis offers abundant merits compared to the traditional methods [55, 56, 57, 125]. The DP will change slightly when there is a sudden change in instantaneous quantities, consequently, fast simulations with a larger time step will be provided which enables incorporating the frequency information. Furthermore, the dynamical couplings which cannot be identified from the outset, are obtained through the DP modeling. One major benefit of the DP method in comparison with the other approaches is that it has steady values even under unbalanced conditions. However, in the dq modeling, one can see a 120 Hz oscillating components in case of unbalanced conditions.

The literature needs a comprehensive radial system model which is appropriate for the small-signal analysis or nonlinear time-domain simulations for balanced and unbalanced situations.

This research investigates the DP modeling of an unbalanced microgrid including a single phase PV system ², an induction machine, a power factor correction capacitor, and transmission lines. It has to be noted that, the unbalance polyphase DP model is considered for the induction machine. Moreover, a detailed PV modeling including an LCL filter, a PR controller, and a PLL have been adopted. Several case studies have been conducted to examine the effect of different parameters of the microgrid (LCL filter, PR controller gains, line length, and induction machine length) in overall stability of the system. Small signal analysis based on linearizing the state equations and dynamic simulations have been investigated in MATLAB®/Simpowersystem toolbox in order to verify the results.

²This part was published in Power & Energy General Meeting, July. 2015, IEEE, pp. 1-5 (best paper in simulation studies). Permission is included in Appendix B.

7.2 Methodology

7.2.1 DP Approach

DP model provides many benefits compared to the traditional approaches of power system analysis. For instance, DP changes smoothly if there is a sudden large step change in the input. In addition, DP can reveal the dynamic coupling, which is not visible from the outset [55]. DP comes from the Fourier series of time variable signal $x(\tau)$ on interval $[t - T, t]$:

$$x(\tau) = \sum_{k=-\infty}^{\infty} X_k(t) e^{jk\omega_s t} \quad (7.1)$$

where $\omega_s = 2\pi/T$ and X_k is the k^{th} complex Fourier coefficient or k^{th} DP. Small signal analysis can be implemented for these coefficients (dynamic phasors), as they vary slightly with time or they are constant during the operation. Therefore, the k^{th} dynamic phasor coefficient of the time varying signal $x(\tau)$ can be attained by [57]:

$$X_k(t) = \frac{1}{T} \int_{t-T}^t x(\tau) e^{-jk\omega_s \tau} d\tau = \langle x \rangle_k(t) \quad (7.2)$$

The value of k that defines the order of dynamic phasor should be selected in a way that leads to a proper approximation of the original signal. For example, in unbalanced conditions, since there is a 120 Hz oscillating mode in induction machines, a second order DP should be considered as well as the first order DP. The main characteristics of DP can be expressed as [57]:

$$\left\langle \frac{dx}{dt} \right\rangle_k = \frac{dX_k}{dt} + jk\omega X_k \quad (7.3)$$

$$\langle x.y \rangle_k = \sum_{l=-\infty}^{\infty} (X_{k-l} \cdot Y_l) \quad (7.4)$$

Equation (7.3) is used when the small signal model of the system contains a capacitor, or an inductor. The capacitor voltage or the inductor current can be represented as a time derivative of capacitor current or inductor voltage which can be transformed to DP by equation (7.3). In

this study, the main goal is to derive the DP model of a microgrid composed of a single-phase PV, a three-phase induction machine, a Power Factor Correction (PFC) unit, and transmission lines. As the system is unbalanced, some components of the system such as induction machines should be modeled in the unbalanced condition mode. In this case, the positive, negative and zero (pnz) reference frame can be used. The DP modeling in unbalanced three-phase systems can be derived by converting the abc reference frame to pnz reference frame [55]. The main equation to convert an abc reference frame variable to pnz reference frame is represented by:

$$\begin{bmatrix} x_a \\ x_b \\ x_c \end{bmatrix} (\tau) = \sum_{l=-\infty}^{\infty} e^{jk\omega_s\tau} \underbrace{\frac{1}{\sqrt{3}} \begin{pmatrix} 1 & 1 & 1 \\ \alpha^* & \alpha & 1 \\ \alpha & \alpha^* & 1 \end{pmatrix}}_T \begin{bmatrix} X_{p,l} \\ X_{n,l} \\ X_{z,l} \end{bmatrix} \quad (7.5)$$

where T is the transformation matrix from abc to pnz reference frame. Similar to the basic definition of DP, the DP coefficients are derived by:

$$\begin{bmatrix} X_{p,l} \\ X_{n,l} \\ X_{z,l} \end{bmatrix} (t) = \frac{1}{T} \int_{t-T}^t A^H e^{-jl\omega_s\tau} \begin{bmatrix} x_a \\ x_b \\ x_c \end{bmatrix} (\tau) d\tau \quad (7.6)$$

It is worth mentioning that $X_{p,l}$, $X_{n,l}$ and $X_{z,l}$ are dynamic phasors in positive, negative and zero-sequence reference frame at the $l\omega_s$ frequency. Moreover, H denotes the complex conjugate transpose. The next important step to convert the abc reference to pnz would be the derivative of the time domain signal based on DP condiments on pnz reference frame [55]:

$$\frac{d}{dt} \begin{bmatrix} X_{p,l} \\ X_{n,l} \\ X_{z,l} \end{bmatrix} (t) = A^H \begin{bmatrix} \langle \frac{dx_a(t)}{dt} \rangle_l \\ \langle \frac{dx_b(t)}{dt} \rangle_l \\ \langle \frac{dx_c(t)}{dt} \rangle_l \end{bmatrix} - jl\omega_s \begin{bmatrix} X_{p,l} \\ X_{n,l} \\ X_{z,l} \end{bmatrix} (t) \quad (7.7)$$

The above set of equations can be used in order to find the symmetric components in a periodic steady state condition and single phase cases. Same as the abc frame for symmetrical components, a close approximation of the original signal can be achieved by an appropriate selection of the DP order k .

7.2.2 Microgrid Configuration

The system under investigation is an unbalanced microgrid composed of a single-phase PV, an induction machine, a PFC unit and loads as shown in Fig. 7.1. The single-phase PV is installed in phase a of the system to make the system unbalanced, and the 3-phase induction machine, a 3-phase PFC, and the 3-phase loads are in balanced condition.

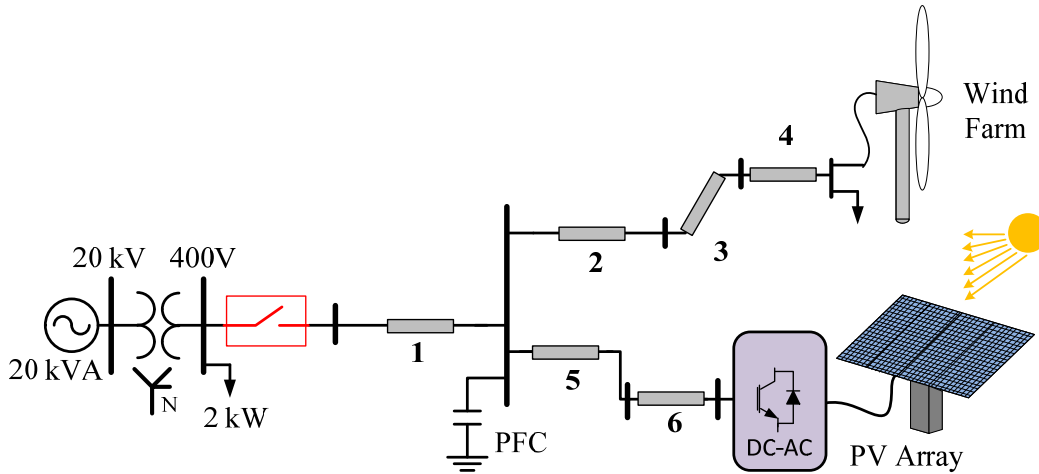


Figure 7.1. The study system; unbalanced microgrid.

Step by step derivation of dynamic phasors for each component of the microgrid is included below.

7.2.3 The DP Model of a Single-Phase PV

Traditionally, two-stage converters (a DC-AC converter after a DC-DC converter) have been used for PV systems. Two-stage converters need additional devices compared to the single-stage converters. Moreover, the DC-DC converters have high losses, unfavorable transient response, and unbelievable maintenance cost. Thus, the single-stage converter has been introduced in this chapter which provides lower price and easier implementation. Single-stage converters have been installed in the PV/grid integration [126, 127, 53, 54]. The basic configuration of a single phase PV is illustrated in Fig 7.2. The key components of the single-stage PV are the PR, the PLL, and the output filters.

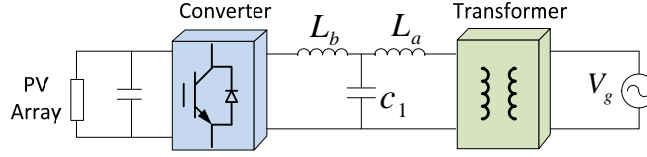


Figure 7.2. A basic configuration of PV system.

Fig. 7.2 shows a simple configuration of a single phase PV system. It has an LCL filter to seize the switching harmonics, and a transformer to isolate the PV from the grid. This figure can be even more simplified. Depending on the operation, different filter combinations can be used; L and LCL are two forms of those filters. The more simplified PV model with L and LCL filters is displayed in Fig. 7.3; where v_{con} is the output voltage of the converter, and L_a and L_b are filter inductances. The grid side voltage is v_G . Because the PV can be modeled as voltage source V_{Con} in series with an inductance L_{Con} , simplification from Fig. 7.2 to Fig. 7.3 is valid. In addition, the transformer can be modeled as an inductance X_T . Therefore, the relationship between L_a , L_b , L_1 , and L_2 for the PV model with LCL filter can be recognized as: $L_2 = L_b + L_{Con}$ and $L_1 = L_a + L_T$. Additionally, for a PV connected to the L filter, if L_f is used for the L filter inductance, the deduction process is summarized to $L_3 = L_f + L_{Con} + L_T$.

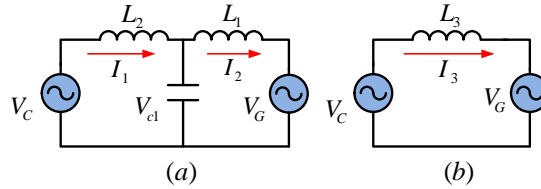


Figure 7.3. Simplified PV model with different combinations; (a) LCL filter, (b) L filter

For the goals of this dissertation, an LCL filter has been considered, which is the mostly used type of filter in PV applications. Applying the simple Kirchhoff's Voltage Law (KVL) and Kirch-

hoff's Current Law (KCL), time domain equations of the system for the LCL filter can be derived:

$$\begin{aligned}
 L_1 \frac{di_1}{dt} &= (v_{c1} - v_G) \\
 L_2 \frac{di_2}{dt} &= (v_{con} - v_{c1}) \\
 C_1 \frac{dv_{c1}}{dt} &= (i_2 - i_1)
 \end{aligned} \tag{7.8}$$

Considering only the first harmonic for the PV, and applying DP laws into the above equations, the DP model of the PV system with the LCL filter is expressed as follows:

$$\begin{aligned}
 \dot{I}_1 &= \frac{1}{L_1} (V_{c1} - V_G) - j\omega_s I_1 \\
 \dot{I}_2 &= \frac{1}{L_2} (V_{con} - V_{c1}) - j\omega_s I_2 \\
 \dot{V}_{c1} &= \frac{1}{C_1} (I_2 - I_1) - j\omega_s V_{c1}
 \end{aligned} \tag{7.9}$$

It should be noted that V_{con} is the DP of the output voltage of the PV controller. A detailed control block diagram of the single-stage single phase PV is shown in Fig 7.4 including a MPPT, a PR, a PLL and a pulse generation unit. As the main purpose is to study the effect of PV unbalance on the entire microgrid, dynamics of MPPT and PLL can be neglected.

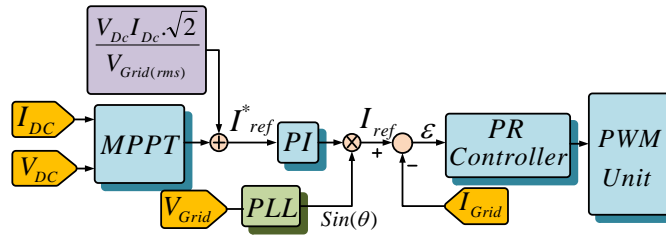


Figure 7.4. Basic control of a single-phase PV.

7.2.4 DP Model of a PR Controller

PR control is used to track AC signals. The PR controller in Fig 7.4 tries to provide unity power factor from the PV. Hence, the current reference is synchronized with the grid voltage

through a PLL. The dynamics of a PR controller considering only the fundamental harmonics can be expressed as:

$$\begin{aligned} v_{con} &= \left(K_p + \frac{K_r s}{s^2 + (\omega_0)^2} \right) (i^* - i_1) \\ &= \left[K_p + K_r \left(\frac{0.5}{s + j\omega_0} + \frac{0.5}{s - j\omega_0} \right) \right] (i^* - i_1) \end{aligned} \quad (7.10)$$

where i^* is the reference current originated from the PV array.

In equation (7.10), i_1 is the grid current when the PV is linked to the LCL filter. By defining the intermediate state variables of x_1 and x_2 :

$$\begin{aligned} (s + j\omega_0)x_1 &= 0.5(i^* - i_1), \\ (s - j\omega_0)x_2 &= 0.5(i^* - i_1). \end{aligned} \quad (7.11)$$

Using DP concept in the above equation will result in equation (7.12).

$$\begin{aligned} \dot{X}_1 &= 0.5(I^* - I_1) - 2\omega_0 X_1 \\ \dot{X}_2 &= 0.5(I^* - I_1) \end{aligned} \quad (7.12)$$

So, the DP of the fundamental frequency component of the converter output voltage can be expressed as:

$$V_{con} = K_{p1}(I^* - I_1) + K_{r1}(X_1 + X_2) \quad (7.13)$$

Taking $I^* = \frac{\sqrt{2}V_{dc}I_{dc}}{V_G(rms)} = \frac{\sqrt{2}P_{ref}}{V_G(rms)}$ into account, the DP model of a single-phase PV consisting of (7.9), (7.12) and (7.13) can be derived.

7.2.5 Induction Machine Model in Dynamic Phasors

Single phase PV will generate unbalance in microgrids, and thus the induction machine model should reflect these unbalanced conditions. Negative sequence components in the stator voltage can cause a clockwise rotating stator flux. In this situation, such flux interacts with the clockwise

rotating rotor flux, until a 120 Hz torque ripple will appear. Accordingly, the rotating speed will have a 120 Hz ripple. To count in the negative effect, this chapter adopted the three-phase induction machine in [55] based on pnz -sequence components. The space vector model of a squirrel cage induction machine with magnetic saturation and slot harmonics neglected is presented as follows.

$$\begin{aligned}
\vec{v}_s &= (r_s + L_s \frac{d}{dt})\vec{i}_s + L_m \frac{d}{dt}\vec{i}_r \\
0 &= L_m \frac{d}{dt}\vec{i}_s + (r_r + L_r \frac{d}{dt})\vec{i}_r - j\omega_r \frac{P}{2}(L_m \vec{i}_s + L_r \vec{i}_r) \\
J \frac{d}{dt}\omega_r &= \frac{3P}{4}L_m \Im(\vec{i}_s \vec{i}_r^*) - B\omega_r - T_L
\end{aligned} \tag{7.14}$$

where $\vec{v}_s, \vec{i}_s, \vec{i}_r$ denote the stator voltage, the stator current and the rotor current respectively. T_L is the mechanical torque and ω_r is the rotor speed. s and r denote the stator and rotor quantities, respectively. \Im denotes the imaginary part. The DP model of an induction machine can be derived by considering the positive- and negative-sequence components in stator/rotor voltages and currents, as well as the DC and the 120 Hz components in the rotating speed [55].

$$\begin{aligned}
V_{ps} &= (r_s + j\omega_s L_s + L_s \frac{d}{dt})I_{ps} + (j\omega_s L_m + L_m \frac{d}{dt})I_{pr} \\
0 &= (j\omega_s L_m + L_m \frac{d}{dt})I_{ps} + (r_r + j\omega_s L_r + L_r \frac{d}{dt})I_{pr} - j\omega_{r0} \frac{P}{2}(L_m I_{ps} + L_r I_{pr}) - j\omega_{r2} \frac{P}{2}(L_m I_{ns}^* \\
&\quad + L_r I_{nr}^*) \\
V_{ns}^* &= (r_s - j\omega_s L_s + L_s \frac{d}{dt})I_{ns}^* - (j\omega_s L_m - L_m \frac{d}{dt})I_{nr}^* \\
0 &= (L_m \frac{d}{dt} - j\omega_s L_m)I_{ns}^* + (r_r - j\omega_s L_r + L_r \frac{d}{dt})I_{nr}^* - j\omega_{r0} \frac{P}{2}(L_m I_{ns}^* + L_r I_{nr}^*) - j\omega_{r2}^* \frac{P}{2}(L_m I_{ps} \\
&\quad + L_r I_{pr}) \\
J \frac{d}{dt}\omega_{r0} &= \frac{2P}{4}L_m \Im(I_{ps} I_{pr}^* + I_{ns}^* I_{nr}) - B\omega_{r0} - T_L \\
J \frac{d}{dt}\omega_{r2} &= \frac{2P}{j8}L_m \Im(I_{ps} I_{nr} - I_{ns} I_{pr}) - (B + j2J\omega_s)\omega_{r2}
\end{aligned} \tag{7.15}$$

where subscripts p and n stand for positive and negative sequence components, respectively.

As the dynamic phasor model of the PV is derived for only phase a, this model should be integrated with an induction machine, modeled in the pnz reference frame. Therefore, the above pnz model will be converted to the abc frame using the relationship presented in (7.5). The block diagram of the conversion is illustrated in Fig 7.5.

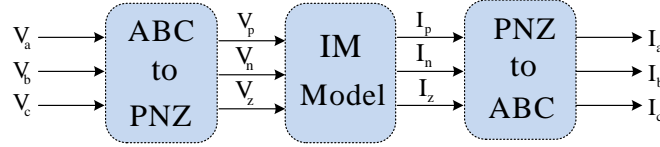


Figure 7.5. Conversion from abc to pnz and back to abc for an induction machine.

7.2.6 Integrated Microgrid Model in Dynamic Phasor

Assuming that there is a three-phase PFC unit in parallel with the PV, the circuit model of the microgrid can be displayed as in Fig 7.6, where C denotes the capacitance of the PFC, I_M

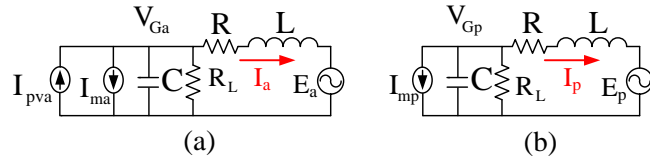


Figure 7.6. (a) Model of microgrid with PV in phase a , (b) model of microgrid in phase b and c

is the induction machine's stator current, I is the line current, R and L are the distribution line parameters, R_L is the load model, and E is the system voltage.

For phase a, as the PV is installed in this phase, the DP model of the integrated system can be expressed as:

$$\begin{aligned} \frac{d}{dt} I_a &= \frac{1}{L} (-(j\omega L + R)I_a + V_{Ga} - E_a) \\ \frac{d}{dt} V_{Ga} &= \frac{1}{C} (-(j\omega C + \frac{1}{R_L})V_{Ga} + I_{ma} + I_{PV} - I_a) \end{aligned} \quad (7.16)$$

There is no PV installed for phases b and c. The DP model of the integrated system can be expressed as:

$$\begin{aligned}\frac{d}{dt}I_p &= \frac{1}{L}(-j\omega L + R)I_p + V_{Gp} - E_p \\ \frac{d}{dt}V_{Gp} &= \frac{1}{C}(-j\omega C + \frac{1}{R_L})V_{Gp} + I_{mp} - I_p\end{aligned}\quad (7.17)$$

where p represents either phase b or phase c.

The entire system is composed of a PV system, an induction machine, a PFC unit, a load, and an RL line. As a total, 17 complex state variables are presented, including the line currents (I_{abc}), the PFC voltage ($V_{G,abc}$), the induction machine stator currents ($I_{s,pn}$), the induction machine rotor currents ($I_{r,pn}$), the induction machine rotor speed (ω_{r0}, ω_{r2}), the PV system state variables (output current (I_1), the current before the filter (I_2), the voltage across the LCL filter capacitor (V_{c1}), and the stator variables in the PR controller (X_1 and X_2). The complex state variables will be separated into real and imaginary components. As a result, 34 real state variables are introduced for this DP model and small-signal analysis will show 34 eigenvalues.

7.3 Results

7.3.1 Case Studies

In the previous section, the analytical model for the entire microgrid system was demonstrated. The state space model is constructed in MATLAB®/Simulink for eigenvalue analysis. The nonlinear analytical model can be linearized based on a certain operating point using MATLAB® function “linmod”. Eigenvalue analysis can then be carried out for the linearized model. To validate the results of analytical model, a time domain detailed model was also built in MATLAB®/SimPowerSystems based on the physical circuit connection.

The MATLAB®/SimPowerSystem model captures power electronic switching details and hence includes a high-fidelity simulation model. Parameters of the system are listed in Table A.12, Table A.13 and Table A.14 of Appendix A.

Three case studies have been carried out.

- In the first case, an analytical model in Simulink is benchmarked with the high-fidelity model in SimPowerSystem toolbox. The dynamic simulation results are compared for the same dynamic event, i.e. a step change in load torque of the induction machine.
- In the second case, the effect of unbalance on the dynamic performance is investigated by applying a ramp change in irradiance of the PV. This dynamic event emulates the cloud effect on a PV and a distribution system.
- In the third case, the effect of a grid line length on stability is investigated. Eigenvalue analysis and dynamic simulation are carried out.

7.3.1.1 Case Study 1

A single-phase PV is connected to the phase *a* of the system at the PCC as shown in Fig.7.1. At $t = 4s$, the induction machine's mechanical torque faces a step change from 28 N.M to 23 N.M.

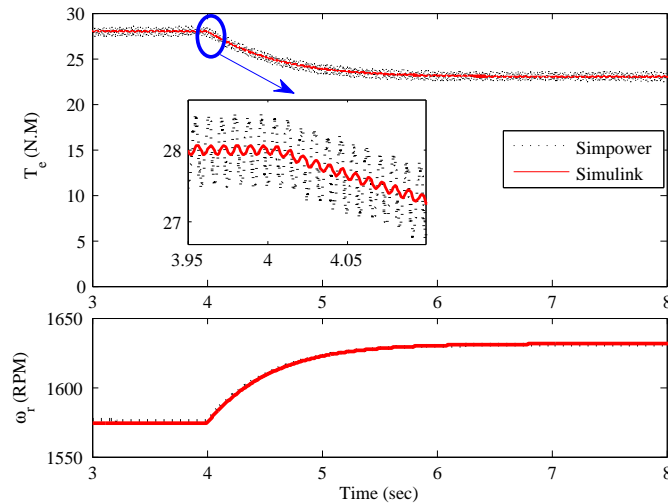


Figure 7.7. Simulation results of torque and rotor speed due to a step change in mechanical torque (from 28 N.M to 23 N.M).

The simulation results of the electromagnetic torque and the rotor speed of the induction machine have been illustrated in Fig. 7.7, showing the comparison between an analytical model and a detailed simulation for an electromechanical torque change. As the figure shows, both responses match and could respond to the step change quickly.

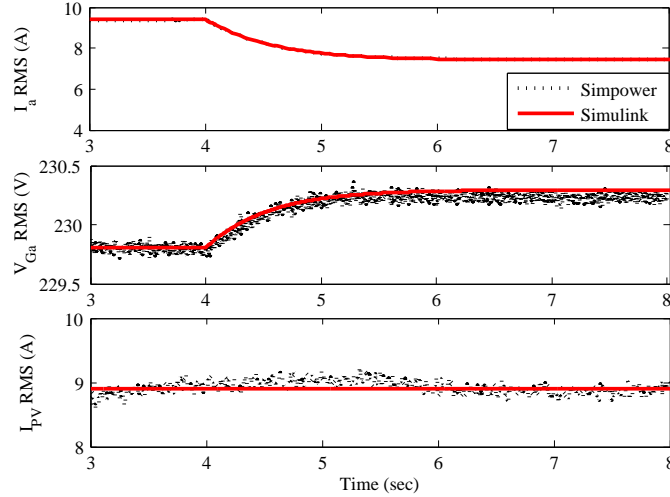


Figure 7.8. Simulation results of the IM stator current, stator voltage and PV current due to a step change in mechanical torque (from 28 N.M to 23 N.M).

The simulation results for the line current, the line voltage, and the PV current are presented in Fig. 7.8. The line current and line voltage simulation results from both models match well, which demonstrates the accuracy of the analytical model derived in this chapter. The PV current from the Simpowersystems simulation has the dynamics related to the MPPT control and the DC side capacitor, neglected in the analytical model. In the analytical model, V_G contains only a negligible variation, which will result in a constant PV current.

7.3.1.2 Case Study 2

Eigenvalue analysis for the system with and without PV has been conducted and the results are presented in Table 7.1 and Table 7.2. It can be observed from the tables that, due to the introduction of the PV, five pairs of eigenvalues are introduced and these eigenvalues are related to PV state variables such as the LCL capacitor voltage V_{c1} , PR controller state variables X_1 , X_2 , and the PV current I_{PV} .

In this part, a ramp change is applied at the time 4 seconds in order to change the irradiance from $1000 \text{ W}/\text{M}^2$ to $200 \text{ W}/\text{M}^2$ within 0.2 sec. After 5.4 sec, the irradiance will be set back to $1000 \text{ W}/\text{M}^2$. The change of the irradiance is illustrated in detail in the Fig. 7.9.

Table 7.1. Eigenvalues of the system without PV

Eigenvalue	damping ratio %	frequency(Hz)	dominant state
$\left\{ \begin{array}{l} -959 \pm 5768i \\ -966 \pm 5935i \\ -966 \pm 5935i \\ -959 \pm 5014i \\ -966 \pm 5181i \\ -966 \pm 5181i \end{array} \right\}$	$\left\{ \begin{array}{l} 16.4 \\ 16.07 \\ 16.06 \\ 18.78 \\ 18.33 \\ 18.33 \end{array} \right\}$	$\left\{ \begin{array}{l} 918 \\ 945 \\ 945 \\ 798 \\ 825 \\ 825 \end{array} \right\}$	V_G, I
$-133.37 \pm 308i$	39.68	49	I_{ps}
$-137.95 \pm 117i$	76.37	18.6	I_{pr}
$-133.38 \pm 445i$	28.69	70.9	I_{ns}
$-137.95 \pm 637i$	21.15	101	I_{nr}
-0.76 ± 754	0.1	120	ω_{r2}
$-1.54 \pm 0i$	100	0	ω_r

Table 7.2. Eigenvalues of the system with PV

Eigenvalue	damping ratio %	frequency(Hz)	dominant state
$\left\{ \begin{array}{l} -966 \pm 5935i \\ -967 \pm 5848i \\ -993 \pm 5607i \\ -993 \pm 4853i \\ -966 \pm 5181i \\ -967 \pm 5094i \end{array} \right\}$	$\left\{ \begin{array}{l} 16.06 \\ 16.31 \\ 17.43 \\ 20.04 \\ 18.33 \\ 18.65 \end{array} \right\}$	$\left\{ \begin{array}{l} 944 \\ 931 \\ 892 \\ 772 \\ 824 \\ 810 \end{array} \right\}$	V_G, I
$\left\{ \begin{array}{l} -855 \pm 8475i \\ -855 \pm 7721i \end{array} \right\}$	$\left\{ \begin{array}{l} 10.04 \\ 11.01 \end{array} \right\}$	$\left\{ \begin{array}{l} 1349 \\ 1229 \end{array} \right\}$	V_{c1}
$\left\{ \begin{array}{l} -1.87 \pm 754i \\ -1.87 \pm 0.10i \end{array} \right\}$	$\left\{ \begin{array}{l} 0.25 \\ 99.8 \end{array} \right\}$	$\left\{ \begin{array}{l} 120 \\ 0.02 \end{array} \right\}$	X_1, X_2
$-8218 \pm 377i$	99.9	60	I_{pv}
$-133.37 \pm 308i$	39.68	49	I_{ps}
$-137.96 \pm 117i$	76.23	18.6	I_{pr}
$-133.37 \pm 445i$	28.68	70.9	I_{ns}
$-137.96 \pm 637i$	21.17	101	I_{nr}
-0.75 ± 754	0.1	120	ω_{r2}
$-1.52 \pm 0i$	100	0	ω_r

The PV power in Fig. 7.9 shows that the PV can greatly follow the irradiance command. It is noticed that the maximum power level of 2 kW is obtained when the irradiance is set to 1000 W/M^2 . The third figure shows the electrical torque of the induction machine. When the irradiance is decreased due to climate change, the PV power is decreased, which decreases the unbalance injection level by PV to the system. The magnitude of the 120 Hz ripple has been decreased during the time interval of 4 to 6 seconds. The last figure shows that the PV current decreased due the irradiance change.

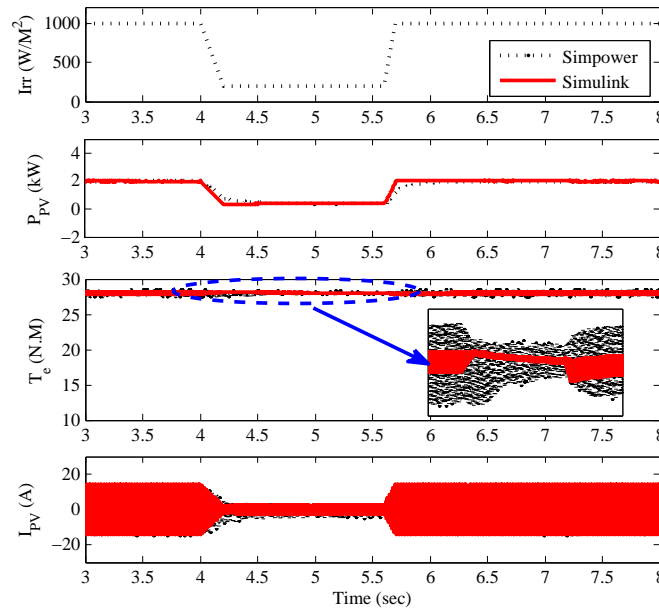


Figure 7.9. Simulation results for the effect of irradiance change.

7.3.1.3 Case Study 3

In case 3, the impact of the line length on the system stability has been investigated by both eigenvalue analysis and time-domain simulation in MATLAB®/Simpowersystems. The root loci plot of the dominant eigenvalue is presented in Fig. 7.10. The grid line length has been changed from 3 km to 15 km in order to make the AC system weaker. Such change is highly favorable when a microgrid is located far away from the main grid. For analytical model, increasing the line length to more than 15 km causes the eigenvalue analysis and linearization process to fail. The results are

only shown for the initial conditions where the system is still able to converge. Fig. 7.10 indicates that as the line length increases, the dominant eigenvalue will move to the right half plane, causing a voltage instability in the system.

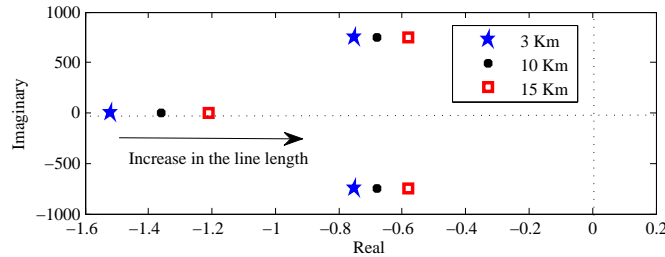


Figure 7.10. The dominant modes (120 Hz, and the voltage stability mode) by increasing the line length.

In order to observe the performance of the detailed model in time-domain simulations, a dynamic event is set to increase the grid line from 3 km to 30 km at the time 4 seconds. Initially, the grid connection consists of two parallel lines. At $t = 4s$, one line will trip and the total impedance of the system will be increased. Such event causes the voltage stability mode to move to the right half plane (RHP). As a result, the stator voltage of the induction machine decreases significantly as shown in Fig. 7.11.

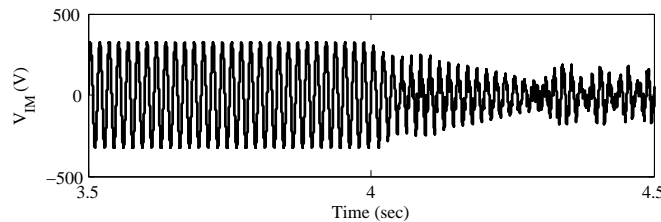


Figure 7.11. Stator voltage when the grid line length increases from 3 km to 30 km; simulation results are produced by Matlab/SimPowerSystems.

Fig. 7.12 presents the dynamic response of the RMS value of stator voltage from 3.5 seconds to 6 seconds, which clearly shows the decline of the voltage magnitude.

Due to the decrease of the stator voltage and system voltage magnitude, the electromagnetic torque in the induction machine will decrease and consequently the rotor speed will decrease as shown in Fig. 7.13 (a) and (b). For the PV, since the reference power is kept constant, the reference

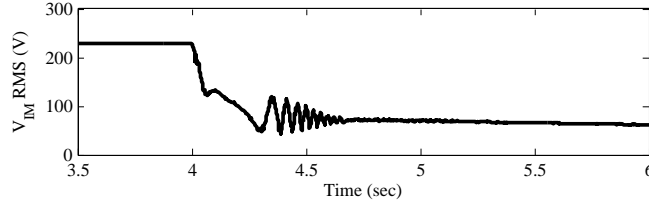


Figure 7.12. RMS stator voltage when the grid line length increases from 3 km to 30 km.

current increases due to the voltage dip. Hence, the PV current's magnitude increases as shown in Fig. 7.13. The entire system becomes unstable.

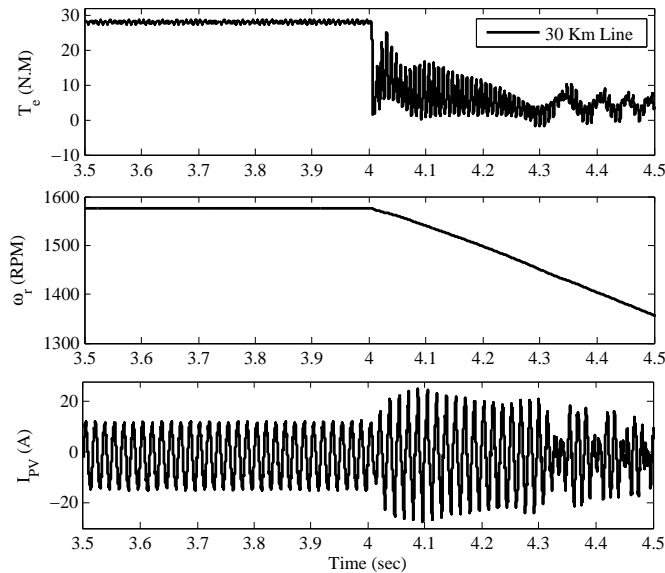


Figure 7.13. Simpowersystems simulation results for the effect of grid line length increase; (a) torque (b) rotating speed (c) instantaneous current from PV.

7.4 Discussions

In this chapter, the detailed dynamic modeling of the grid connected microgrids in an unbalanced condition is investigated. The unbalance comes from the single-phase PV system connected to phase a of the system. The modeling part has been conducted based on the DP model of each component with their controllers. For the DP modeling of the induction generator, the pnz based dynamic phasor has been considered. Detailed modeling of single phase PV is derived for an LCL filter, a PR

controller and a single phase PLL. Moreover, the DP modeling of transmission line and power factor correction unit are included in the final model. The aggregated model is used to verify the effect of the single phase PV on the system stability based on eigenvalue analysis and Simpowersystem simulations. Three different case studies have been discussed. Firstly, the effect of the PV on stability is studied, then the effect of an induction machine on stability is considered, and finally, the effect of the grid line length is simulated. It is concluded that different parameters of the PV can cause an instability such as the LCL filter and gains of the PR controller. Special care should be taken into account when trying to tune these parameters. Moreover, the effect of induction machine in stability of the system is investigated through changing the induction machine's line length. It has been derived that the shorter the induction machine line length, the more stable the system. Finally, the third case study reveals that with increasing the line length, the system is more prone to instability.

CHAPTER 8

CONCLUSIONS

8.1 Results

In this chapter, results of the analysis and simulations derived in each chapter will be included in detail.

Chapter 2 presents the basic foundation of upper level and lower level controls in microgrids. In the lower level control, a primary controller, which can be a voltage/frequency/power controller, is supplemented to the pulse generation unit of the DER converter. If there are more than one DER units in the microgrid, primary droop controllers are developed. The upper level controller is the high level control in charge of the voltage/frequency restoration, or synchronization and optimization of multiple DERs. There are two approaches for the upper level control; centralized controllers and decentralized/distributed controllers. Centralized upper level controllers need one way communication and they send a unified control signal to primary controllers of DERs. In case of a failure in centralized controllers, the entire synchronization of the secondary controller fails. Distributed or decentralized controllers are the upper level controllers with two way communications between DERs, but with the limited information exchange. This type of control, which is the main focus of this dissertation, will improve the reliability and performance of the secondary controllers in microgrids.

Chapter 2 also introduces the main concept behind the distributed control implementation, which is the consensus theory. Consensus theory is an advanced control theory applied for synchronization between multiple agents with limited information exchange among the agents. The last part of the chapter 2 presents two analysis approaches for microgrids. The first method is

the impedance analysis for interactions between converters and the grid and the second one is the dynamic phasor for unbalanced microgrids.

Chapter 3 investigates the application of the lower level control in single phase PV systems. The studied single phase PV model is built in real time simulators. As real-time simulators work with discrete domain models, the continuous single phase PV model presented in the literature is converted to the discrete time domain. A new design is introduced to enhance the efficiency of the MPPT controller in the single phase PV. The findings verify that the proposed design can greatly remove the large spikes in the maximum power tracking controller output and improve the efficiency.

Chapter 4 demonstrates the application of the lower level control in offshore wind farms based on multi-terminal HVDC transmission lines. The main objective is to minimize the losses by designing adaptive droop controllers at inverter stations. Because HVDC has two energy conversion processes of 1) AC to DC, i.e. the rectifier station, in offshore and 2) DC to AC, i.e. the inverter station, in onshore, multiple control functions can be achieved. This research proves that if at least one of the rectifier station converters is working at the maximum power, and the droop gains of the inverter station converters are inversely proportional to the DC cable resistances, the minimum loss in the DC system is achieved. The algorithm can work with any operating points and even in case of failures. By tuning the droop gains of the grid side converters, the minimum loss is guaranteed. Moreover, the proposed algorithm will keep the voltage at the both terminals fixed even if faults occur, which is a great achievement.

Chapter 5 discusses the impact of the upper level control in microgrids. In this chapter, distributed/decentralized controller is designed for a microgrid composed of three energy storage devices with limited information exchange between the energy storage systems. Consensus theory is also applied for the decentralized controller design, with the goal of synchronizing the energy levels and powers of energy storage devices in microgrids.

Chapter 6 studies the microgrid modeling with impedance analysis. Impedance analysis is the best tool to evaluate the interactions between a converter and grid. Such interactions may occur when the converter is linked to a weak AC grid. In this case, the vector control of the converter might

fail, which is why in weak AC systems, a power synchronization is employed as an alternative to the vector control. This study adopts the impedance analysis in the MIMO condition with Nyquist stability criterion and singular value analysis in order to compare the vector control and the power synchronization in multiple operating point conditions. Results proves a superior performance of the power synchronization control in very weak AC grid conditions. Time domain simulations are added to support the analysis claims. Various case studies are carried out to compare the power synchronization with the vector control.

Chapter 7 investigates an unbalanced modeling and analysis of a microgrid with dynamic phasors. An unbalanced microgrid composed of a single phase PV and a three phase induction machine with multiple loads is considered. Dynamic phasor is used in order to reflect the unbalance effect in the microgrid. Analytical models are used to find the eigenvalues, and conduct the stability analysis. Moreover, time domain simulations are conducted in order to verify the analytical results. It is concluded that the analytical model built by the dynamic phasor can greatly reflect the dynamic behavior of the detailed model with a much faster response. It is also concluded that increasing the grid line length in a grid connected unbalanced microgrid may result in voltage stability issues.

8.2 Future Work

8.2.1 Lower Level Control

Improvements in the lower level control can be validated through experimental results. Chapter 3 has shown that the new MPPT algorithm for the PV system will improve the efficiency of the PV controller. An experimental setup can verify the claims with micro inverters and PV array emulators.

8.2.2 Upper Level Control

The distributed control design in this thesis was based on consensus theory for homogeneous systems. It means, in the case study presented in chapter 4, all the energy storage devices were the same, and shared the same dynamics. However, if multiple DERs are present, the dynamics of those DERs would be different. In this case, heterogeneous consensus theory should be applied. More

research is anticipated to improve the heterogeneous consensus design procedure for distributed control in microgrids.

8.2.3 Parallel Programming in Power System and Smart Grids

Parallel programming is a new field in computer science. The idea is to decrease the calculation time if the calculations are independent. Parallel programming is a method to divide the calculation into multiple sub-calculation steps and have separate processing cores to take care of each sub-calculation step. With this approach, calculation time can be saved. This approach can be used in power system applications where we need fast response. For example, optimal power flow, or power flow solution is achieved by solving nonlinear equations. However, in more complicated power systems, there will be thousands of nonlinear equations that can be separated into multiple groups, in which parallel computing can improve the speed of the calculation. This area still needs more investigations.

REFERENCES

- [1] R. H. Lasseter and P. Paigi, "Microgrid: a conceptual solution," in *Power Electronics Specialists Conference, 2004. PESC 04. 2004 IEEE 35th Annual*, vol. 6, June 2004, pp. 4285–4290 Vol.6.
- [2] F. Katiraei and M. R. Iravani, "Power management strategies for a microgrid with multiple distributed generation units," *IEEE Transactions on Power Systems*, vol. 21, no. 4, pp. 1821–1831, Nov 2006.
- [3] Y. W. Li and C. N. Kao, "An accurate power control strategy for power-electronics-interfaced distributed generation units operating in a low-voltage multibus microgrid," *IEEE Transactions on Power Electronics*, vol. 24, no. 12, pp. 2977–2988, Dec 2009.
- [4] R. Majumder, B. Chaudhuri, A. Ghosh, R. Majumder, G. Ledwich, and F. Zare, "Improvement of stability and load sharing in an autonomous microgrid using supplementary droop control loop," *IEEE Transactions on Power Systems*, vol. 25, no. 2, pp. 796–808, May 2010.
- [5] T. L. Vandoorn, B. Renders, L. Degroote, B. Meersman, and L. Vandevelde, "Active load control in islanded microgrids based on the grid voltage," *IEEE Transactions on Smart Grid*, vol. 2, no. 1, pp. 139–151, March 2011.
- [6] A. Mehrizi-Sani and R. Iravani, "Potential function based control of a microgrid in islanded and grid-connected modes," *IEEE Transactions on Power Systems*, vol. 25, no. 4, pp. 1883–1891, Nov 2010.
- [7] M. Pipattanasomporn, H. Feroze, and S. Rahman, "Multi-agent systems in a distributed smart grid: Design and implementation," in *Power Systems Conference and Exposition, 2009. PSCE '09. IEEE/PES*, March 2009, pp. 1–8.
- [8] S. Jacobsson and A. Johnson, "The diffusion of renewable energy technology: an analytical framework and key issues for research," *Energy policy*, vol. 28, no. 9, pp. 625–640, 2000.
- [9] X. Y. Wang, D. M. Vilathgamuwa, and S. S. Choi, "Determination of battery storage capacity in energy buffer for wind farm," *IEEE Transactions on Energy Conversion*, vol. 23, no. 3, pp. 868–878, Sept 2008.
- [10] A. G. Tsikalakis and N. D. Hatziargyriou, "Centralized control for optimizing microgrids operation," in *2011 IEEE Power and Energy Society General Meeting*, July 2011, pp. 1–8.
- [11] D. E. Olivares, C. A. Caizares, and M. Kazerani, "A centralized optimal energy management system for microgrids," in *2011 IEEE Power and Energy Society General Meeting*, July 2011, pp. 1–6.

- [12] A. H. Etemadi, E. J. Davison, and R. Iravani, "A decentralized robust control strategy for multi-der microgrids; part i: Fundamental concepts," *IEEE Transactions on Power Delivery*, vol. 27, no. 4, pp. 1843–1853, Oct 2012.
- [13] ———, "A decentralized robust control strategy for multi-der microgrids; part ii: Performance evaluation," *IEEE Transactions on Power Delivery*, vol. 27, no. 4, pp. 1854–1861, Oct 2012.
- [14] C. X. Dou and B. Liu, "Multi-agent based hierarchical hybrid control for smart microgrid," *IEEE Transactions on Smart Grid*, vol. 4, no. 2, pp. 771–778, June 2013.
- [15] B. Liu, S. Duan, and T. Cai, "Photovoltaic dc-building-module-based BIPV system concept and design considerations," *Power Electronics, IEEE Transactions on*, vol. 26, no. 5, pp. 1418–1429, 2011.
- [16] B. Yang, W. Li, Y. Zhao, and X. He, "Design and analysis of a grid-connected photovoltaic power system," *Power Electronics, IEEE Transactions on*, vol. 25, no. 4, pp. 992–1000, 2010.
- [17] W. Xiao and W. G. Dunford, "A modified adaptive hill climbing mppt method for photovoltaic power systems," in *Power Electronics Specialists Conference, 2004. PESC 04. 2004 IEEE 35th Annual*, vol. 3. Ieee, 2004, pp. 1957–1963.
- [18] F. Liu, Y. Kang, Y. Zhang, and S. Duan, "Comparison of p&o and hill climbing mppt methods for grid-connected pv converter," in *Industrial Electronics and Applications, 2008. ICIEA 2008. 3rd IEEE Conference on*. IEEE, 2008, pp. 804–807.
- [19] M. Ciobotaru, R. Teodorescu, and F. Blaabjerg, "Control of single-stage single-phase pv inverter," *EPE Journal*, vol. 16, no. 3, pp. 20–26, 2006.
- [20] J. H. Lee, H. Bae, and B. H. Cho, "Advanced incremental conductance mppt algorithm with a variable step size," in *Power Electronics and Motion Control Conference, 2006. EPE-PEMC 2006. 12th International*, Aug 2006, pp. 603–607.
- [21] Y.-C. Kuo, T.-J. Liang, and J.-F. Chen, "Novel maximum power point tracking controller for photovoltaic energy conversion system," *IEEE Transactions on Industrial Electronics*, vol. 48, no. 3, pp. 594–601, Jun 2001.
- [22] J. Liang *et al.*, "Control of multi-terminal vsc-hvdc transmission for offshore wind power," in *2009 13th European Conference on Power Electronics and Applications*, 2009, pp. 1–10.
- [23] D. Van Hertem and M. Ghandhari, "Multi-terminal vsc hvdc for the european supergrid: Obstacles," *Renewable and sustainable energy reviews*, vol. 14, no. 9, pp. 3156–3163, 2010.
- [24] J. Liang, T. Jing, O. Gomis-Bellmunt, J. Ekanayake, and N. Jenkins, "Operation and control of multi-terminal hvdc transmission for offshore wind farms," *Power Delivery, IEEE Transactions on*, vol. 26, no. 4, pp. 2596–2604, 2011.
- [25] L. Xu and L. Yao, "Dc voltage control and power dispatch of a multi-terminal hvdc system for integrating large offshore wind farms," *IET renewable power generation*, vol. 5, no. 3, pp. 223–233, 2011.

- [26] E. Prieto-Araujo, F. D. Bianchi, A. Junyent-Ferre, and O. Gomis-Bellmunt, "Methodology for droop control dynamic analysis of multi-terminal vsc-hvdc grids for offshore wind farms," *Power Delivery, IEEE Transactions on*, vol. 26, no. 4, pp. 2476–2485, 2011.
- [27] A. S. Abdel-Khalik, A. M. Massoud, A. A. Elserougi, and S. Ahmed, "Optimum power transmission-based droop control design for multi-terminal hvdc of offshore wind farms," 2013.
- [28] M. Aragüés-Peñalba, A. Egea-Alvarez, O. Gomis-Bellmunt, and A. Sumper, "Optimum voltage control for loss minimization in hvdc multi-terminal transmission systems for large offshore wind farms," *Electric Power Systems Research*, vol. 89, pp. 54–63, 2012.
- [29] S. Chiang, K. Chang, and C. Yen, "Residential photovoltaic energy storage system," *Industrial Electronics, IEEE Transactions on*, vol. 45, no. 3, pp. 385–394, 1998.
- [30] J. Khazaei, Z. Miao, L. Piyasinghe, and L. Fan, "Real-time digital simulation-based modeling of a single-phase single-stage pv system," *Electric Power Systems Research*, vol. 123, pp. 85–91, 2015.
- [31] L. Yazhou, "Studies on wind farm integration into power system," *Automation of Electric Power Systems*, vol. 8, p. 017, 2003.
- [32] K. Divya and J. Østergaard, "Battery energy storage technology for power systems: An overview," *Electric Power Systems Research*, vol. 79, no. 4, pp. 511–520, 2009.
- [33] X. Li, D. Hui, and X. Lai, "Battery energy storage station (bess)-based smoothing control of photovoltaic (pv) and wind power generation fluctuations," *Sustainable Energy, IEEE Transactions on*, vol. 4, no. 2, pp. 464–473, 2013.
- [34] B. S. Borowy and Z. M. Salameh, "Dynamic response of a stand-alone wind energy conversion system with battery energy storage to a wind gust," *Energy Conversion, IEEE Transactions on*, vol. 12, no. 1, pp. 73–78, 1997.
- [35] C. Hill, M. C. Such, D. Chen, J. Gonzalez, W. M. Grady *et al.*, "Battery energy storage for enabling integration of distributed solar power generation," *Smart Grid, IEEE Transactions on*, vol. 3, no. 2, pp. 850–857, 2012.
- [36] F. Guo, C. Wen, J. Mao, and Y.-D. Song, "Distributed secondary voltage and frequency restoration control of droop-controlled inverter-based microgrids," *Industrial Electronics, IEEE Transactions on*, vol. 62, no. 7, pp. 4355–4364, 2015.
- [37] A. Bidram, A. Davoudi, F. L. Lewis, and J. M. Guerrero, "Distributed cooperative secondary control of microgrids using feedback linearization," *Power Systems, IEEE Transactions on*, vol. 28, no. 3, pp. 3462–3470, 2013.
- [38] L.-Y. Lu and C.-C. Chu, "Consensus-based droop control synthesis for multiple dics in isolated micro-grids," *Power Systems, IEEE Transactions on*, vol. 30, no. 5, pp. 2243–2256, 2015.
- [39] J. Schiffer, T. Seel, J. Raisch, and T. Sezi, "Voltage stability and reactive power sharing in inverter-based microgrids with consensus-based distributed voltage control," *Control System Technology, IEEE Transactions on*, vol. 24, no. 1, pp. 96–109, 2015.

- [40] J. Y. Kim, J. H. Jeon, S. K. Kim, C. Cho, J. H. Park, H. M. Kim, and K. Y. Nam, “Cooperative control strategy of energy storage system and microsources for stabilizing the microgrid during islanded operation,” *IEEE Transactions on Power Electronics*, vol. 25, no. 12, pp. 3037–3048, Dec 2010.
- [41] T. Morstyn, B. Hredzak, and V. G. Agelidis, “Distributed cooperative control of microgrid storage,” *Power Systems, IEEE Transactions on*, vol. 30, no. 5, pp. 2780–2789, 2015.
- [42] J. Sun, “Impedance-based stability criterion for grid-connected inverters,” *Power Electronics, IEEE Transactions on*, vol. 26, no. 11, pp. 3075–3078, 2011.
- [43] M. Cespedes and J. Sun, “Impedance modeling and analysis of grid-connected voltage-source converters,” *IEEE Transactions on Power Electronics*, vol. 29, no. 3, pp. 1254–1261, March 2014.
- [44] L. Harnefors, M. Bongiorno, and S. Lundberg, “Input-admittance calculation and shaping for controlled voltage-source converters,” *Industrial Electronics, IEEE Transactions on*, vol. 54, no. 6, pp. 3323–3334, 2007.
- [45] Z. Miao, “Impedance-model-based ssr analysis for type 3 wind generator and series-compensated network,” 2012.
- [46] L. Zhang, L. Harnefors, and H.-P. Nee, “Power-synchronization control of grid-connected voltage-source converters,” *IEEE Trans. Power Syst.*, vol. 25, no. 2, pp. 809–820, 2010.
- [47] L. Xu and L. Fan, “Impedance-based resonance analysis in a VSC-HVDC system,” *IEEE Trans. Power Del.*, vol. 28, no. 4, pp. 2209–2216, 2013.
- [48] A. Egea-Alvarez, S. Fekriasl, F. Hassan, and O. Gomis-Bellmunt, “Advanced vector control for voltage source converters connected to weak grids,” *IEEE Trans. Power Syst.*, vol. 30, no. 6, pp. 3072–3081, 2015.
- [49] M. Braun, G. Arnold, and H. Laukamp, “Plugging into the zeitgeist,” *Power and Energy Magazine, IEEE*, vol. 7, no. 3, pp. 63–76, 2009.
- [50] A. K. Abdelsalam, A. M. Massoud, S. Ahmed, and P. N. Enjeti, “High-performance adaptive perturb and observe mppt technique for photovoltaic-based microgrids,” *Power Electronics, IEEE Transactions on*, vol. 26, no. 4, pp. 1010–1021, 2011.
- [51] H. Kanchev, D. Lu, F. Colas, V. Lazarov, and B. Francois, “Energy management and operational planning of a microgrid with a pv-based active generator for smart grid applications,” *Industrial Electronics, IEEE Transactions on*, vol. 58, no. 10, pp. 4583–4592, 2011.
- [52] K. Tan, P. So, Y. Chu, and M. Chen, “Coordinated control and energy management of distributed generation inverters in a microgrid,” 2013.
- [53] Y. Yang, K. Zhou, and F. Blaabjerg, “Harmonics suppression for single-phase grid-connected photovoltaic systems in different operation modes,” in *The Applied Power Electronics Conference and Exposition, 2013*.

- [54] Y. Wang, P. Zhang, W. Li, W. Xiao, and A. Abdollahi, "Online overvoltage prevention control of photovoltaic generators in microgrids," 2012.
- [55] A. M. Stanković, S. R. Sanders, and T. Aydin, "Dynamic phasors in modeling and analysis of unbalanced polyphase ac machines," *Energy Conversion, IEEE Transactions on*, vol. 17, no. 1, pp. 107–113, 2002.
- [56] A. M. Stanković and T. Aydin, "Analysis of asymmetrical faults in power systems using dynamic phasors," *Power Systems, IEEE Transactions on*, vol. 15, no. 3, pp. 1062–1068, 2000.
- [57] L. Piyasinghe, Z. Miao, and L. Fan, "Dynamic phase based model of type 1 wind generator for unbalanced operation," in *Power Electronics and Machines in Wind Applications (PEMWA), 2012 IEEE*. IEEE, 2012, pp. 1–5.
- [58] A. Stankovic, S. Sanders, and T. Aydin, "Dynamic phasors in modeling and analysis of unbalanced polyphase ac machines," *Energy Conversion, IEEE Transactions on*, vol. 17, no. 1, pp. 107–113, mar 2002.
- [59] Y.-H. Ji, D.-Y. Jung, J.-G. Kim, J.-H. Kim, T.-W. Lee, and C.-Y. Won, "A real maximum power point tracking method for mismatching compensation in PV array under partially shaded conditions," *Power Electronics, IEEE Transactions on*, vol. 26, no. 4, pp. 1001–1009, 2011.
- [60] L. Zhang, K. Sun, Y. Xing, L. Feng, and H. Ge, "A modular grid-connected photovoltaic generation system based on dc bus," *Power Electronics, IEEE Transactions on*, vol. 26, no. 2, pp. 523–531, 2011.
- [61] J. L. Agorreta, M. Borrega, J. López, and L. Marroyo, "Modeling and control of-paralleled grid-connected inverters with LCL filter coupled due to grid impedance in pv plants," *Power Electronics, IEEE Transactions on*, vol. 26, no. 3, pp. 770–785, 2011.
- [62] M. Park and I.-K. Yu, "A novel real-time simulation technique of photovoltaic generation systems using RTDS," *Energy Conversion, IEEE Transactions on*, vol. 19, no. 1, pp. 164–169, March 2004.
- [63] O. Craciun, A. Florescu, S. Bacha, I. Munteanu, and A. Bratcu, "Hardware-in-the-loop testing of pv control systems using rt-lab simulator," in *Power Electronics and Motion Control Conference (EPE/PEMC), 2010 14th International*, Sept 2010, pp. S2–1–S2–6.
- [64] S. B. Kjaer, "Evaluation of the hill climbing and the incremental conductance maximum power point trackers for photovoltaic power systems," *Energy Conversion, IEEE Transactions on*, vol. 27, no. 4, pp. 922–929, 2012.
- [65] W. Xiao and W. G. Dunford, "A modified adaptive hill climbing mppt method for photovoltaic power systems," in *Power Electronics Specialists Conference, 2004. PESC 04. 2004 IEEE 35th Annual*, vol. 3. Ieee, 2004, pp. 1957–1963.

- [66] A. K. Abdelsalam, A. M. Massoud, S. Ahmed, and P. Enjeti, “High-performance adaptive perturb and observe MPPT technique for photovoltaic-based microgrids,” *Power Electronics, IEEE Transactions on*, vol. 26, no. 4, pp. 1010–1021, 2011.
- [67] M. A. Elgendy, B. Zahawi, and D. J. Atkinson, “Assessment of perturb and observe mppt algorithm implementation techniques for pv pumping applications,” *Sustainable Energy, IEEE Transactions on*, vol. 3, no. 1, pp. 21–33, 2012.
- [68] D. Sera, R. Teodorescu, J. Hantschel, and M. Knoll, “Optimized maximum power point tracker for fast changing environmental conditions,” in *Industrial Electronics, 2008. ISIE 2008. IEEE International Symposium on*. IEEE, 2008, pp. 2401–2407.
- [69] G. Petrone, G. Spagnuolo, R. Teodorescu, M. Veerachary, and M. Vitelli, “Reliability issues in photovoltaic power processing systems,” *Industrial Electronics, IEEE Transactions on*, vol. 55, no. 7, pp. 2569–2580, 2008.
- [70] A. Safari and S. Mekhilef, “Simulation and hardware implementation of incremental conductance mppt with direct control method using cuk converter,” *Industrial Electronics, IEEE Transactions on*, vol. 58, no. 4, pp. 1154–1161, 2011.
- [71] —, “Incremental conductance mppt method for pv systems,” in *Electrical and computer engineering (CCECE), 2011 24th Canadian Conference on*. IEEE, 2011, pp. 000 345–000 347.
- [72] A. Pandey, N. Dasgupta, and A. K. Mukerjee, “Design issues in implementing mppt for improved tracking and dynamic performance,” in *IEEE Industrial Electronics, IECON 2006-32nd Annual Conference on*. IEEE, 2006, pp. 4387–4391.
- [73] M. Ciobotaru, R. Teodorescu, and F. Blaabjerg, “Control of single-stage single-phase pv inverter,” in *Power Electronics and Applications, 2005 European Conference on*. IEEE, 2005, pp. 10–pp.
- [74] E. Koutroulis and F. Blaabjerg, “A new technique for tracking the global maximum power point of pv arrays operating under partial-shading conditions,” *Photovoltaics, IEEE Journal of*, vol. 2, no. 2, pp. 184–190, 2012.
- [75] M. A. G. de Brito, L. Galotto, L. P. Sampaio, G. de Azevedo e Melo, and C. A. Canesin, “Evaluation of the main mppt techniques for photovoltaic applications,” *Industrial Electronics, IEEE Transactions on*, vol. 60, no. 3, pp. 1156–1167, 2013.
- [76] B. Liu, S. Duan, F. Liu, and P. Xu, “Analysis and improvement of maximum power point tracking algorithm based on incremental conductance method for photovoltaic array,” in *Power Electronics and Drive Systems, 7th International Conference on*. IEEE, 2007, pp. 637–641.
- [77] Q. Mei, M. Shan, L. Liu, and J. M. Guerrero, “A novel improved variable step-size incremental-resistance mppt method for pv systems,” *Industrial Electronics, IEEE Transactions on*, vol. 58, no. 6, pp. 2427–2434, 2011.

- [78] Z. Yan, L. Fei, Y. Jinjun, and D. Shanxu, "Study on realizing mppt by improved incremental conductance method with variable step-size," in *Industrial Electronics and Applications, 2008. ICIEA 2008. 3rd IEEE Conference on*. IEEE, 2008, pp. 547–550.
- [79] J. H. Lee, H. Bae, and B. H. Cho, "Advanced incremental conductance mppt algorithm with a variable step size," in *Power Electronics and Motion Control Conference, 2006. EPE-PEMC 2006. 12th International*. IEEE, 2006, pp. 603–607.
- [80] F. Liu, S. Duan, F. Liu, B. Liu, and Y. Kang, "A variable step size inc mppt method for pv systems," *Industrial Electronics, IEEE Transactions on*, vol. 55, no. 7, pp. 2622–2628, 2008.
- [81] S. R. Wenham, *Applied photovoltaics*. Routledge, 2011.
- [82] H. Pereira, A. Cupertino, C. da SG Ribeiro, and S. Silva, "Influence of pll in wind parks harmonic emissions," in *IEEE PES Conference on Innovative Smart Grid Technologies Latin America (ISGT LA)*. IEEE, 2013, pp. 1–8.
- [83] R. Teodorescu, F. Blaabjerg, U. Borup, and M. Liserre, "A new control structure for grid-connected lcl pv inverters with zero steady-state error and selective harmonic compensation," in *Applied Power Electronics Conference and Exposition, 2004. APEC'04. Nineteenth Annual IEEE*, vol. 1. IEEE, 2004, pp. 580–586.
- [84] J. Beerten, S. Cole, and R. Belmans, "Generalized steady-state vsc mtdc model for sequential ac/dc power flow algorithms," *Power Systems, IEEE Transactions on*, vol. 27, no. 2, pp. 821–829, 2012.
- [85] F. D. Bianchi and O. Gomis-Bellmunt, "Droop control design for multi-terminal vsc-hvdc grids based on lmi optimization," in *Decision and Control and European Control Conference (CDC-ECC), 2011 50th IEEE Conference on*. IEEE, 2011, pp. 4823–4828.
- [86] N. R. Chaudhuri and B. Chaudhuri, "Adaptive droop control for effective power sharing in multi-terminal dc (mtdc) grids," *Power Systems, IEEE Transactions on*, vol. 28, no. 1, pp. 21–29, 2013.
- [87] T. M. Haileselassie and K. Uhlen, "Impact of dc line voltage drops on power flow of mtdc using droop control," *Power Systems, IEEE Transactions on*, vol. 27, no. 3, pp. 1441–1449, 2012.
- [88] A. Egea-Alvarez, F. Bianchi, A. Junyent-Ferré, G. Gross, and O. Gomis-Bellmunt, "Voltage control of multi-terminal vsc-hvdc transmission systems for offshore wind power plants: Design and implementation in a scaled platform," *Industrial Electronics, IEEE Transactions on*, vol. 60, no. 6, pp. 2381–2391, 2013.
- [89] W. Wang and M. Barnes, "Power flow algorithms for multi-terminal VSC-HVDC with droop control," *Power Systems, IEEE Transactions on*, vol. 29, no. 4, pp. 1721–1730, July 2014.
- [90] J. Cao, W. Du, H. Wang, and S. Bu, "Minimization of transmission loss in meshed ac/dc grids with vsc-mtdc networks," *Power Systems, IEEE Transactions on*, vol. 28, no. 3, pp. 3047–3055, Aug 2013.

- [91] S. Abourida, C. Dufour, J. Bélanger, G. Murere, N. Léchevin, and B. Yu, “Real-time pc-based simulator of electric systems and drives,” in *Applied Power Electronics Conference and Exposition, 2002. APEC 2002. Seventeenth Annual IEEE*, vol. 1. IEEE, 2002, pp. 433–438.
- [92] J. M. Guerrero, J. C. Vasquez, J. Matas, D. Vicuna, L. García, and M. Castilla, “Hierarchical control of droop-controlled ac and dc microgrids: A general approach toward standardization,” *Industrial Electronics, IEEE Transactions on*, vol. 58, no. 1, pp. 158–172, 2011.
- [93] J.-Y. Kim, J.-H. Jeon, S.-K. Kim, C. Cho, J. H. Park, H.-M. Kim, and K.-Y. Nam, “Cooperative control strategy of energy storage system and microsources for stabilizing the microgrid during islanded operation,” *Power Electronics, IEEE Transactions on*, vol. 25, no. 12, pp. 3037–3048, 2010.
- [94] J. M. Guerrero, P. C. Loh, T.-L. Lee, and M. Chandorkar, “Advanced control architectures for intelligent microgrids part ii: Power quality, energy storage, and ac/dc microgrids,” *Industrial Electronics, IEEE Transactions on*, vol. 60, no. 4, pp. 1263–1270, 2013.
- [95] J. Lopes, C. Moreira, and A. Madureira, “Defining control strategies for microgrids islanded operation,” *Power Systems, IEEE Transactions on*, vol. 21, no. 2, pp. 916–924, 2006.
- [96] Z. Miao, L. Xu, V. R. Disfani, and L. Fan, “An soc-based battery management system for microgrids,” *Smart Grid, IEEE Transactions on*, vol. 5, no. 2, pp. 966–973, 2014.
- [97] X. Lu, K. Sun, J. M. Guerrero, J. C. Vasquez, L. Huang, and R. Teodorescu, “Soc-based droop method for distributed energy storage in dc microgrid applications,” in *Industrial Electronics (ISIE), 2012 IEEE International Symposium on*. IEEE, 2012, pp. 1640–1645.
- [98] X. Lu, K. Sun, J. M. Guerrero, J. C. Vasquez, and L. Huang, “State-of-charge balance using adaptive droop control for distributed energy storage systems in dc microgrid applications,” *Industrial Electronics, IEEE Transactions on*, vol. 61, no. 6, pp. 2804–2815, 2014.
- [99] T. Morstyn, B. Hredzak, and V. G. Agelidis, “Communication delay robustness for multi-agent state of charge balancing between distributed ac microgrid storage systems,” in *2015 IEEE Conference on Control Applications (CCA)*, Sept 2015, pp. 181–186.
- [100] O. Palizban and K. Kauhaniemi, “Distributed cooperative control of battery energy storage system in ac microgrid applications,” *Journal of Energy Storage*, vol. 3, pp. 43–51, 2015.
- [101] C. Li, T. Dragicevic, J. C. Vasquez, J. M. Guerrero, and E. A. A. Coelho, “Multi-agent-based distributed state of charge balancing control for distributed energy storage units in ac microgrids,” in *2015 IEEE Applied Power Electronics Conference and Exposition (APEC)*, March 2015, pp. 2967–2973.
- [102] H. Zhang, F. L. Lewis, and Z. Qu, “Lyapunov, adaptive, and optimal design techniques for cooperative systems on directed communication graphs,” *Industrial Electronics, IEEE Transactions on*, vol. 59, no. 7, pp. 3026–3041, 2012.
- [103] J. A. Fax and R. M. Murray, “Information flow and cooperative control of vehicle formations,” *Automatic Control, IEEE Transactions on*, vol. 49, no. 9, pp. 1465–1476, 2004.

- [104] M. Chen, G. Rincón-Mora *et al.*, “Accurate electrical battery model capable of predicting runtime and iv performance,” *Energy Conversion, IEEE Transactions on*, vol. 21, no. 2, pp. 504–511, 2006.
- [105] O. B. Nayak, A. Gole, D. Chapman, and J. Davies, “Dynamic performance of static and synchronous compensators at an HVDC inverter bus in a very weak ac system,” *IEEE Trans. Power Syst.*, vol. 9, no. 3, pp. 1350–1358, 1994.
- [106] X. Koutiva, T. Vrionis, N. Vovos, and G. B. Giannakopoulos, “Optimal integration of an offshore wind farm to a weak ac grid,” *IEEE Trans. Power Del.*, vol. 21, no. 2, pp. 987–994, 2006.
- [107] J. Pan, R. Nuqui, K. Srivastava, T. Jonsson, P. Holmberg, and Y.-J. Hafner, “Ac grid with embedded vsc-hvdc for secure and efficient power delivery,” in *Energy 2030 Conference, IEEE*, Nov 2008, pp. 1–6.
- [108] A. Gavrilovic, “Ac/dc system strength as indicated by short circuit ratios,” in *International Conference on AC and DC Power Transmission*, Sep 1991, pp. 27–32.
- [109] X. Zheng, “Characteristics of HVDC connected to weak ac systems part1: HVDC transmission capability,” *Power System Technology*, vol. 21, no. 1, pp. 12–16, 1997.
- [110] F. Schettler, H. Huang, and N. Christl, “HVDC transmission systems using voltage sourced converters design and applications,” in *IEEE Power Engineering Society Summer Meeting*, vol. 2, 2000, pp. 715–720.
- [111] N. Flourentzou, V. G. Agelidis, and G. D. Demetriades, “VSC-based HVDC power transmission systems: An overview,” *IEEE Trans. Power Electron.*, vol. 24, no. 3, pp. 592–602, 2009.
- [112] L. Zhang, L. Harnefors, and H.-P. Nee, “Modeling and control of VSC-HVDC links connected to island systems,” *IEEE Trans. Power Syst.*, vol. 26, no. 2, pp. 783–793, 2011.
- [113] A. Yazdani and R. Iravani, *Voltage-sourced converters in power systems: modeling, control, and applications*. John Wiley & Sons, 2010.
- [114] S. Li, T. Haskew, and L. Xu, “Control of HVDC light system using conventional and direct current vector control approaches,” *IEEE Trans. Power Electron.*, vol. 25, no. 12, pp. 3106–3118, 2010.
- [115] M. Durrant, H. Werner, and K. Abbott, “Model of a VSC-HVDC terminal attached to a weak ac system,” in *IEEE Conference on Control Applications.*, vol. 1, 2003, pp. 178–182.
- [116] L. Zhang, L. Harnefors, and H.-P. Nee, “Interconnection of two very weak ac systems by VSC-HVDC links using power-synchronization control,” *IEEE Trans. Power Syst.*, vol. 26, no. 1, pp. 344–355, 2011.
- [117] P. Mitra, L. Zhang, and L. Harnefors, “Offshore wind integration to a weak grid by VSC-HVDC links using power-synchronization control: A case study,” *IEEE Trans. Power Del.*, vol. 29, no. 1, pp. 453–461, 2014.

- [118] L. Zhang, H.-P. Nee, and L. Harnefors, "Analysis of stability limitations of a VSC-HVDC link using power-synchronization control," *IEEE Trans. Power Syst.*, vol. 26, no. 3, pp. 1326–1337, 2011.
- [119] K. M. Alawasa and Y. A.-R. Mohamed, "Impedance and damping characteristics of grid-connected vscs with power synchronization control strategy," *IEEE Trans. Power Syst.*, vol. 30, no. 2, pp. 952–961, 2015.
- [120] L. Xu, L. Fan, and Z. Miao, "Dc impedance-model-based resonance analysis of a VSC-HVDC system," *IEEE Trans. Power Del.*, vol. 30, no. 3, 2015.
- [121] B. Wen, D. Boroyevich, R. Burgos, P. Mattavelli, and Z. Shen, "Small-signal stability analysis of three-phase ac systems in the presence of constant power loads based on measured dq frame impedances," *IEEE Trans. Power Electron.*, no. 10, pp. 5952–5963, Oct. 2015.
- [122] M. Morari and E. Zafiriou, *Robust process control*. Morari, 1989.
- [123] N. Lehtomaki, N. R. Sandell Jr, M. Athans *et al.*, "Robustness results in linear-quadratic gaussian based multi-variable control designs," *Automatic Control, IEEE Transactions on*, vol. 26, no. 1, pp. 75–93, 1981.
- [124] L. Piyasinghe, Z. Miao, J. Khazaei, and L. Fan, "Impedance model-based ssr analysis for tesc compensated type-3 wind energy delivery systems," *Sustainable Energy, IEEE Transactions on*, vol. 6, no. 1, pp. 179–187, 2015.
- [125] P. Mattavelli, G. C. Verghese, and A. M. Stankovic, "Phasor dynamics of thyristor-controlled series capacitor systems," *Power Systems, IEEE Transactions on*, vol. 12, no. 3, pp. 1259–1267, 1997.
- [126] M. Ciobotaru, R. Teodorescu, and F. Blaabjerg, "Control of single-stage single-phase pv inverter," in *Power Electronics and Applications, 2005 European Conference on*. IEEE, 2005, pp. 10–pp.
- [127] C. Meza, J. J. Negroni, D. Biel, and F. Guinjoan, "Energy-balance modeling and discrete control for single-phase grid-connected pv central inverters," *Industrial Electronics, IEEE Transactions on*, vol. 55, no. 7, pp. 2734–2743, 2008.

APPENDICES

Appendix A List of Parameters

Table A.1. Parameters of single phase PV for Sunpower panel

Total capacity	2.4 kW
Nominal voltage	440V
Open circuit voltage per cell	64.2 V
Short circuit current per cell	5.96 A
K_p, K_r of PR Controller	100,500
ω	377 rad/sec
K_p, K_i of MPPT Controller	5,20
K_p, K_i of PLL	180,3200
L_b, L_a of AC Filter	20,10 mH
C of AC filter	1 μ F
Frequency	60 Hz

Table A.2. Parameters of the wind farm side rectifiers

K_p current control loop	50
K_i current control loop	100
L	0.1 H
Q_{ref}	0 MVar
ω_s	377 rad/sec

Table A.3. Parameters of the grid side inverters

K_p outer loop	0.4
K_i outer loop	2
K_p inner loop	50
K_i inner loop	100
L	0.1 H
Q_{ref}	0 Mvar

Appendix A (Continued)

Table A.4. Parameters of the system

Quantity	Value
AC grid	13.8 kV, 60 Hz
Grid filter	$0.1+j3 \Omega$
Filter 1	$j0.6 \Omega$
Filter 2	$j0.75 \Omega$
Filter 3	$j0.9 \Omega$
Induction machine	5.5 kVA, 60 Hz, 0.4 kV
Load 1	33 kW
Load 2	20 kW, 5 kVAR
Load 3	13 kW

Table A.5. Parameters of transformers

Number	Voltage(kV)	Power(kVA)	$Z_1, Z_2 (\Omega)$
T_1	13.8/0.4	800	$0.02+j0.1$
T_2 to T_5	0.4/0.4	200	$0.01+j0.05$

Table A.6. Parameters of battery control

Quantity	Value
Switching frequency	1620 Hz
Inverter nominal power	100 kW
α_f	1000 Hz

Table A.7. Parameters of individual batteries

Quantity	Value
R_{DS}	$1e^6 \Omega$
C_C	$39e^5$ F
R_S	0.0074Ω
R_{TS}	0.0046Ω
C_{TS}	$70.36e^3$ F
R_{TL}	0.0498Ω
C_{TL}	$447.5e^3$ F
f_1, f_2	1

Appendix A (Continued)

Table A.8. System parameters for VSC-HVDC model

Quantity	Value
AC system line voltage	100 kV
AC system frequency	60 Hz
HVDC rated power	100 MW
dc rated voltage	250 kV
DC cable parameters	0.0139 Ω /km, 0.159 mH/km, 0.231 μ F/km
DC cable length	20 km

Table A.9. Parameters of individual VSC

Switching frequency	1620 Hz
Grid filter	0.048 H (for SCR 3)
Grid filter	0.088 H (for SCR 2)
Grid filter	0.25 H (for SCR 1)
DC capacitor	96 μ F

Table A.10. Parameters of power synchronization

PSC controller	$k_{ip}=5$
PI controller	$k_{pv}=0.5, k_{iv}=10$

Table A.11. Parameters of vector controllers

Current controller	$k_p=50, k_i=100$
Alternating voltage controller	$k_p=0.01, k_i=100$
Outer PI controller	$k_p=0.1, k_i=5$

Table A.12. Parameters of the induction machine

Total capacity	5.5 kVA
Nominal voltage	400 V
Frequency	60 Hz
R_s	2.52 Ω
R_r	2.67 Ω
X_{ls}	3.39 Ω
X_{lr}	3.39 Ω
X_M	197 Ω
J	0.486 $kg.m^2$
P (poles)	4

Appendix A (Continued)

Table A.13. Parameters of the PV

Total capacity	2000 W
Frequency	60Hz
L_a	0.01 H
L_b	0.02 H
Cap	3 μH
$K_p(PLL)$	180
$K_i(PLL)$	3200
$K_p(PR)$	200
$K_i(PR)$	1500

Table A.14. Line data of the network

Line No	Line Type	Z (Ω/km)	Length(m)
1	Z_{Grid}	0.579+j1.75	105
2	Z_{IM}	0.497+j2.47	105
3	Z_{PV}	0.462+j0.564	30

Appendix B Reuse Permissions of Published Papers for Chapters 3, 4, and 7

5/16/2016 Rightslink® by Copyright Clearance Center

 **Copyright Clearance Center** **RightsLink®** [Home](#) [Account Info](#) [Help](#) [Live Chat](#)



Title: Real-time digital simulation-based modeling of a single-phase single-stage PV system
Author: Javad Khazaei, Zhixin Miao, Lakshmi Piyasinghe, Lingling Fan
Publication: Electric Power Systems Research
Publisher: Elsevier
Date: June 2015

Logged in as: javad khazaei
Account #: 3001027655
[LOGOUT](#)

Copyright © 2015 Elsevier B.V. All rights reserved.

Order Completed

Thank you very much for your order.

This is a License Agreement between javad khazaei ("You") and Elsevier ("Elsevier"). The license consists of your order details, the terms and conditions provided by Elsevier, and the [payment terms and conditions](#).

[Get the printable license.](#)

License Number	3871100173108
License date	May 16, 2016
Licensed content publisher	Elsevier
Licensed content publication	Electric Power Systems Research
Licensed content title	Real-time digital simulation-based modeling of a single-phase single-stage PV system
Licensed content author	Javad Khazaei, Zhixin Miao, Lakshmi Piyasinghe, Lingling Fan
Licensed content date	June 2015
Licensed content volume number	123
Licensed content issue number	n/a
Number of pages	7
Type of Use	reuse in a thesis/dissertation
Portion	full article
Format	both print and electronic
Are you the author of this Elsevier article?	Yes
Will you be translating?	No
Title of your thesis/dissertation	Distributed Coordination and Control of Renewable Energy Sources in Microgrids
Expected completion date	Jun 2016
Estimated size (number of pages)	170
Elsevier VAT number	GB 494 6272 12
Permissions price	0.00 USD
VAT/Local Sales Tax	0.00 USD / 0.00 GBP
Total	0.00 USD

[ORDER MORE...](#)

[CLOSE WINDOW](#)

Copyright © 2016 Copyright Clearance Center, Inc. All Rights Reserved. [Privacy statement](#). [Terms and Conditions](#).
Comments? We would like to hear from you. E-mail us at customercare@copyright.com

Appendix B (Continued)

5/22/2016

Rightslink® by Copyright Clearance Center



RightsLink®

Home

Account Info

Help



Title: Real-time digital simulation modeling of single-phase PV in RT-LAB
Conference Proceedings: 2014 IEEE PES General Meeting | Conference & Exposition
Author: Javad Khazaei; Lakshan Piyasinghe; Zhixin Miao; Lingling Fan
Publisher: IEEE
Date: 27-31 July 2014
Copyright © 2014, IEEE

Logged in as:
javad.khazaei
Account #:
3001027655

LOGOUT

Thesis / Dissertation Reuse

The IEEE does not require individuals working on a thesis to obtain a formal reuse license, however, you may print out this statement to be used as a permission grant:

Requirements to be followed when using any portion (e.g., figure, graph, table, or textual material) of an IEEE copyrighted paper in a thesis:

- 1) In the case of textual material (e.g., using short quotes or referring to the work within these papers) users must give full credit to the original source (author, paper, publication) followed by the IEEE copyright line © 2011 IEEE.
- 2) In the case of illustrations or tabular material, we require that the copyright line © [Year of original publication] IEEE appear prominently with each reprinted figure and/or table.
- 3) If a substantial portion of the original paper is to be used, and if you are not the senior author, also obtain the senior author's approval.

Requirements to be followed when using an entire IEEE copyrighted paper in a thesis:

- 1) The following IEEE copyright/ credit notice should be placed prominently in the references: © [year of original publication] IEEE. Reprinted, with permission, from [author names, paper title, IEEE publication title, and month/year of publication]
- 2) Only the accepted version of an IEEE copyrighted paper can be used when posting the paper or your thesis on-line.
- 3) In placing the thesis on the author's university website, please display the following message in a prominent place on the website: In reference to IEEE copyrighted material which is used with permission in this thesis, the IEEE does not endorse any of [university/educational entity's name goes here]'s products or services. Internal or personal use of this material is permitted. If interested in reprinting/republishing IEEE copyrighted material for advertising or promotional purposes or for creating new collective works for resale or redistribution, please go to http://www.ieee.org/publications_standards/publications/rights/rights_link.html to learn how to obtain a License from RightsLink.

If applicable, University Microfilms and/or ProQuest Library, or the Archives of Canada may supply single copies of the dissertation.

BACK

CLOSE WINDOW


Copyright © 2016 Copyright Clearance Center, Inc. All Rights Reserved. [Privacy statement](#). [Terms and Conditions](#).
Comments? We would like to hear from you. E-mail us at customercare@copyright.com

<https://s100.copyright.com/AppDispatchServlet#formTop>

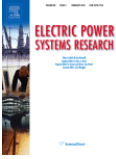
1/1

Appendix B (Continued)

5/16/2016 Rightslink® by Copyright Clearance Center



Home Account Info Help Live Chat



Title: Minimizing DC system loss in multi-terminal HVDC systems through adaptive droop control

Author: Javad Khazaei, Zhixin Miao, Lakshmi Piyasinghe, Lingling Fan

Publication: Electric Power Systems Research

Publisher: Elsevier

Date: September 2015

Logged in as: javad khazaei
Account #: 3001027655
LOGOUT

Copyright © 2015 Elsevier B.V. All rights reserved.

Order Completed

Thank you very much for your order.

This is a License Agreement between javad khazaei ("You") and Elsevier ("Elsevier"). The license consists of your order details, the terms and conditions provided by Elsevier, and the [payment terms and conditions](#).

[Get the printable license.](#)

License Number	3871100062953
License date	May 16, 2016
Licensed content publisher	Elsevier
Licensed content publication	Electric Power Systems Research
Licensed content title	Minimizing DC system loss in multi-terminal HVDC systems through adaptive droop control
Licensed content author	Javad Khazaei, Zhixin Miao, Lakshmi Piyasinghe, Lingling Fan
Licensed content date	September 2015
Licensed content volume number	126
Licensed content issue number	n/a
Number of pages	9
Type of Use	reuse in a thesis/dissertation
Portion	full article
Format	both print and electronic
Are you the author of this Elsevier article?	Yes
Will you be translating?	No
Title of your thesis/dissertation	Distributed Coordination and Control of Renewable Energy Sources in Microgrids
Expected completion date	Jun 2016
Estimated size (number of pages)	170
Elsevier VAT number	GB 494 6272 12
Permissions price	0.00 USD
VAT/Local Sales Tax	0.00 USD / 0.00 GBP
Total	0.00 USD


ORDER MORE...


CLOSE WINDOW

Copyright © 2016 Copyright Clearance Center, Inc. All Rights Reserved. [Privacy statement](#). [Terms and Conditions](#). Comments? We would like to hear from you. E-mail us at customer@copyright.com

Appendix B (Continued)

5/22/2016 Rightslink® by Copyright Clearance Center

 **RightsLink®** [Home](#) [Account Info](#) [Help](#) [Live Chat](#)

 **IEEE**
Requesting permission to reuse content from an IEEE publication

Title: Dynamic Phasor-Based Modeling of Unbalanced Radial Distribution Systems
Author: Zhixin Miao; Lakshan Piyasinghe; Javad Khazaei; Lingling Fan
Publication: Power Systems, IEEE Transactions on
Publisher: IEEE
Date: Nov. 2015
Copyright © 2015, IEEE

Logged in as: javad.khazaei
Account #: 3001027655
[LOGOUT](#)

Thesis / Dissertation Reuse

The IEEE does not require individuals working on a thesis to obtain a formal reuse license, however, you may print out this statement to be used as a permission grant:

Requirements to be followed when using any portion (e.g., figure, graph, table, or textual material) of an IEEE copyrighted paper in a thesis:

- 1) In the case of textual material (e.g., using short quotes or referring to the work within these papers) users must give full credit to the original source (author, paper, publication) followed by the IEEE copyright line © 2011 IEEE.
- 2) In the case of illustrations or tabular material, we require that the copyright line © [Year of original publication] IEEE appear prominently with each reprinted figure and/or table.
- 3) If a substantial portion of the original paper is to be used, and if you are not the senior author, also obtain the senior author's approval.

Requirements to be followed when using an entire IEEE copyrighted paper in a thesis:

- 1) The following IEEE copyright/ credit notice should be placed prominently in the references: © [year of original publication] IEEE. Reprinted, with permission, from [author names, paper title, IEEE publication title, and month/year of publication]
- 2) Only the accepted version of an IEEE copyrighted paper can be used when posting the paper or your thesis on-line.
- 3) In placing the thesis on the author's university website, please display the following message in a prominent place on the website: In reference to IEEE copyrighted material which is used with permission in this thesis, the IEEE does not endorse any of [university/educational entity's name goes here]'s products or services. Internal or personal use of this material is permitted. If interested in reprinting/republishing IEEE copyrighted material for advertising or promotional purposes or for creating new collective works for resale or redistribution, please go to http://www.ieee.org/publications_standards/publications/rights/rights_link.html to learn how to obtain a License from RightsLink.

If applicable, University Microfilms and/or ProQuest Library, or the Archives of Canada may supply single copies of the dissertation.

[BACK](#)

[CLOSE WINDOW](#)

Copyright © 2016 [Copyright Clearance Center, Inc.](#) All Rights Reserved. [Privacy statement](#), [Terms and Conditions](#).
Comments? We would like to hear from you. E-mail us at customercare@copyright.com

Appendix B (Continued)

5/22/2016

Rightslink® by Copyright Clearance Center



RightsLink®

Home

Account Info

Help



Title: Initialization of unbalanced radial distribution systems for small signal stability analysis
Conference Proceedings: 2015 IEEE Power & Energy Society General Meeting
Author: Javad Khazaei; Zhixin Miao; Lakshani Piyasinghe; Lingling Fan
Publisher: IEEE
Date: 26-30 July 2015
Copyright © 2015, IEEE

Logged in as:
javad.khazaei
Account #:
3001027655

LOGOUT

Thesis / Dissertation Reuse

The IEEE does not require individuals working on a thesis to obtain a formal reuse license, however, you may print out this statement to be used as a permission grant:

Requirements to be followed when using any portion (e.g., figure, graph, table, or textual material) of an IEEE copyrighted paper in a thesis:

- 1) In the case of textual material (e.g., using short quotes or referring to the work within these papers) users must give full credit to the original source (author, paper, publication) followed by the IEEE copyright line © 2011 IEEE.
- 2) In the case of illustrations or tabular material, we require that the copyright line © [Year of original publication] IEEE appear prominently with each reprinted figure and/or table.
- 3) If a substantial portion of the original paper is to be used, and if you are not the senior author, also obtain the senior author's approval.

Requirements to be followed when using an entire IEEE copyrighted paper in a thesis:

- 1) The following IEEE copyright/ credit notice should be placed prominently in the references: © [year of original publication] IEEE. Reprinted, with permission, from [author names, paper title, IEEE publication title, and month/year of publication]
- 2) Only the accepted version of an IEEE copyrighted paper can be used when posting the paper or your thesis on-line.
- 3) In placing the thesis on the author's university website, please display the following message in a prominent place on the website: In reference to IEEE copyrighted material which is used with permission in this thesis, the IEEE does not endorse any of [university/educational entity's name goes here]'s products or services. Internal or personal use of this material is permitted. If interested in reprinting/republishing IEEE copyrighted material for advertising or promotional purposes or for creating new collective works for resale or redistribution, please go to http://www.ieee.org/publications_standards/publications/rights/rights_link.html to learn how to obtain a License from RightsLink.

If applicable, University Microfilms and/or ProQuest Library, or the Archives of Canada may supply single copies of the dissertation.

BACK

CLOSE WINDOW

Copyright © 2016 Copyright Clearance Center, Inc. All Rights Reserved. [Privacy statement](#). [Terms and Conditions](#).
Comments? We would like to hear from you. E-mail us at customercare@copyright.com

<https://s100.copyright.com/AppDispatchServlet#formTop>

1/1

ABOUT THE AUTHOR

Javad Khazaei was born in 1987 in Ghaemshahr, Iran. He obtained his bachelor degree in Electrical Engineering from University of Mazandaran, Iran in 2009 and his masters degree from Urmia University, Iran in 2011. He received his Ph.D. degree in Electrical Engineering from the University of South Florida in June, 2016. His research interests include: distributed control of Microgrids, modeling of Renewable energy sources and power electronics devices, Stability analysis of microgrids and real-time digital simulation.